



University of Coimbra
Faculty of Sciences and Technology
Department of Electrical and Computer Engineering

SLIDING MODE CONTROL APPLIED IN
TRAJECTORY-TRACKING
OF WMRs AND AUTONOMOUS VEHICLES

Razvan Constantin Solea
March 2009



University of Coimbra
Faculty of Sciences and Technology
Department of Electrical and Computer Engineering

SLIDING MODE CONTROL APPLIED IN
TRAJECTORY-TRACKING
OF WMRs AND AUTONOMOUS VEHICLES

A DISSERTATION
SUBMITTED TO THE DEPARTMENT OF
ELECTRICAL AND COMPUTER ENGINEERING
OF COIMBRA UNIVERSITY
IN PARTIAL FULFILLMENT OF THE REQUIREMENTS
FOR THE DEGREE OF DOCTOR OF PHILOSOPHY

Razvan Constantin Solea

UNDER SUPERVISION OF
Professor Urbano NUNES (supervisor)
Professor Adrian FILIPESCU (co-supervisor)

Acknowledgment

I would like to express my deep gratitude to my advisor Prof. Urbano Nunes (Associate Professor with the Department of Electrical and Computer Engineering of the Faculty of Sciences and Technology (FCTUC) of University of Coimbra, Portugal) for his continuous and patient guidance helping me discover abilities I did not know I had, for the honest and valuable advises he gave me.

I also want to thank Prof. Adrian Filipescu and Prof. Viorel Dugan (Professors with the Department of Automation and Industrial Informatics of the Faculty of Computer Science of University "Dunarea de Jos" of Galati, Romania) for believing in me and making this trip possible.

To Elena, thank you for your love, patience, and endless support, especially during the PhD stage.

To the numerous friends I met in Coimbra, thank you for the funny and not so funny moments.

During the period of this work, at Institute of Systems and Robotics (ISR) - Coimbra, Portugal, I was supported in part by Portuguese Foundation for Science and Technology (FCT), under research fellowship: SFRH/BD//18211/2004 and by ISR - Coimbra and FCT, under contract NCT04: POSC/EEA/SRI/58016/2004 - "Nonlinear control techniques applied in path following of WMRs and autonomous, vehicles with high precision localization system".

Contents

Acknowledgment	v
1 Introduction	3
1.1 Motivation and Background	3
1.2 Contributions	5
1.3 Outline of the Thesis	7
2 Trajectory Tracking Problems	9
2.1 Related Works	9
2.2 Motivation	12
3 Kinematic and Dynamic Models for Differential-drive and Car-like Mobile Robots	15
3.1 Kinematic and Dynamic Modeling for Differential-drive Robots	15
3.2 Motion Control for WMR	19
3.2.1 Point Stabilization	22
3.2.2 Trajectory Tracking	23
3.2.3 Path Following	24
3.3 Kinematic and Dynamic Modeling for Car-like Vehicle	27
3.3.1 Dynamics of the Nonlinear Single-Track Model	30
3.3.2 Linearized Single-Track Model	34
3.4 Motion Control for Car-like Vehicle	36
3.4.1 Longitudinal Control	36
3.4.2 Lateral Control	37
3.4.3 Integration of Lateral and Longitudinal Controls	37
4 Path Planning	39
4.1 Introduction	39

4.2	Quintic Equations	41
4.3	Velocity Planning	43
5	Sliding Mode Control Design	55
5.1	Definitions and Preliminaries	55
5.2	Sliding Surface Design	58
5.3	Control Law Design	62
5.4	Chattering Problem and its Reduction	67
5.5	Sliding Mode Trajectory-Tracking Control for WMR	69
5.5.1	Simulation Results	71
5.6	Sliding Mode Trajectory-Tracking Control for Car-like Vehicle	75
5.6.1	Simulation Results	78
5.7	Sliding-Mode Path-Following Control for WMR	80
5.7.1	Simulation Results	83
6	Human Body Comfort	87
6.1	Introduction	87
6.2	Model of Human Head-Neck Complex	93
6.3	Experimental Date From Inertial Sensor	95
7	Implementation in Real Wheelchair - RobChair	99
7.1	Introduction	99
7.2	Architecture of RobChair	101
7.2.1	Hardware and Software Architecture	102
7.3	Robot Constraints	106
7.3.1	Velocity Limits	106
7.3.2	Acceleration and Deceleration Limits	106
7.3.3	Maximum Velocity to Avoid Sliding Out	107
7.3.4	Wheel-Ground Interaction to Avoid Slippage	110
7.3.5	Calculation of the Coefficient of Friction	111
7.3.6	Bounded Wheel Speed Commands	112
7.3.7	Dynamic Constraints	115
7.3.8	Feasible Constraints	116
7.4	Experimental Results	116
7.4.1	Experimental Results Under Odometry Navigation	116
7.4.2	Experimental Results Under Magnetic-markers Navigation	117

8	Conclusions	123
A	Appendix	125
	Bibliography	127

List of Tables

3.1	Parameters of the car model	31
3.2	Vehicle model summary	36
4.1	Length, time and r.m.s. acceleration values for each curve	52
4.2	Length, time and r.m.s. acceleration values for each curve (Fig. 4.9) .	54
6.1	Most relevant parameters	90
6.2	ISO 2631-1 STANDARD.	92
6.3	Characteristics of user's elements	95
6.4	Experimental results.	96
7.1	Fusion algorithm.	105
7.2	Experimental results for SM-TT controller under odometry navigation.	118
7.3	Experimental results for SM-TT controller under odometry navigation.	118
7.4	Experimental results for SM-TT controller under magnetic-markers navigation.	121
7.5	Experimental results for SM-TT controller under magnetic-markers navigation.	121
7.6	Experimental results for SM-PF controller under magnetic-markers navigation.	121

List of Figures

3.1	WMR model and symbols.	16
3.2	Motion control using the kinematic model.	20
3.3	Two-stage model of a real mobile robot.	20
3.4	Inner loop control of a mobile robot (dynamic-level control).	20
3.5	Control of a real mobile robot.	21
3.6	Description of the Trajectory Tracking Problem.	24
3.7	Description of the Path Following Problem.	25
3.8	Description of the Path Following problem with look-ahead distance.	26
3.9	Kinematics model of A) 4 wheel vehicle; B) Bicycle model.	28
3.10	The one-track bicycle model.	32
3.11	The one-track bicycle model.	33
4.1	Path planning example using quintic polynomial curves.	42
4.2	Lane change ($\eta_1 = \eta_2 = 1, 2, 3, 4, 5, \eta_3 = \eta_4 = 0$).	44
4.3	Lane change ($\eta_1 = \eta_2 = 5, \eta_3 = \eta_4 = -50, -25, 0, 25, 50$).	44
4.4	An example of a longitudinal velocity profile.	46
4.5	Restrictive cases of a_w	50
4.6	Linear and angular velocity for path example depicted in Fig. 4.1.	51
4.7	Lateral and longitudinal accelerations for path example depicted in Fig. 4.1.	51
4.8	R.m.s. acceleration values for path example depicted in Fig. 4.1.	52
4.9	Path planning example	53
4.10	Linear and angular velocity for path example (Figure 4.9); case <i>A</i> and <i>B</i>	53
4.11	Lateral and longitudinal accelerations for path example (Figure 4.9); case <i>A</i> and <i>B</i>	53
4.12	R.m.s. acceleration values for path example (Figure 4.9); case <i>A</i> and <i>B</i>	54

5.1	Geometric interpretation of two intersecting switching surfaces.	57
5.2	Block diagram of observer based sliding mode control.	68
5.3	Disturbance compensation with sliding mode disturbance observer.	68
5.4	Simulation model block diagram (Simulink scheme).	72
5.5	Simulink model for RobChair.	72
5.6	Path examples calculated by the trajectory planner (see Chapter 4).	72
5.7	Velocities and accelerations for the path depicted in Fig. 5.6.	73
5.8	R.M.S. acceleration values for each path-segment (AB, BC,...) of the paths depicted in Fig. 5.6.	73
5.9	Desired v_d , command v_c and real v_r linear velocities for SM-TT control - Path 1 and Path 2.	73
5.10	Desired ω_d , command ω_c and real ω_r angular velocities for SM-TT control - Path1 and Path 2.	74
5.11	Desired av_d , command av_c and real av_r longitudinal accelerations for SM-TT control - Path 1 and Path 2.	74
5.12	Desired $a\omega_d$, command $a\omega_c$ and real $a\omega_r$ angular accelerations for SM-TT control - Path1 and Path 2.	74
5.13	Longitudinal, lateral and angular errors of SM-TT control - Path 1 and Path 2.	75
5.14	Simulation SM-TT control starting from an initial error state ($x_e(0) = -0.5, y_e(0) = -0.5, \phi_e(0) = 0$).	75
5.15	Bicycle model (5.62)	76
5.16	Lateral, longitudinal and orientation error (trajectory-tracking)	76
5.17	Simulation model block diagram (Simulink scheme).	78
5.18	Simulink model for car-like vehicle.	79
5.19	Desired (v_d, δ_d) , command (v_c, δ_c) and real (v_r, δ_r) linear velocities and steering angles for SM-TT controller without initial pose error - Path Fig. 4.1	79
5.20	Desired $(av_d, a\delta_d)$, command $(av_c, a\delta_c)$ and real $(av_r, a\delta_r)$ longitudinal and lateral accelerations for SM-TT controller without initial pose error - Path Fig. 4.1	79
5.21	Longitudinal (x_e), lateral (y_e) and orientation (ϕ_e) errors for SM-TT controller without initial pose error - Path Fig. 4.1	80
5.22	Simulation SM-TT control starting from an initial error state ($x_e(0) = -2.5, y_e(0) = -2.5, \phi_e(0) = \pi/4$).	80

5.23	Simulation model block diagram for TT-PF control - Simulink scheme.	84
5.24	Simulation of TT-PF controller with a given longitudinal velocity profile.	84
5.25	Desired $a\omega_d$, command $a\omega_c$ and real $a\omega_r$ longitudinal and angular velocity for SM-PF control.	85
5.26	Lateral and angular errors of SM-PF control.	85
5.27	Simulation of TT-PF controller with a constant longitudinal velocity ($v_d = 0.5m/s$).	85
5.28	Desired $a\omega_d$, command $a\omega_c$ and real $a\omega_r$ longitudinal and angular velocity for SM-PF control.	86
5.29	Lateral and angular errors of SM-PF control.	86
6.1	The human response (ride quality) involves human variables as well as dynamic motion and other physical variables, but the ride comfort response and technical evaluation of ride (dis-)comfort involves dynamic motion variables only. Modified from Forstberg [114].	90
6.2	Human head-neck model	94
6.3	Experimental sliding-mode trajectory-tracking control using an EKF-based fusion in the on-line pose estimation.	96
6.4	Cross-spectral density functions for all experiments.	97
6.5	Longitudinal and lateral accelerations from IMU and from encoders.	97
7.1	RobChair platform.	101
7.2	Levels and modules of the motion control system.	102
7.3	RobChair CAN-based hardware architecture.	103
7.4	Robotic wheelchair model and symbols.	106
7.5	Surfaces used in the determination of acceleration limits.	107
7.6	Experimental (green and red) and desired (blue) wheels speed values used to determine the maximum acceleration and deceleration of the RobChair.	108
7.7	Free body diagram showing the RobChair mobile robot (in plane yz).	109
7.8	Free body diagram to find the maximum acceleration before wheel slippage.	110
7.9	Schematic showing the forces acting on RobChair to cause it to move.	112
7.10	Feasible WMR velocities.	113
7.11	Differential drive curvature as function of the wheels speeds.	114
7.12	Linear velocity as function of wheels' speed.	115

7.13	Experimental SM-TT control starting from an initial error state ($x_e(0) = -1, y_e(0) = -1, \phi_e(0) = 0$), under odometry navigation.	117
7.14	Experimental SM-TT control under magnetic-markers navigation: Left) <i>Path</i> - 1; Right) <i>Path</i> - 2. In both paths, the circles represent the positions of the seven magnetic markers used in the experiment.	118
7.15	Experimental SM-PF control under magnetic-markers navigation: Left) <i>Path</i> - 1; Right) <i>Path</i> - 2. In both paths, the circles represent the positions of the seven magnetic markers used in the experiment.	119
7.16	RobChair pictures at different positions in a real experiment.	119
7.17	Desired (v_d, ω_d), command (v_c, ω_c) and real (v_r, ω_r) linear and angular velocities for SM-TT control using an EKF-based fusion in the on-line pose estimation - <i>Path</i> - 1.	120
7.18	Desired (v_d, ω_d), command (v_c, ω_c) and real (v_r, ω_r) linear and angular velocities for SM-TT control using an EKF-based fusion in the on-line pose estimation - <i>Path</i> - 2.	120
7.19	Longitudinal and lateral errors of SM-TT control under magnetic-markers navigation: Left) <i>Path</i> - 1; Right) <i>Path</i> - 2.	120
7.20	Longitudinal and lateral accelerations from IMU and from encoders in case of SM-TT control, Left) <i>Path</i> - 1; Right) <i>Path</i> - 2.	122

List of Abbreviations

CAN	Controller-Area Network
CSD	Cross Spectral Density
DOF	Degree Of Freedom
EKF	Extended Kalman Filter
eVDV	Estimated Vibration Dose Value
FFT	Fast Fourier Transformation
HNC	Head-Neck Complex
IMU	Inertial Measurement Unit
ISO	International Organization for Standardization
ISR	Institute of Systems and Robotics
MCL	Motion Control Level
MPL	Motion Planning Level
MTL	Motion Tracking Level
PSD	Power Spectral Density
rmq	Root Mean Quad
rms	Root Mean Square
SM-PF	Sliding-Mode Path-Following
SM-TT	Sliding-Mode Trajectory-Tracking
SMC	Sliding Mode Control
Tr	Transmissibility
VDV	Vibration Dose Value
VSC	Variable Structure Control
VSS	Variable Structure Systems
WMR	Wheeled Mobile Robot

Chapter 1

Introduction

1.1 Motivation and Background

Everyday more and more robotic vehicles are entering the real world. They are put to work just about everywhere manual vehicles have been used in the past. From agriculture, and mining operations, to inside factories and hospitals, they are increasing safety, efficiency, and performance in all tasks otherwise considered to be too dull, dirty or dangerous for manual labor.

Autonomous vehicles pose a number of unique problems in their design and implementation. There is no longer a human-in-the-loop control scheme for the vehicle. The system itself must close the loop from environment feedback to low-level vehicle control. Where a human operator would normally analyze data feedback from telemetry, remote video, etc. and then decide the best course of action, designers must now instrument the vehicle so that it can automate these tasks. This requires the inclusion of internal state and environmental sensors, along with onboard computers and software capable of processing the sensed information and planning the vehicle's action accordingly.

The first design step is the inclusion of different types of sensors onto the vehicle platform. These sensors serve two general purposes. The first is to measure the state of the vehicle itself, such as its position, orientation, speed, and perhaps also health monitoring information such as comfort, temperature, pressure, etc (proprioception).

The second general purpose is the system's ability to sense information originating outside of itself (exteroception). It is the ability to sense one's environment. Sensors such as cameras and range detectors provide this information. The job of the system designer is to outfit the autonomous vehicle with those sensors necessary and

appropriate to provide the correct environment feedback, thus allowing the system to decide how to act within it.

The second design step is giving the autonomous vehicle the ability to calculate how to react to sensed internal and external information. This step requires the vehicle to have the necessary processing and computational power along with the algorithms and software capable of providing robust and stable control laws that guide the navigation of the robot.

Autonomous vehicles generate their own decisions, at the planning level, that govern how to drive the vehicle actuators, and cause the platform to move.

The problem of motion planning and control is that there must be consideration for the motion constraints of any actuators involved or the vehicle platform itself. This is especially an important issue for car-like vehicles and WMRs because they are subject to nonholonomic constraints. This means that a vehicle driving on a surface may have three degrees of freedom: translation in two dimensions and rotation in one. Consequently, the equations of motion describing the vehicle dynamics are non-integrable, which makes the problem much more difficult to solve. This also means that car-like vehicles and WMRs are under actuated. In other words, the number of control inputs to the system is less than the number of degrees of freedom in the system's configuration space.

Many people nowadays spend a significant proportion of their time travelling and there is an increasing demand for comfort, in private and public transportation. Three classes of factors are considered in the analysis of travelling comfort: organizational, local and riding. The riding comfort can be analysed in three different respects: dynamic factors - related to vibration, shocks and acceleration; ambient factors - thermal comfort, air quality, noise, pressure gradients, etc; spatial factors - dealing with the ergonomics of the passenger's position.

Comfort is a complex definition that contains both physiological and psychological components; this includes the subjective feeling of well being with the absence of discomfort, stress and pain. Comfort not only consists of the absence of negative effects; it is also the experience of positive aspects of comfort. Therefore, comfort includes a form of evaluation, i.e. *it feels well* and has as its opposite, negative sensations. From interviews of vehicle passengers it is obvious that ride comfort is dependent not only on the magnitude but also on the occurrence of occasional shocks or transients.

Ride quality is a person's reaction to a set of physical conditions in a vehicle environment, such as dynamic, ambient and spatial variables. Dynamic variables consist of motions, measured as accelerations and changes (jerk) in accelerations in all three axes (lateral, longitudinal and vertical), angular motions about these axes (roll, pitch and yaw) and sudden motions, such as shocks and jolts. Normally, the axes are fixed to the vehicle body. The ambient variables may include temperature, pressure, air quality and ventilation, as well as noise and high frequency vibrations, while the spatial variables may include workspace, leg room and other seating variables. However, many use the term passenger comfort, ride comfort or average ride comfort for ratings on a ride quality scale regarding the influence of dynamic variables. Normally, higher rating on a ride quality scale means better comfort, whereas higher rating on a ride (dis-)comfort scale means less comfort.

This is the nature of the problem undertaken in this thesis.

The theory of variable structure systems (VSS) opened up a wide new area of development for control designers. Variable structure control (VSC), which is frequently known as sliding mode control (SMC), is characterized by a discontinuous control action which changes structure upon reaching a set of predetermined switching surfaces. This kind of control may result in a very robust system and thus provides a possibility for achieving our goals. Some promising features of SMC are listed below:

- The order of the motion equation can be reduced.
- The motion equation of the sliding mode can be designed linear and homogeneous, despite that the original system may be governed by nonlinear equations.
- The sliding mode does not depend on the process dynamics, but it is determined by parameters selected by the designer.
- Once the sliding motion occurs, the system has invariant properties which make the motion independent of certain system parameter variations and disturbances. Thus the system performance can be completely determined by the dynamics of the sliding manifold.

1.2 Contributions

This work has three main contributions:

- Although motion planning of mobile robots and autonomous vehicles has been thoroughly studied in the last decades, the requisite of producing trajectories with low associated accelerations and jerk is not easily traceable in the technical literature. This thesis addresses this problem proposing an approach that consists of introducing a velocity planning stage to generate adequate time sequences to be used in the interpolating curve planners. In this context, ***it is important to generate speed profiles (linear and angular) that lead to trajectories respecting human comfort.*** The need of having travel comfort in autonomous vehicle' applications, motivated my research on the subject of this thesis.
- In this thesis was proposed ***a new design of sliding surface for sliding-mode trajectory-tracking (SM-TT) and sliding-mode path-following (SM-PF) controller for WMR and car-like vehicle.*** Due to their non-holonomic properties, restricted mobility and their relevance in applications, the trajectory-tracking of those systems has been a challenging class of control problems. Variable structure control emerges as a robust approach in different applications and has been successfully applied to control problems as diverse as automatic flight control, control of electrical motors, regulation in chemical processes, helicopter stability augmentation, space systems and robotics. One particular type of VCS system is the sliding mode control methodology. The theory of SMC has been applied to various control systems, since it has been shown that this nonlinear type of control exhibits many excellent properties, such as robustness against large parameter variation and disturbances.
- The transmission of the acceleration to the head-neck complex (HNC) in the seated human body is a cause of discomfort and motion sickness in vehicles. The seat back, by limiting the horizontal and rotational motion of the trunk, increases the transmission of the trunk horizontal acceleration to the HNC. This may has considerable influence on discomfort. The present thesis ***analyzes the comfort of wheelchair users when a SM-TT or a SM-PF controller is used.*** The user comfort is examined not only in the time domain (using the transmissibility parameter), but also in the frequency domain. For measuring accelerations of the real intelligent wheelchair (platform used in real experiments), a three-dimensional inertial sensor was used.

Moreover a set of experimental tests using an intelligent wheelchair, called RobChair, has been performed to evaluate the performance of the SM-TT/SM-PF controller and the trajectory planning algorithm, with comfort constraint. RobChair prototype has been developed for allowing experimental studies on rehabilitation applications and mobility assistance of people with special needs (e.g. people with severely impaired motion skills), with the purpose of providing them with a certain degree of autonomy and independence. RobChair is based on a commercial wheelchair, which has been equipped with an intelligent control system and several sensors.

1.3 Outline of the Thesis

The thesis is structured as follows:

- **Chapter 2:** Trajectory tracking problems are summarized.
- **Chapter 3:** Kinematic and dynamic modeling of the WMRs and car-like robots are presented.
- **Chapter 4:** The concept of sliding mode are first introduced. Then the fundamentals of SMC are summarized, including basic definitions, methods of sliding surface and control law design, robustness properties and the methods on handling chattering problems. New sliding-mode trajectory-tracking and sliding-mode path-following controllers for WMRs and car-like vehicles, are also proposed in this chapter.
- **Chapter 5:** The trajectory/path planning are developed, including the velocity profile.
- **Chapter 6:** A model with two freedom degrees is considered for the HNC model. The user comfort is examined not only in the time domain, but also in the frequency domain.
- **Chapter 7:** Experimental results obtained with the implementation of the proposed controllers in RobChair are summarized and discussed.
- **Chapter 8:** Finally, conclusions are drawn and some suggestions for future work are provided.

Chapter 2

Trajectory Tracking Problems

2.1 Related Works

Control problems involving mobile robots have attracted considerable attention in the control community. Most wheeled mobile robots can be classified as nonholonomic mechanical systems. Controlling such systems is, however, simple. The challenge presented by these problems comes from the fact that a motion of a wheeled mobile robot in a plane possesses three degrees of freedom (DOF); while it has to be controlled using only two control inputs under the nonholonomic constraint.

The methods used in recent years to solve mobile robot control problems can be classified into three categories. The first category is the sensor-based control approach to navigation problems. The emphasis is on interactive motion planning in dynamic environments [1, 2]. Because the working environment for mobile robots is unstructured and may change with time, the robot must use its on-board sensors to cope with the dynamic environment. Most reported designs following this approach rely on intelligent control schemes, such as fuzzy logic control [3, 4, 5] and neural-network learning control [6, 7]. Obstacle motion estimation and environment configuration prediction using sensory information are important for proper motion planning. However, since a mobile robot responds to its surroundings in a reactive or reflexive way; the executed trajectory may not be globally optimized.

In the second category, the navigation problem is decomposed into a path planning phase and a path execution phase. A collision-free path is generated and executed based on a prior map of the environment. The executed path is planned using certain optimization algorithms based on a minimal time, minimal distance or minimal energy performance index. Methods for avoiding both static and moving obstacles have been

reported in the literature [8, 9, 10, 11, 12]. In these methods, a collision-free path is planned according to the environment map space-time relations. The mobile robot must follow the planned path employing a path-following controller.

The third category follows the motion control approach, in which a desired trajectory must be tracked accurately. Among these, tracking controller designs employing a simplified linear model have been reported [13, 14]. In the linear model approach, however, the controller works only when the linear velocity is not zero. Under such circumstances, it would be difficult to control the mobile robot to track the specified trajectory and in the mean time stop with the specified pose. Consequently a more generalized approach is desirable. Nonlinear system theory has been employed to solve this problem. Two main research directions employing nonlinear control design can be distinguished. The first, initiated by Bloch et al. [15], used discontinuous feedback, whereas the second research direction used time-varying continuous feedback, which was first investigated by Samson [16]. Pomet [17] then proposed several smooth feedback control laws. However, though these solve the regulation problem, they were found to yield slow asymptotic convergence. In order to obtain faster convergence (e.g., exponential convergence), an alternative approach was initially proposed by MCloskey and Murray [18] and taken up in several subsequent studies.

Research on the tracking problem for mobile robots has been extensive. Using Barbalats lemma or the backstepping method, control schemes have been proposed for mobile robots to globally follow special paths such as circles and straight lines. In practical applications, it is preferable to solve the tracking problem and the regulation problem simultaneously using a single controller; otherwise, switching between two different types of controllers will be necessary.

Tracking control of nonholonomic mobile robots aims at controlling robots to track a given time varying trajectory (reference trajectory). It is a fundamental motion control problem and has been intensively investigated in the robotic community.

Based on whether the system is described by a kinematic model or a dynamic model, the tracking control problem is classified as either a kinematic or a dynamic tracking control problem. Several researchers have studied the kinematic tracking problem and proposed several controllers. Using the kinematic model of WMRs the trajectory-tracking problem was solved by Kanayama et al. [19]. Both the local and global tracking problems with exponential convergence have been solved theoretically using time varying state feedback based on the backstepping technique by Jiang and Nijmeijer [20].

The kinematic tracking control problem of WMR has been widely studied whereas dynamic tracking control problem has received attention only recently. Most of the results on dynamic model based tracking problem of non-holonomic systems are proposed assuming that the kinematics of the system are exactly known and uncertainties are present only in the dynamics. But practically speaking, uncertainties are present in both the kinematics and dynamics.

Usually, the reference trajectory is obtained by using a reference (virtual) robot; therefore, all the kinematic constraints are implicitly considered by the reference trajectory. The control inputs are mostly obtained by a combination of feedforward inputs, calculated from reference trajectory, and feedback control law, as in [21, 22, 23]. Lyapunov stable time-varying state-tracking control laws were pioneered by [19, 16, 24], where the systems equations are linearized with respect to the reference trajectory, and by defining the desired parameters of the characteristic polynomial the controller parameters are calculated. The stabilization to the reference trajectory requires a nonzero motion condition.

A discontinuous stabilizing controller for WMRs with nonholonomic constraints where the state of the robot asymptotically converges to the target configuration with a smooth trajectory was presented by Zhang and Hirschorn [25]. A tracking problem was formulated by Koh and Cho [26] for a mobile robot to follow a virtual target vehicle that is moved exactly along the path with specified velocity. The driving velocity control law was designed based on bang-bang control considering the acceleration bounds of driving wheels and the robot dynamic constraints in order to avoid wheel slippage or mechanical damage during navigation. Zhang, et al. [27] employed a dynamic modeling to design a tracking controller for a differentially steered mobile robot that is subject to wheel slip and external loads.

Various nonlinear control techniques have been used by many researchers considering the system disturbances and unknown dynamic parameters. Sliding mode motion control technique by Yang and Kim [28], robust adaptive control technique by Kim et al. [29], adaptive control technique by Fukao et al. [30] and higher order sliding mode technique by Li and Chao [32] have been used to solve the tracking control problem for WMRs.

A solution for the trajectory tracking problem for a WMR in the presence of disturbances that violate the nonholonomic constraint based on discrete-time sliding mode control [33]. An electromagnetic approach for path guidance of a mobile-robot-based automatic transport service system with a PD control algorithm was investigated by

Wu, et al. [34]. Jiang, et al. [35] developed a model-based control design strategy that deals with global stabilization and global tracking control for the kinematic model with a nonholonomic WMR in the presence of input saturations.

Adaptive controls are derived for mobile robots, using backstepping technique, for tracking of a reference trajectory and stabilization to a fixed posture by Pourboghraat and Karlsson [36]. In [37], Dong and Kuhnert propose a robust adaptive controller with the aid of backstepping technique and neural networks.

The trajectory tracking algorithms presented in the above literature share a common idea of defining velocity control inputs, which stabilize the closed loop system.

In industrial and manufacturing applications, time and speed are very important parameters when calculating the productivity and efficiency of a process. Hence, in the trajectory tracking control problem it is a requirement that the WMR be able to track a time-indexed trajectory. In such cases motion control is commonly achieved with a velocity profile.

2.2 Motivation

For many years, the control of non-holonomic vehicles has been a very active research field. At least two reasons account for this fact. On one hand, wheeled vehicles constitute a major and ever more ubiquitous transportation system. Previously restricted to research laboratories and factories, automated wheeled vehicles are now envisioned in everyday life (e.g. through car-platooning applications or urban transportation services), not to mention the military domain.

These novel applications, which require coordination between multiple agents, give rise to new control problems. On the other hand, the kinematic equations of non-holonomic systems are highly nonlinear, and thus of particular interest for the development of nonlinear control theory and practice. Furthermore, some of the control methods initially developed for non-holonomic systems have proven to be applicable to other physical systems (e.g. underactuated mechanical systems), as well as to more general classes of nonlinear systems.

The present thesis addresses sliding-mode control of non-holonomic vehicles, and more specifically trajectory tracking, by which we mean the problem of stabilizing the state, or an output function of the state, to a desired reference value, possibly time-varying.

For controllable linear systems, linear state feedbacks provide, simple, efficient,

and robust control solutions. By contrast, for non-holonomic systems, different types of feedback laws have been proposed, each one carrying its specific advantages and limitations. As a consequence, the choice of a control approach for a given application is a matter of compromise, depending on the system characteristics and the performance requirements.

In the European Union there are about 80 million elderly or disabled people. Various reports also show that there is a strong relation between the age of the person and the handicaps suffered, the latter being commoner in persons of advanced age. Given the growth in life expectancy in the EU, this means that a large part of its population will experience functional problems. Aware of the dearth of applications for this sector of the population, governments and public institutions have been promoting research in this line in this recent years. Various types of research groups at a world level have begun to set up cooperation projects, projects to aid communication and mobility of elderly and/or disabled persons with the aim of increasing their quality of life and allowing them a more autonomous and independent lifestyle and greater chances of social integration.

One of the most potentially useful applications for increasing the mobility of disabled and/or elderly persons is wheelchair implementation. A standard motorized wheelchair aids the mobility of disabled people who cannot walk, always providing that their disability allows them to control the joystick safely. Persons with a serious disability or handicap, however, may find it difficult or impossible to use them; cases in point could be tetraplegics who are capable only of handling an onoff sensor or make certain very limited movements. This would make control of the wheelchair particularly difficult, especially on delicate manoeuvres. For such cases it is necessary to develop more complex human-wheelchair interfaces adapted to the disability of the user, thus allowing them to input movement commands in a safe and simple way.

Chapter 3

Kinematic and Dynamic Models for Differential-drive and Car-like Mobile Robots

In this section, a review of modeling and control of nonholonomic mobile robots is provided. In such robots, the motion control will be subject to nonholonomic constraints, which make motion perpendicular to the wheels impossible. This constraint involves a nontrivial control method although the full state be measured.

3.1 Kinematic and Dynamic Modeling for Differential-drive Robots

A mobile robot system having an n -dimensional configuration space with generalized variables (q_1, q_2, \dots, q_n) and subject to constraints can be described by [38]:

$$M(q) \cdot \ddot{q} + V_m(q, \dot{q}) \cdot \dot{q} + F(\dot{q}) + G(q) + \tau_d = B(q) \cdot \tau - A^T(q) \cdot \lambda \quad (3.1)$$

where $M(q) \in R^{n \times n}$ is a symmetric, positive definite inertia matrix, $V_m(q, \dot{q}) \in R^{n \times n}$ is the centripetal and Coriolis matrix, $F(\dot{q}) \in R^{n \times 1}$ denotes the surface friction, $G(q) \in R^{n \times 1}$ is the gravitational vector, τ_d denotes bounded unknown disturbances including unstructured unmodeled dynamics, $B(q) \in R^{n \times r}$ is the input transformation matrix, $\tau \in R^{n \times 1}$ is the input vector, $A(q) \in R^{m \times n}$ is the matrix associated with the constraints, and, $\lambda \in R^{m \times 1}$ is the vector of constraint forces. The nonholonomic

nature of a mobile robot is related to the assumption that the wheels of the vehicle roll without skidding. They are subject to non-integrable equality nonholonomic constraints involving the velocity. In other words, the dimension of the admissible velocity space is smaller than the dimension of the configuration space. This constraint can be written as:

$$A(q) \cdot \dot{q} = 0 \quad (3.2)$$

In the case of a differential-drive WMR, the model used in [30] and [31] is used in this thesis. Consider the mobile robot of Figure 3.1, $O - xy$ is the world coordinate system and $P_0 - XY$ is the coordinate system fixed to the mobile robot. P_0 is the origin of the coordinate system $P_0 - XY$ fixed at the middle point between the right and left driving wheels. The distance from P_0 to the center of mass P_c is d .

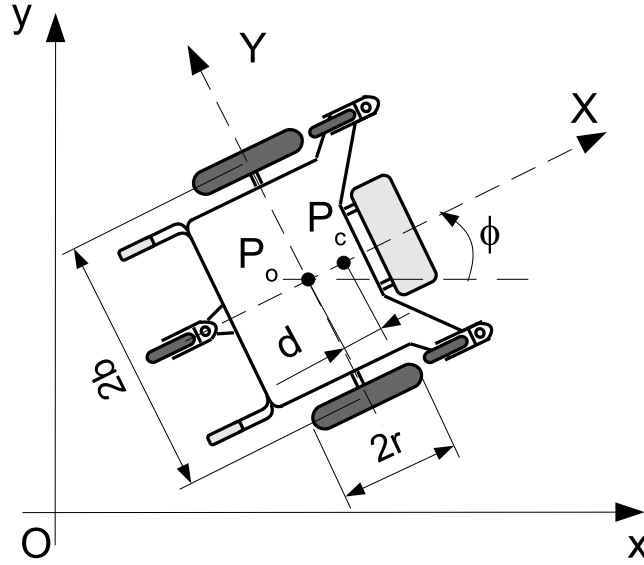


Figure 3.1: WMR model and symbols.

We assume the wheels roll and do not skid. Then, there are three constraints; the velocity of P_0 must be in the direction of the axis of symmetry and the wheels must not skid:

$$\dot{y} \cdot \cos\phi - \dot{x} \cdot \sin\phi - d \cdot \dot{\phi} = 0 \quad (3.3)$$

$$\dot{x} \cdot \cos\phi + \dot{y} \cdot \sin\phi + b \cdot \dot{\phi} = r \cdot \dot{\theta}_r \quad (3.4)$$

$$\dot{x} \cdot \cos\phi + \dot{y} \cdot \sin\phi - b \cdot \dot{\phi} = r \cdot \dot{\theta}_l \quad (3.5)$$

which can be rewritten in the matrix form (3.2) with:

$$A(q) = \begin{bmatrix} \sin\phi & -\cos\phi & d & 0 & 0 \\ \cos\phi & \sin\phi & b & -r & 0 \\ \cos\phi & \sin\phi & -b & 0 & -r \end{bmatrix}$$

The system (3.1) can be rewritten as follows:

$$M(q) \cdot \ddot{q} + V_m(q, \dot{q}) \cdot \dot{q} = B(q) \cdot \tau - A^T(q) \cdot \lambda \quad (3.6)$$

For the later description, m_c is the mass of the robot's body and m_w is the mass of a driving wheel plus its associated motor; I_c , I_w , and I_m are the moment of inertia of the body about the vertical axis through P_c , the wheel with a motor about the wheel axis, and the wheel with a motor about the wheel diameter, respectively. The matrices M , V_m and B are given by:

$$M(q) = \begin{bmatrix} m & 0 & 2 \cdot m_w \cdot d \cdot \sin\phi & 0 & 0 \\ 0 & m & -2 \cdot m_w \cdot d \cdot \cos\phi & 0 & 0 \\ 2 \cdot m_w \cdot d \cdot \sin\phi & -2 \cdot m_w \cdot d \cdot \cos\phi & I & 0 & 0 \\ 0 & 0 & 0 & I_w & 0 \\ 0 & 0 & 0 & 0 & I_w \end{bmatrix}$$

$$V_m(q, \dot{q}) = \begin{bmatrix} 2 \cdot m_w \cdot d \cdot \dot{\phi}^2 \cdot \cos\phi \\ 2 \cdot m_w \cdot d \cdot \dot{\phi}^2 \cdot \sin\phi \\ 0 \\ 0 \\ 0 \end{bmatrix}, \quad B(q) = \begin{bmatrix} 0 & 0 \\ 0 & 0 \\ 0 & 0 \\ 1 & 0 \\ 0 & 1 \end{bmatrix}, \quad \tau = \begin{bmatrix} \tau_r \\ \tau_l \end{bmatrix}$$

Where I and m are given by: $I = m_c \cdot d^2 + I_c + 2 \cdot m_w \cdot b^2 + 2 \cdot I_m$, $m = m_c + 2 \cdot m_w$.

Five generalized coordinates can describe the configuration of the mobile robot: $q = [x, y, \phi, \theta_r, \theta_l]^T$, where (x, y) are the coordinates of P_0 , ϕ is the heading angle of the mobile robot, and θ_r, θ_l are the angles of the right and left driving wheels.

Let $S(q)$ be a full rank matrix formed by a set of smooth and linearly independent vectors such as:

$$S^T(q) \cdot A^T(q) = 0 \quad (3.7)$$

It is easy to verify that $S(q)$ is given by:

$$S(q) = \begin{bmatrix} \frac{r}{2b} \cdot (b \cdot \cos\phi - d \cdot \sin\phi) & \frac{r}{2b} \cdot (b \cdot \cos\phi + d \cdot \sin\phi) \\ \frac{r}{2b} \cdot (b \cdot \sin\phi + d \cdot \cos\phi) & \frac{r}{2b} \cdot (b \cdot \sin\phi - d \cdot \cos\phi) \\ \frac{r}{2b} & -\frac{r}{2b} \\ 1 & 0 \\ 0 & 1 \end{bmatrix}$$

According to (3.1) and (3.7), it is possible to find that:

$$\dot{q} = S(q) \cdot \nu \quad (3.8)$$

where $\nu = [\nu_1 \ \nu_2]$ whose elements are the angular velocities of the right and left wheels. Equation (3.8) represents the kinematic model of the robot. Differentiating (3.8), substituting the result in (3.1), and then multiplying by S^T , we can eliminate the constraint matrix $A^T(q) \cdot \lambda$. Also, if we denote $\bar{M} = S^T \cdot M \cdot S$ and $\bar{V}_m = S^T \cdot (M \cdot \dot{S} + V_m \cdot S)$, and after simplifications, the nonholonomic mobile robot model (3.1) can be written in the form of:

$$\bar{M}(q) \cdot \dot{\nu} + \bar{V}_m(q, \dot{q}) \cdot \nu = \bar{B}(q) \cdot \tau \quad (3.9)$$

where

$$\bar{M}(q) = \begin{bmatrix} \frac{r^2}{4b^2} \cdot (m \cdot b^2 + I) + I_w & \frac{r^2}{4b^2} \cdot (m \cdot b^2 - I) \\ \frac{r^2}{4b^2} \cdot (m \cdot b^2 - I) & \frac{r^2}{4b^2} \cdot (m \cdot b^2 + I) + I_w \end{bmatrix}$$

$$\bar{V}_m = \begin{bmatrix} 0 & \frac{r^2}{2b} \cdot m_c \cdot d \cdot \dot{\phi} \\ -\frac{r^2}{2b} \cdot m_c \cdot d \cdot \dot{\phi} & 0 \end{bmatrix}, \quad \bar{B} = \begin{bmatrix} 1 & 0 \\ 0 & 1 \end{bmatrix}, \quad \tau = \begin{bmatrix} \tau_r \\ \tau_l \end{bmatrix}$$

Equations (3.8) and (3.9) represent the kinematic and dynamic models of the robot, respectively. From equation (3.8) we can obtain that:

$$\frac{d}{dt} \begin{bmatrix} x \\ y \\ \phi \\ \theta_r \\ \theta_l \end{bmatrix} = \begin{bmatrix} \frac{r}{2} \cdot \cos\phi & \frac{r}{2} \cdot \cos\phi \\ \frac{r}{2} \cdot \sin\phi & \frac{r}{2} \cdot \sin\phi \\ \frac{r}{2b} & -\frac{r}{2b} \\ 1 & 0 \\ 0 & 1 \end{bmatrix} \cdot \begin{bmatrix} \nu_1 \\ \nu_2 \end{bmatrix} \quad (3.10)$$

The relation between (v, w) and (ν_1, ν_2) is:

$$\begin{bmatrix} \nu_1 \\ \nu_2 \end{bmatrix} = \begin{bmatrix} \frac{1}{r} & \frac{b}{r} \\ \frac{1}{r} & -\frac{b}{r} \end{bmatrix} \cdot \begin{bmatrix} v \\ \omega \end{bmatrix} \quad (3.11)$$

where v and ω are the linear and angular velocity of the robot. If we want to focus only on x , y , and ϕ then it is sufficient to substitute (3.11) in (3.10). We will get the ordinary form of a mobile robot with two actuated wheels:

$$\frac{d}{dt} \begin{bmatrix} x \\ y \\ \phi \end{bmatrix} = \begin{bmatrix} \cos\phi & 0 \\ \sin\phi & 0 \\ 0 & 1 \end{bmatrix} \cdot \begin{bmatrix} v \\ \omega \end{bmatrix} \quad (3.12)$$

3.2 Motion Control for WMR

Motion control of mobile robots has been studied by many authors in the last decade, since they are increasingly used in wide range of applications. At the beginning, the research effort was focused only on the kinematic model, assuming that there is perfect velocity tracking [38]. The main objective was to find suitable velocity control inputs, which stabilize the kinematic closed loop control. Later on, the research was conducted to design motion controllers, including also the dynamics of the robot. However, when the dynamics part is considered, exact knowledge about the parameters values of the mobile robot is almost unattainable in practice. If we consider that during the robot motion, these parameters may change due to surface friction, additional load, among others, the problem becomes more complicated. Furthermore, the control at the kinematic level may be unstable if there are control errors at the dynamic level. Therefore, the control at the dynamic level is at least as important as the kinematic-level control. At present, PID controllers are still widely used in motor control of mobile robots and in industrial control systems in general. However, its ability to cope with some complex process properties such as non-linearities, and time-varying parameters is known to be very poor. Recently, some investigations have been conducted to design non-linear dynamic controllers. Instead of using approximate linear models as in the design of conventional linear controllers, non-linear models are used and non-linear feedbacks are employed on the control loop. Using non-linear controllers, system stability can be improved significantly; a few results are available in [30] and [39]. However, nonlinear controllers have a more complicated structure, and are more difficult to find and to implement.

In motion control, the objective is to control the velocity of the robot such that its pose $P = [x, y, \phi]^T$ follows a reference trajectory $P_r = [x_r, y_r, \phi_r]^T$. At the beginning, the research effort was focused only on the kinematic model, assuming that there is perfect velocity tracking. Thus, the controllers neglect the vehicle dynamics and

consider only the steering system (3.12), where the velocities (v, w) are supposed to be the robot inputs (Fig 3.2). Various feedback controllers have been proposed to solve this problem (see the survey paper [38] and references cited therein).

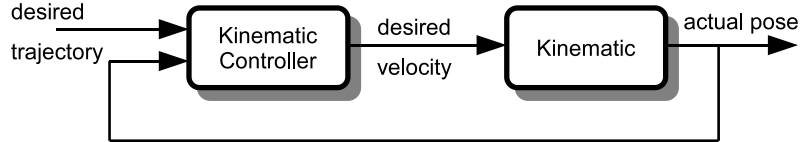


Figure 3.2: Motion control using the kinematic model.

Later on, the research was conducted to design motion controllers, including also the dynamics of the robot. In a real case, the mobile robot is described with two stages. As shown in Figure 3.3, the first stage contains the dynamics, with two outputs (v, w) linear and angular velocity. The second stage contains the kinematics.



Figure 3.3: Two-stage model of a real mobile robot.

To have better motion control performance one has to take into account also the specific vehicle dynamics. In this case the controller structure should be decomposed into two stages:

a) an inner loop (Figure 3.4), depending on the robot dynamics, that can be used for controlling the linear and angular velocities. It is also called dynamic-level control of a mobile robot;

b) an outer loop to control the pose of the robot. It is also called kinematic-level control of a mobile robot.

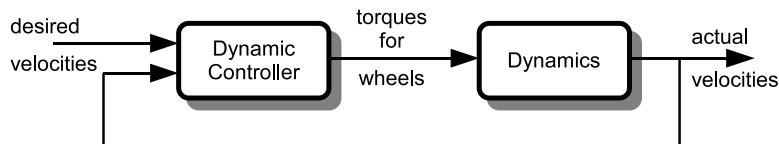


Figure 3.4: Inner loop control of a mobile robot (dynamic-level control).

The global control structure is then composed as presented in Figure 3.5.

When the dynamic model is considered, exact knowledge about the parameters values of the mobile robot dynamics is almost unattainable in practical situations.

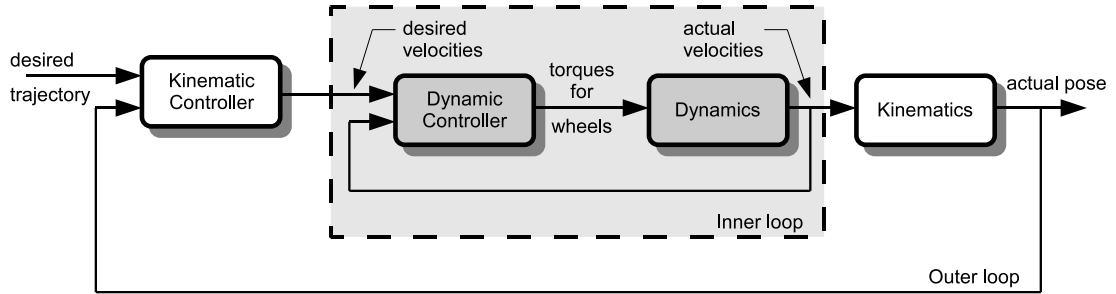


Figure 3.5: Control of a real mobile robot.

If we consider that these parameters are time varying, the problem becomes more complicated.

In [15] it was first demonstrated that a nonholonomic system cannot be stabilized to a single equilibrium point by a continuous (smooth) time-invariant pure state feedback law, derived from a violation of Brockett's necessary condition for stabilizability. Furthermore, a WMR is only small time locally controllable [15], and it is a controllable system regardless of the structure of the nonholonomic constraints [42]. Therefore, choices for control are limited to using: (a) discontinuous time invariant feedback laws or (b) continuous but time varying non linear feedback control laws.

Various problems related to motion control of autonomous vehicles (including air, land, and marine robots) have been studied extensively in recent years. The problems addressed in the literature can be roughly classified into three groups:

- point stabilization - the goal is to stabilize the vehicle at a given target point, with a desired orientation;
- trajectory tracking - the vehicle is required to track a time parameterized reference;
- path following - the vehicle is required to converge to and follow a path, without any temporal specifications.

Point stabilization presents a true challenge to control system designers when the vehicle has nonholonomic constraints, since that goal cannot be achieved with smooth (or even continuous) state-feedback control laws, as pointed out in [43]. To overcome this difficulty, two main approaches have been proposed: smooth time-varying control laws [44], [45] and discontinuous and hybrid feedback laws [46], [47], [48].

The *trajectory tracking* problem for fully actuated systems is now well understood and satisfactory solutions can be found in advanced nonlinear control textbooks.

However, in the case of underactuated vehicles, that is, when the vehicles have less actuators than state variables to be tracked, the problem is still a very active topic of research. Linearization and feedback linearization methods [49], [50] as well as Lyapunov based control laws [44], [51] have been proposed.

Path following control has received relatively less attention in the literature. See [52], [53] for pioneering work in the area as well as [44], [54] and the references therein. The underlying assumption in path following control is that the vehicles forward speed tracks a desired speed profile, while the controller acts on the vehicle orientation to drive it to the path. Typically, smoother convergence to a path is achieved (when compared to the behaviour obtained with trajectory tracking control laws) and the control signals are less likely pushed to saturation.

3.2.1 Point Stabilization

The challenge is that nonholonomic mobile robot systems have more degrees of freedom than controls. When represented in Cartesian space, they cannot be stabilized with a continuously differentiable, time-invariant feedback control law as pointed out in the famous paper by Brockett [43]. Various approaches have been undertaken to stabilize these systems such as time-varying [63], adaptive [55], [37] discontinuous [56], and neural network based [57] strategies. For a thorough survey of nonholonomic control techniques see the review in [39].

The various strategies may be broken up into three basic types: discontinuous time-invariant, continuous time-varying, and hybrid techniques that are some combination of the other two. All of the techniques make use of the fact that Brockett's Theorem shows that feedback stabilization is achievable if there is a discontinuity introduced in either the control law or time.

Discontinuous time-invariant techniques are of two basic types: piecewise continuous and sliding mode controllers. Sliding mode controllers can provide good convergence rates by forcing the trajectory to slide on a manifold towards equilibrium, but often have problems with chatter as the controller switches control laws along the manifold. Piecewise continuous controllers are of several types, but most make use of a coordinate transformation introducing a discontinuity at the origin [58], [59], [60]. These controllers offer exponential convergence rates without the problem of chatter experienced by sliding mode control, and generally produce smooth natural looking paths [61].

The time-varying control laws that have been developed generally suffer from two problems. Firstly, since time is discontinuous, exponential convergence usually cannot be guaranteed. Hence, these controllers normally suffer from slow convergence rates [39]. Second, the paths generated by this type of controller are generally not smooth or natural looking. They would require a robot with a high degree of maneuverability to follow the generated paths. Most of the hybrid techniques also suffer from these two problems.

Many of the proposed techniques make the simplifying assumption that the mobile robot is a simple unicycle vehicle type. These techniques are therefore well suited to vehicles with only one axle to control, the ability to perform a zero radius turn, and easily reverse direction.

3.2.2 Trajectory Tracking

Trajectory tracking (TT) has been well studied because it is similar to servosystems, and it is guaranteed that the system will converge to the desired trajectory in a deterministic time using an asymptotically stable control law (except for the perturbations that it may suffer). On the other hand, path following (PF) is not well suited for systems with strict timing requirements, but it is very suitable for nonholonomic systems and is applicable to many mobile robots since they are not usually involved in hard real-time systems. Although the first approach seems to be the most straightforward, it has been shown that the second is more suitable for many situations in which time is not a critical parameter.

This is the case for most applications in mobile industrial robots or assistant robots such as computerized wheelchairs (see Fig 3.6). This situation can be understood if we consider the following example in TT systems: if big perturbations force the system to be at rest, the desired point for trajectory tracking will move unavoidably. This means that errors will increase to some value that may introduce instability. On the other hand, if PF were used, the desired point will be the same despite these perturbations, because the paths shape and the real robot state remain the same. This allows the system to overcome large perturbations, avoiding possible unstable states. Thus interest in PF for mobile robots is rapidly growing.

Sliding-mode controllers have been devised by [65] for holonomic robots and extended for nonholonomic robots. Sliding-mode motion control technique by Yang and Kim [28], robust adaptive control technique by Kim et al. [29], adaptive control

technique by Fukao et al. [30] and higher order sliding mode technique by Li and Chao [32] have been used to solve the trajectory-tracking control problem for WMRs.

In [37], Dong and Kuhnert propose a robust adaptive controller with the aid of backstepping technique and neural networks.

Feedback linearization techniques have been used in [23] and [66]. Asymptotic stability in trajectory-tracking using time-varying backstepping was demonstrated by [67], though the convergence was only to a neighborhood of the desired trajectory. Biologically inspired and neural-network based control strategies are presented in [68].

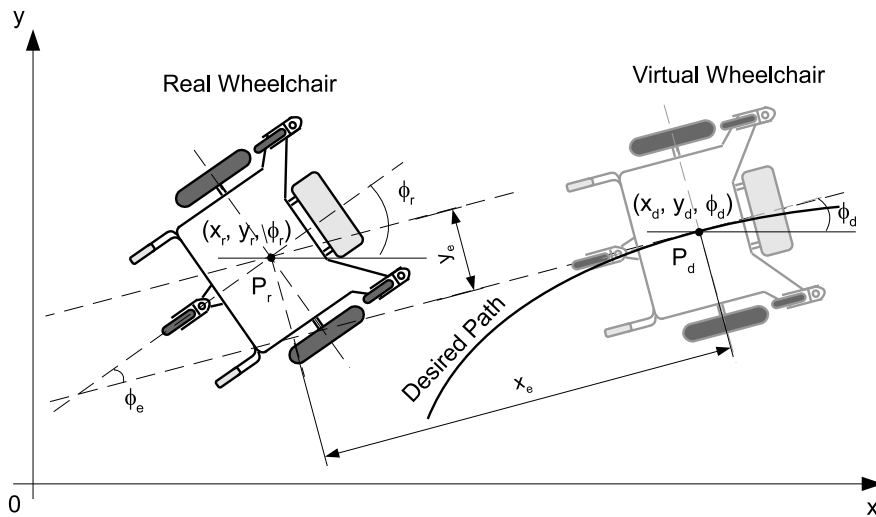


Figure 3.6: Description of the Trajectory Tracking Problem.

3.2.3 Path Following

The virtues of PF can be understood considering this example: if big perturbations force the system to be at rest, for TT the desired point will move unavoidably. This means that errors will increase to some value that may introduce instability. On the other hand, if PF is used, the desired point will be the same in spite of these perturbations. This allows the system to overcome large perturbations avoiding possible unstable states.

In mobile robots it is usual that the trajectory is memorized or previously generated by a path planner module.

The most important path following strategy can be summarized in the following categories:

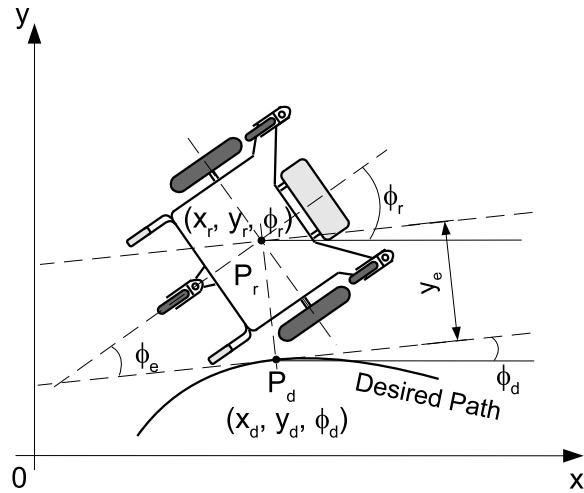


Figure 3.7: Description of the Path Following Problem.

1. In a first category [44], [52], [62], [63] the desired point in the path is obtained through a normal projection along the vector that we have called n . Therefore this projection chooses the point of the desired path that has a null x_e coordinate (see Fig. 3.7). Articles in this category impose a constant value for the variable v_r to guarantee that the system always moves. Finally an asymptotically convergent control law is obtained and behavior for desired paths composed of circles and lines is shown through simulation. Paths containing circles with a small radius (usually call turns with a null radius and infinite curvature “zero-radius turns”) are prohibited, so it is ensured that the normal projection exists and is unique.
2. Another point of view for the projection [64] is to transform the kinematic equations of the mobile robot into a new time scale. In particular, the time scale is chosen to be identical to the distance along the desired path. However the desired paths are limited to straight lines, because the authors are concerned with the tracking of lines and the parking maneuver in a garage. The authors show that the new scale (the distance along the desired path) represents the desired posture obtained through the normal projection.
3. In the last category [23] the projection point chosen by the authors is the one that minimizes the Euclidean distance between the real and the desired points (see Fig. 3.8). Using point P_{Lh} they avoid paths with curvature tending to infinite. Again these authors obtain good convergence results for several paths

(circles and lines) through a feedback linearization control law. But this strategy fails when the desired path is a turn around point P_r .

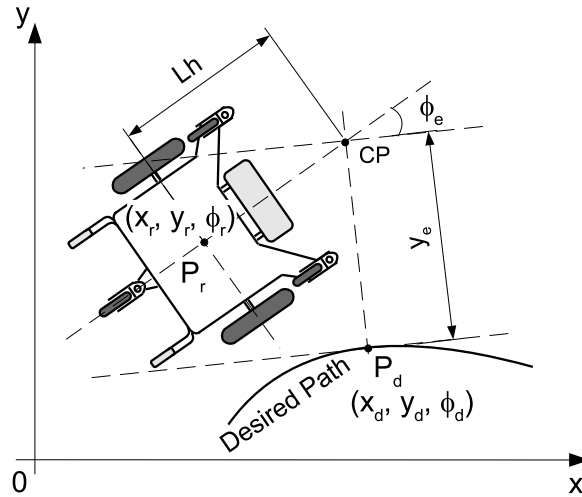


Figure 3.8: Description of the Path Following problem with look-ahead distance.

The main characteristics that must rule PF and that differentiate it from TT, can be summarized as follows:

1. Only the global shape of the path is considered to do the following. The desired trajectory evolution (governed by time) must not play any role in the track as it does in TT.
2. In opposition to TT (where the desired posture is exactly determined by the time), in PF we must choose some relationship to determine the desired posture. Usually this relationship is called *projecting function* as it projects the actual posture to the reference (or desired) path. A classical example of *projecting function* is the normal projection described in [44] and [52], equivalent to making e_x null. That is, the first error coordinate x_e , is eliminated and the robot posture is expressed by only two: y_e and ϕ_e .
3. If the robot stops, the reference or goal point must also stop, as the parameter P_d does not grow by itself. The progress of P_d must not be independent (as in TT) but dependent on the real robot movement, that is \dot{P}_d equation must be driftless.
4. The existence of the rigid law $P_d = P_d(t)$ in TT understand *pulling* or *dragging* the robot to reach the reference. On the other hand, in PF the reference path

can not *pull* (or *drag*) the robot: the robot must move independently by some condition (of course, meanwhile a control law must ensure convergence to the path). We must impose a motion in the real system to guarantee that it moves or progresses. In the current mobile robot literature most motion exigencies are applied to WMR robots, so it is usual to have $v_d = ct$ (other authors use $|v_d| \neq 0$) or a velocity profile for v_d is supposed to be given between the initial and final position.

5. A direct result of what is explained before is that there is no time exigency in the following. This means that we cannot ensure that the robot will reach a reference point in a predictable period of time.

3.3 Kinematic and Dynamic Modeling for Car-like Vehicle

A nonholonomic kinematic model of a vehicle is tackled in this section. The sideslip of the vehicle and lateral slips of the wheels are taken into account while discussing the nonholonomic constraints. To discuss a nonholonomic kinematic model of a vehicle, the following assumptions are considered: a) distances between wheels (generally called as wheelbase or tread) are strictly fixed; b) the steering axle of each wheel is perpendicular to a surface terrain; c) a vehicle does not consist of any flexible parts.

A kinematic model of vehicle including the lateral slips is shown in Fig. 3.9A. In this model, each wheel has a certain steering angle δ_i and slip angle β_i . The slip angle, which defines how large the wheel generates the lateral slip, is calculated by the longitudinal and lateral linear velocities $v_{x_{wi}}$, $v_{y_{wi}}$ of the wheel as follows:

$$\beta_i = \tan^{-1} \left(\frac{v_{y_{wi}}}{v_{x_{wi}}} \right) \quad (3.13)$$

The subscript i denotes each wheel ID as shown in Fig. 3.9A. (x_{CG}, y_{CG}, ψ) defines the position and an orientation of the center of gravity of the vehicle (CG), while (x_{wi}, y_{wi}) defines the position of the i -th wheel. v and v_i are linear velocities of the vehicle and each wheel, respectively. Also, β denotes the sideslip of the vehicle, which is determined by a similar equation of (3.13). l_f and l_r means the longitudinal distance from the center of gravity of the vehicle to the front or rear wheels and d defines the wheelbase. Here, based on the assumption as previously pointed, l_f , l_r

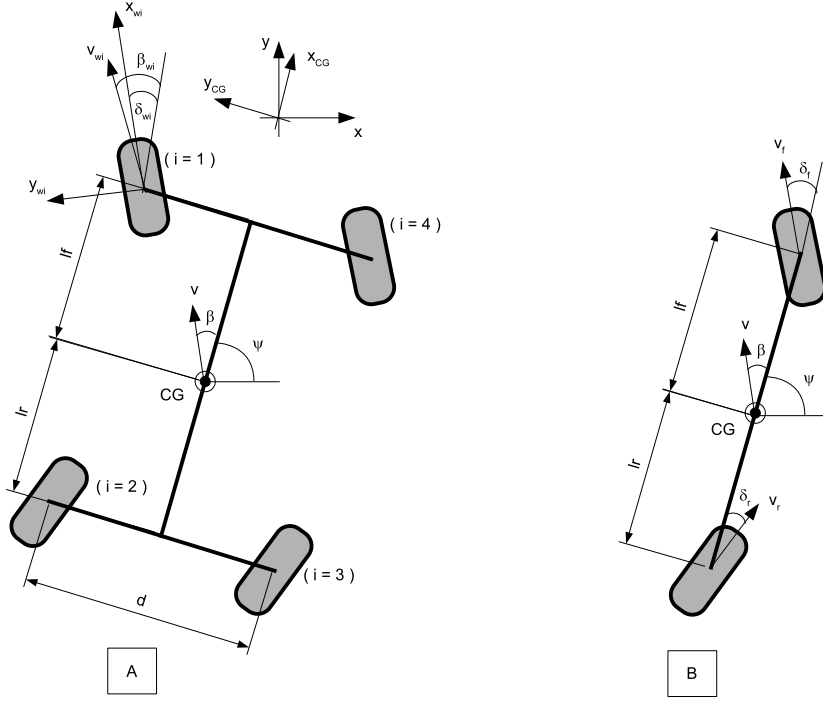


Figure 3.9: Kinematics model of A) 4 wheel vehicle; B) Bicycle model.

and d take constant values.

Nonholonomic constraints

In the conventional approach, Bicycle model [69], a four-wheel car-like vehicle is approximated as a two-wheel bicycle-like vehicle. However, the bicycle model is hardly able to deal with the slips of each wheel, strictly. Therefore, taking into account the slips, the nonholonomic constraints are expressed by:

$$\dot{x}_{CG} \cdot \sin(\beta + \psi) + \dot{y}_{CG} \cdot \cos(\beta + \psi) = 0 \quad (3.14)$$

$$\dot{x}_{wi} \cdot \sin(\beta_{wi} + \delta_{wi} + \psi) + \dot{y}_{wi} \cdot \cos(\beta_{wi} + \delta_{wi} + \psi) = 0 \quad (3.15)$$

The geometric constraints between each wheel and the center of gravity of the vehicle are written as:

$$\begin{aligned} x_{w1} &= x_{CG} + l_f \cdot \cos\psi - d/2 \cdot \sin\psi \\ x_{w2} &= x_{CG} - l_f \cdot \cos\psi - d/2 \cdot \sin\psi \\ x_{w3} &= x_{CG} - l_r \cdot \cos\psi + d/2 \cdot \sin\psi \\ x_{w4} &= x_{CG} + l_r \cdot \cos\psi + d/2 \cdot \sin\psi \end{aligned} \quad (3.16)$$

$$\begin{aligned}
 y_{w1} &= y_{CG} + l_f \cdot \sin\psi + d/2 \cdot \cos\psi \\
 y_{w2} &= y_{CG} - l_f \cdot \sin\psi + d/2 \cdot \cos\psi \\
 y_{w3} &= y_{CG} - l_r \cdot \sin\psi - d/2 \cdot \cos\psi \\
 y_{w4} &= y_{CG} + l_r \cdot \sin\psi - d/2 \cdot \cos\psi
 \end{aligned} \tag{3.17}$$

Substituting equations (3.16) and (3.17) by equation (3.15), the following matrix form equation is obtained:

$$A_0 \cdot \dot{q}_0 = 0 \tag{3.18}$$

where

$$A_0 = \begin{bmatrix} \sin\phi_{w1} & -\cos\phi_{w1} & -l_f \cdot \cos(\phi_{w1} - \psi) - d/2 \cdot \sin(\phi_{w1} - \psi) \\ \sin\phi_{w2} & -\cos\phi_{w2} & l_r \cdot \cos(\phi_{w2} - \psi) + d/2 \cdot \sin(\phi_{w2} + \psi) \\ \sin\phi_{w3} & -\cos\phi_{w3} & l_r \cdot \cos(\phi_{w3} - \psi) - d/2 \cdot \sin(\phi_{w3} + \psi) \\ \sin\phi_{w4} & -\cos\phi_{w4} & -l_f \cdot \cos(\phi_{w4} - \psi) + d/2 \cdot \sin(\phi_{w4} - \psi) \\ \sin\phi_0 & -\cos\phi_0 & 0 \end{bmatrix} \tag{3.19}$$

$$\dot{q}_0 = \begin{bmatrix} \dot{x}_{CG} \\ \dot{y}_{CG} \\ \dot{\psi} \end{bmatrix} = 0$$

where $\phi_0 = \beta + \psi$, $\phi_{wi} = \beta_{wi} + \delta_{wi} + \psi$, $i = 1, 2, 3, 4$.

Here, it is complicated to derive a null-space vector of the constraints matrix A_0 if obtaining the vector \dot{q}_0 which satisfies equation (3.18). Therefore, a simplified constrains matrix A_{12} for bicycle model (Figure 3.9B) is represented instead of A_0 .

For instance, in terms of a bicycle model ($i = 1, 2$):

$$A_{12} \cdot \dot{q}_0 = 0 \tag{3.20}$$

where

$$A_{12} = \begin{bmatrix} \sin\phi_{w1} & -\cos\phi_{w1} & -l_f \cdot \cos(\phi_{w1} - \psi) - d/2 \cdot \sin(\phi_{w1} - \psi) \\ \sin\phi_{w2} & -\cos\phi_{w2} & l_r \cdot \cos(\phi_{w2} - \psi) + d/2 \cdot \sin(\phi_{w2} + \psi) \\ \sin\phi_0 & -\cos\phi_0 & 0 \end{bmatrix} \tag{3.21}$$

$$\dot{q}_0 = \begin{bmatrix} \dot{x}_{CG} \\ \dot{y}_{CG} \\ \dot{\psi} \end{bmatrix} = 0$$

Under the basic assumptions of planar motion, rigid body and non-slippage of

tire, the four-wheel vehicle can be approximated by a *bicycle model*, as shown in Figure 3.9. To describe the vehicle motion, a global coordinate $x - y$ is fixed on the horizontal plane on which the vehicle moves. The motion status of the vehicle can be described using the bicycle model as illustrated in Figure 3.9B.

$$\begin{bmatrix} \sin(\delta_f + \psi) & -\cos(\delta_f + \psi) & -l_f \cdot \cos\delta_f \\ \sin(\delta_r + \psi) & -\cos(\delta_r + \psi) & l_r \cdot \cos\delta_r \\ \sin(\beta + \psi) & -\cos(\beta + \psi) & 0 \end{bmatrix} \cdot \begin{bmatrix} \dot{x}_{CG} \\ \dot{y}_{CG} \\ \dot{\psi} \end{bmatrix} = 0 \quad (3.22)$$

Using a null-space vector of A_{12} , it is possible to obtain the vector \dot{q}_0 satisfying equation (3.22):

$$\begin{bmatrix} \dot{x}_{CG} \\ \dot{y}_{CG} \\ \dot{\psi} \end{bmatrix} = \begin{bmatrix} \cos(\beta + \psi) \\ \sin(\beta + \psi) \\ \frac{\cos\beta \cdot (\tan\delta_f - \tan\delta_r)}{l_f + l_r} \end{bmatrix} \cdot v \quad (3.23)$$

where $\beta = \arctan \frac{l_f \cdot \tan\delta_r + l_r \cdot \tan\delta_f}{l_f + l_r}$ and v is linear velocity of the vehicle.

3.3.1 Dynamics of the Nonlinear Single-Track Model

In this section, the equations of motion of the nonlinear single-track model are deduced, which relate the motion function of the forces F_x , F_y and momentum M_z exerted on the center of gravity (CG) of the chassis.

If a vehicle follows a circular trajectory, it experiences a centrifugal force F_c pointing to the exterior of the curve and a force of inertia F_i to the opposite direction of the velocity v , see Fig 3.10. These two forces are opposed by the forces F_x and F_y (pointing parallel to the x and the y axis, respectively) and the moment M_z .

The parameters of the car model are given in Table 3.1.

Setting up the equilibrium of forces and momentum yields

$$\begin{aligned} F_x &= -F_c \cdot \sin\beta + F_i \cdot \cos\beta \\ F_y &= F_c \cdot \cos\beta + F_i \cdot \sin\beta \\ M_z &= J_z \cdot \ddot{\psi} \end{aligned} \quad (3.24)$$

The centrifugal force is $F_c = \frac{m \cdot v^2}{R}$, with the curve radius R , i.e. the distance between center of gravity CG and the center point of rotation COR . Differentiating with respect to time the relation for the length of a segment of a circle $s = R \cdot (\beta + \psi)$

Table 3.1: Parameters of the car model

Parameter	Remarks
x_{CG}, y_{CG}	Axis for the center of gravity co-ordinate system
x_w, y_w	Axis for the wheel co-ordinate system
F_{Lf}, F_{Lr}	Longitudinal forces of front and rear tires, respectively
F_{Sf}, F_{Sr}	Lateral forces of front and rear tires, respectively
F_x, F_y, M_z	Forces and momentum on the center of gravity (CG) of the chassis
F_c	Centrifugal force of the vehicle
F_i	Vehicle inertial force
F_{ad}	Aerodynamic drag force
C_{ad}	Aerodynamic drag coefficient
A_{ad}	Maximum vehicle cross-sectional area
ρ_{ad}	Air density
v	Longitudinal speed at the CG of the vehicle
m	Mass of the vehicle
J_z	Inertia moment around center of gravity (CG)
l_f, l_r	Distance from front and rear tires to CG , respectively
α_f, α_r	Slip angle of front and rear tires, respectively
δ_f, δ_r	Wheel steering angle of front and rear tires, respectively
β	Vehicle body sideslip angle (angle between x_{CG} and v , the vehicle velocity)
β_f, β_r	Sideslip angle of front and rear chassis
ψ	Yaw angle
r	Yaw rate
c_f, c_r	Tire stiffness in the direction of y_w and x_w
μ	Road friction coefficient
R	Curve radius - distance between center of gravity CG and the center point of rotation COR

yields $v = R \cdot (\dot{\beta} + \dot{\psi})$; $(\beta + \psi)$ is the angle between the velocity v and the space-fixed coordinate system (x_0, y_0) . With this the centrifugal force depending on the state variables is obtained as

$$F_c = m \cdot v \cdot (\dot{\beta} + \dot{\psi}) \quad (3.25)$$

In (3.24), F_i is the vehicle inertial force

$$F_i = m \cdot \dot{v} \quad (3.26)$$

Inserting (3.25) and (3.26) in (3.24) yields the equations of motion depending on

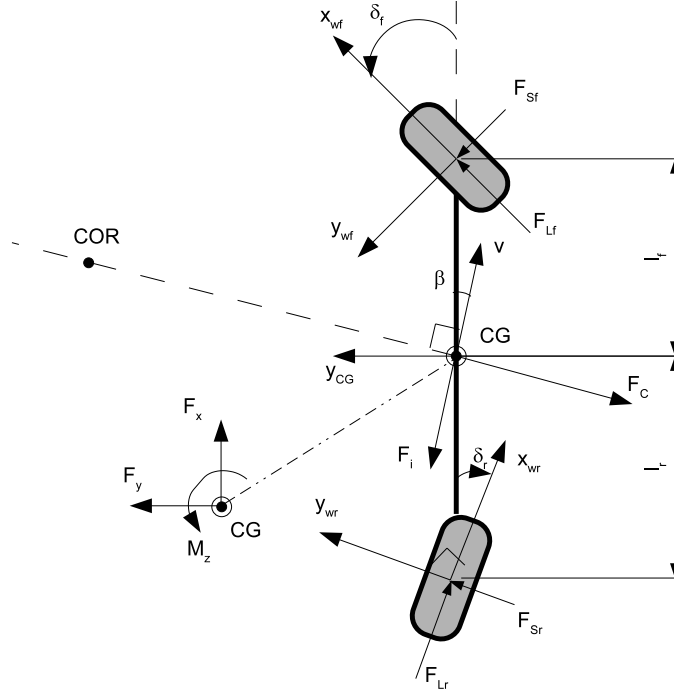


Figure 3.10: The one-track bicycle model.

the state variable $x = [\beta \cdot v \cdot \dot{\psi}]^T$ of the nonlinear one-track model:

$$\begin{aligned}
 F_x &= -m \cdot v \cdot (\dot{\beta} + \dot{\psi}) \cdot \sin\beta + m \cdot \dot{v} \cdot \cos\beta \\
 F_y &= m \cdot v \cdot (\dot{\beta} + \dot{\psi}) \cdot \cos\beta + m \cdot \dot{v} \cdot \sin\beta \\
 M_z &= J_z \cdot \ddot{\psi}
 \end{aligned} \tag{3.27}$$

where J_z represents the total yaw moment of inertia. Yaw rate $r = \dot{\psi}$ will be introduced as a state variable. From (3.27), the following is obtained:

$$\begin{bmatrix} m \cdot v \cdot (\dot{\beta} + r) \\ m \cdot \dot{v} \\ J_z \cdot \dot{r} \end{bmatrix} = \begin{bmatrix} -\sin\beta & \cos\beta & 0 \\ \cos\beta & \sin\beta & 0 \\ 0 & 0 & 1 \end{bmatrix} \cdot \begin{bmatrix} F_x \\ F_y \\ M_z \end{bmatrix} \tag{3.28}$$

A relation between the tire forces F_S , F_L and the forces/moment on the center of gravity F_x , F_y , M_z is needed. Fig. 3.10 shows that there exists the purely geometric

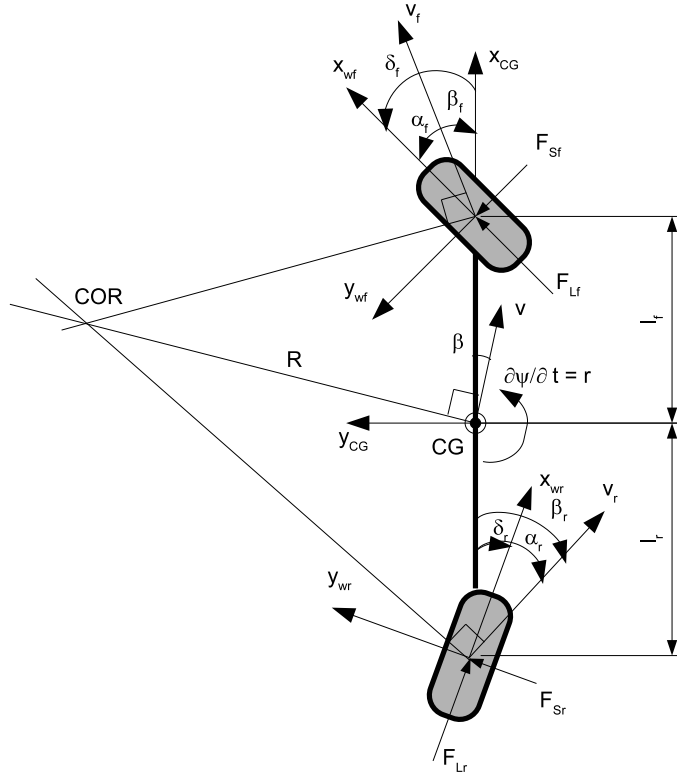


Figure 3.11: The one-track bicycle model.

relations:

$$\begin{aligned}
 \begin{bmatrix} F_x \\ F_y \\ M_z \end{bmatrix} &= \begin{bmatrix} -\sin\delta_f & -\sin\delta_r \\ \cos\delta_f & \cos\delta_r \\ l_f \cdot \cos\delta_f & -l_r \cdot \cos\delta_r \end{bmatrix} \cdot \begin{bmatrix} F_{Sf} \\ F_{Sr} \end{bmatrix} + \\
 &+ \begin{bmatrix} \cos\delta_f & \cos\delta_r \\ \sin\delta_f & \sin\delta_r \\ l_f \cdot \sin\delta_f & -l_r \cdot \sin\delta_r \end{bmatrix} \cdot \begin{bmatrix} F_{Lf} \\ F_{Lr} \end{bmatrix} + \begin{bmatrix} -1 \\ 0 \\ 0 \end{bmatrix} \cdot F_{ad}
 \end{aligned} \tag{3.29}$$

The aerodynamic drag resistance force F_{ad} given by $F_{ad} = 1/2 \cdot \rho_{ad} \cdot C_{ad} \cdot A_{ad} \cdot v^2$ affects vehicle longitudinal dynamics as the cruise speed increases. Different values of the drag coefficient C_{ad} are available in the literature for different vehicles, C_{ad} usually ranges between 0.3 and 0.4 for automobiles.

When a vehicle is cornering, the car motion does not follow the directed angle δ (steering angle). There is always a certain slip so that the car follows a smaller angle, the so-called slip angle β of the vehicle. The difference between the steering angle

and the slip angle of the vehicle is the slip angle α of the tire (see Fig. 3.11):

$$\begin{aligned}\alpha_f &= \delta_f - \beta_f \\ \alpha_r &= \delta_r - \beta_r\end{aligned}\tag{3.30}$$

The front and rear chassis sideslip angles β_f and β_r are calculated by a “kinematic model” from the state variables β , r and v

$$\begin{aligned}v_f \cdot \sin\beta_f &= v \cdot \sin\beta + l_f \cdot r \\ v_r \cdot \sin\beta_r &= v \cdot \sin\beta - l_r \cdot r\end{aligned}\tag{3.31}$$

The longitudinal components of these vectors must be equal, as they are connected through the rigid chassis of the vehicle:

$$v_f \cdot \cos\beta_f = v_r \cdot \cos\beta_r = v \cdot \cos\beta\tag{3.32}$$

Eliminating v_f and v_r from (3.32) by using (3.31) leads to

$$\begin{aligned}\tan\beta_f &= \tan\beta + \frac{l_f \cdot r}{v \cdot \cos\beta} \\ \tan\beta_r &= \tan\beta - \frac{l_r \cdot r}{v \cdot \cos\beta}\end{aligned}\tag{3.33}$$

The relationship between the tire sideslip angles and the tire side forces are given by a nonlinear tire model

$$\begin{aligned}F_{sf} &= F_{sf}(\alpha_f) \\ F_{sr} &= F_{sr}(\alpha_r)\end{aligned}\tag{3.34}$$

A nonlinear tire model can be found in [70].

3.3.2 Linearized Single-Track Model

In the following a short overview of the assumptions has been made to obtain the linear model:

- vehicle sideslip angle β is small (β is limited to a value which is less than 10°) and the vehicle travels at constant speed, i.e. $\sin\beta \approx \beta$, $\cos\beta \approx 1$ and $\dot{v} = 0$ ($\Rightarrow F_x = 0$, $\Rightarrow F_l$ is constantly zero). Then (3.28) becomes

$$\begin{bmatrix} m \cdot v \cdot (\dot{\beta} + r) \\ J_z \cdot \dot{r} \end{bmatrix} = \begin{bmatrix} F_y \\ M_z \end{bmatrix}\tag{3.35}$$

- the steering angles δ_f and δ_r are small, i.e. $\sin\delta \approx \delta$ and $\cos\delta \approx 1$. Then (3.29) becomes

$$\begin{bmatrix} F_y \\ M_z \end{bmatrix} = \begin{bmatrix} 1 & 1 \\ l_f & -l_r \end{bmatrix} \cdot \begin{bmatrix} F_{sf}(\alpha_f) \\ F_{sr}(\alpha_r) \end{bmatrix} \quad (3.36)$$

- the front and rear chassis sideslip angles β_f and β_r are small. Then, from (3.33)

$$\begin{aligned} \beta_f &= \beta + \frac{l_f \cdot r}{v} \\ \beta_r &= \beta - \frac{l_r \cdot r}{v} \end{aligned} \quad (3.37)$$

- the nonlinear tire characteristics can be approximated by

$$\begin{aligned} F_{sf}(\alpha_f) &= c_f^* \cdot \alpha_f = c_f \cdot \mu \cdot \alpha_f \\ F_{sr}(\alpha_r) &= c_r^* \cdot \alpha_r = c_r \cdot \mu \cdot \alpha_r \end{aligned} \quad (3.38)$$

where c_f^* and c_r^* are referred to as ‘‘cornering stiffnesses’’ in the automotive literature.

From these assumptions, the linearized model has the following form:

$$\begin{bmatrix} m \cdot v \cdot (\dot{\beta} + r) \\ J_z \cdot \dot{r} \end{bmatrix} = \begin{bmatrix} 1 & 1 \\ l_f & -l_r \end{bmatrix} \cdot \begin{bmatrix} c_f \cdot \mu \cdot \left(\delta_f - \beta - \frac{l_f \cdot r}{v} \right) \\ c_r \cdot \mu \cdot \left(\delta_r - \beta + \frac{l_r \cdot r}{v} \right) \end{bmatrix} \quad (3.39)$$

Rearranging terms, the following linear state-space representation is obtained:

$$\begin{bmatrix} \dot{\beta} \\ \dot{r} \end{bmatrix} = \begin{bmatrix} a_{11} & a_{12} \\ a_{21} & a_{22} \end{bmatrix} \cdot \begin{bmatrix} \beta \\ r \end{bmatrix} + \begin{bmatrix} b_{11} & b_{12} \\ b_{21} & b_{22} \end{bmatrix} \cdot \begin{bmatrix} \delta_f \\ \delta_r \end{bmatrix} \quad (3.40)$$

with

$$\begin{aligned} a_{11} &= -\frac{\mu \cdot (c_r + c_f)}{m \cdot v} \\ a_{12} &= \frac{\mu \cdot (c_r \cdot l_r - c_f \cdot l_f)}{m \cdot v^2} - 1 \\ a_{21} &= \frac{\mu \cdot (c_r \cdot l_r - c_f \cdot l_f)}{J_z} \\ a_{22} &= -\frac{\mu \cdot (c_r \cdot l_r^2 + c_f \cdot l_f^2)}{J_z \cdot v} \end{aligned} \quad (3.41)$$

$$\begin{aligned} b_{11} &= \frac{\mu \cdot c_f}{m \cdot v} \\ b_{21} &= \frac{\mu \cdot c_r}{m \cdot v} \\ b_{21} &= \frac{\mu \cdot c_f \cdot l_f}{J_z} \\ b_{21} &= -\frac{\mu \cdot c_r \cdot l_r}{J_z} \end{aligned} \quad (3.42)$$

Table 3.2: Vehicle model summary

Model name	Model for vehicle position	Model for vehicle yaw
Single-track kinematic	$\dot{x}_{CG} = v \cdot \cos(\psi)$ $\dot{y}_{CG} = v \cdot \sin(\psi)$	$\dot{\psi} = \frac{v \cdot \tan(\delta_f)}{l_f + l_r}$
Double-track kinematic	$\dot{x}_{CG} = v \cdot \cos(\psi)$ $\dot{y}_{CG} = v \cdot \sin(\psi)$	$\dot{\psi} = \frac{2 \cdot v \cdot \tan(\delta_f)}{2 \cdot (l_f + l_r) + d \cdot \tan \delta_f }$
Single-track dynamic	$\dot{x}_{CG} = v \cdot \cos(\beta + \psi)$ $\dot{y}_{CG} = v \cdot \sin(\beta + \psi)$	$\begin{bmatrix} \dot{\beta} \\ \dot{\psi} \end{bmatrix} = \begin{bmatrix} a_{11} & a_{12} \\ a_{21} & a_{22} \end{bmatrix} \begin{bmatrix} \beta \\ \psi \end{bmatrix} + \begin{bmatrix} b_{11} \\ b_{21} \end{bmatrix} \delta_f$

Table 3.2 summarizes the vehicle models presented in this chapter. Here it is illustrated how the steady-state models may be used to help simulate vehicle performance by providing an estimate of vehicle yaw rate.

3.4 Motion Control for Car-like Vehicle

3.4.1 Longitudinal Control

Longitudinal control involves the vehicle's throttle and brake. The basic functions of automated longitudinal vehicle control are keeping the vehicle a safe distance behind another vehicle, maintaining relatively constant speed with the least brake use and applying the brake as fast as possible in emergency situations.

The cruise control option on vehicles only controls the throttle and allows a vehicle to maintain a relatively constant velocity without the driver needing to push the accelerator. *Intelligent* or *adaptive* cruise controllers with the use of sensing devices such as radar, laser, vision could be able to determine and maintain safe headway among vehicles at given velocities and vehicle conditions (brake, throttle, vehicle wind drag, tire traction, weight, weight distribution) while maximizing road capacity. These controllers need to determine when to choose the throttle or brake and minimize the switching between the two for a smooth and fuel efficient ride.

A platoon is a group of two or more closely spaced vehicles traveling with the same velocity in the same lane. There are two main approaches: a) *autonomous intelligent cruise control* which does not involve communications of the vehicle with exterior sources. The driver needs to set the desired speed and headway; b) *cooperative*

intelligent cruise control allows the vehicle to communicate with the other vehicles in its platoon.

3.4.2 Lateral Control

Lateral vehicle control ([71], [72], [73]) involves the steering of the vehicle. It is concerned with lane keeping, turning, lane changing and avoiding objects that might appear in front of the vehicle. There are two main approaches for automated steering: a) *look-down* systems and b) *look-ahead* systems.

Look-down systems ([74], [75], [76]) follow wires or magnets embedded in the middle of the lane. The major advantage of using a look-down system is that it is unaffected by blinding conditions such as heavy precipitation, snow, fog or dust.

Look-ahead systems ([77], [78]) use cameras for lane following, radar for following the preceding vehicle and lasers and/or cameras for lane switching.

3.4.3 Integration of Lateral and Longitudinal Controls

Lateral and longitudinal controllers ([79], [80]) need to be combined to determine the brake pressure to keep the vehicle in its lane at the proper turning angle and losing the least amount of speed. Another problem is obstacle avoidance when the controller needs to determine if the vehicle should stop, go over or avoid an object in front of it. If the vehicle avoids an obstacle, the controller need to determine the correct brake pressure and turning movement to prevent the vehicle's tires from losing contact with the road.

Chapter 4

Path Planning

4.1 Introduction

Mobile robot research has made considerable advances in the past three decades. Earlier works on mobile robots concentrated on path planning, where the objective was to plan a collision free path and avoid stationary obstacles, while working in an indoor/outdoor environment. Stationary obstacles are defined as fixed or non moving obstructions such as walls or furniture. The most popular method in early path planning was the configuration space method, where the mobile robot is shrunk to a point, while corresponding growing the obstacles in order to compensate for taking the robot as a point [98].

The many methods of path planning can be divided into three main categories: roadmap approach [99], cell decomposition [100], and potential field [101] methods. The roadmap approach is where the obstacle free area is modelled as a network of lines. This network is then searched for a path that connects the start and goal points. Cell decomposition is where the obstacle free area is subdivided into cells that are interconnected to each other. These cells are then searched to find a path that connects the start and goal points. Potential field methods use imaginary forces acting on a robot. The goal position attracts the robot by pulling it towards the goal, whereas the obstacles repulse the robot by pushing it away.

A *trajectory* is a path which is an explicit function of time. To have smooth movement, the trajectory must be twice differentiable to give a continuous velocity and acceleration. As a result, curve fitting is an integral part of trajectory planning. There are a number of techniques used in curve fitting, including the use of B-splines, cubic splines [102], clothoids, etc [103]. Simple path planning techniques assume that

the robot is omnidirectional and is able to execute paths flawlessly. However, in the real world, these assumptions are often not valid. Planning a trajectory which disregards the robot constraints has a profound impact on the ability of the robot to track the path [104]. Earlier works in trajectory planning added simplified kinematic constraints to plan a feasible trajectory. Louste et al. [101] used the minimum turning radius and the dimensions of a robot to plan a trajectory. The path was divided into straight and curved segments and the velocity was individually planned for each segment. As a result the path had a smooth trajectory with a continuous first derivative. Other works [105] added dynamic constraints such as upper velocity and acceleration bounds in order to make dynamical effects negligible. This was done by setting the upper velocity and acceleration to very low values as compared to the characteristics of the robot. Munoz et al. [104] proposed a method to create a smooth trajectory subject to kinematic and dynamic constraints. The trajectory planner created the shortest obstacle free trajectory, which was smoothed out by using B-spline curves. Constraints such as velocity and acceleration limits based on the limits of the servomotors, maximum curvature, wheel ground adhesion, and a maximum lateral acceleration were added. Cherif [106] went a step further and made a detailed model of both the terrain and the robot, and used a multilevel motion planner for an outdoor setting. The algorithm consisted of a high level motion planner which minimized the distance between the present robot location and the desired end location. A local level motion planner attempted to attain the goals set by the higher level. This was done by computing wheel accelerations, contact forces, equations of motion and the new state of the deformable regions in the terrain. This algorithm also incorporated the wheel ground interaction, added a tip over constraint, and a bounded control torque constraint.

Temporal planning is to follow a given velocity profile. This may be used to minimize time of motion and to avoid moving obstacles. Fotouhi et al. [107] proposed a velocity planning algorithm for a two-link rigid manipulator. A rudimentary trajectory was created by assigning an arbitrary time to a path. Using linear time scaling, this trajectory was modified to take into account velocity and acceleration constraints of the manipulator. In order to have the manipulator end effector capable to follow any predefined velocity profile, a non-linear time scaling technique was presented. This algorithm can be implemented on a wheeled mobile robot. Munoz et al. [108] proposed a temporal planning algorithm where the maximum possible velocity was determined by using a number of constraints. This algorithm contains three main

parts. The first was the temporal planning process, where the maximum possible velocity was determined using the following constraints: velocity, acceleration, wheel slippage, moments, and a built-in safety speed. The next step was to create a smooth path using B-splines while avoiding moving obstacles. The final step was to merge the maximum velocity with the path, thereby creating a trajectory. While most other works use constant upper velocity, acceleration, and deceleration bounds, Prado et al. [109] created upper bound velocity, acceleration and deceleration functions which changed with the path. In a more recent work, Prado et al. [110] introduced a velocity profiling technique that divides the path into smaller segments. The velocity profile of each segment is generated by a cubic polynomial which is then integrated to obtain position and differentiated to obtain the acceleration. The profile is checked with a number of constraints and is iteratively modified until the constraints are fully satisfied. He also provided a method to avoid moving obstacles by modifying the velocity profile of the mobile robot. If a moving obstacle was encountered, the robot speed was reduced until the obstacle had cleared the path.

4.2 Quintic Equations

Let $P(u) = \{p_1(u), p_2(u), \dots, p_n(u)\}$, $u \in [0, 1]$ be a route defined by a set of points computed by a path planner as shown in Figure 4.1. Each point p_i is composed of three basic elements: x_i , y_i and ϕ_i where $i = 1, 2, \dots, n$. The first two components, define position relative to a global reference frame shown in Figure 4.1. The last component, ϕ_i , is the heading (orientation) from one point to the next defined in the $X - Y$ plane. There are several methods to join these points with a curve. The easiest method is to connect the points with straight lines; however, there are sudden changes in slope which in mobile robotics means a discontinuous velocity. Another method could be to use a high order polynomial. However, if there are numerous points, the path may become wavy due to the oscillatory nature of high order polynomials. A more effective method is the use of piecewise quintic polynomials, also known as quintic splines. These quintic splines are ideal since they provide a continuity in position, heading, curvature, velocity, and acceleration [111], [112].

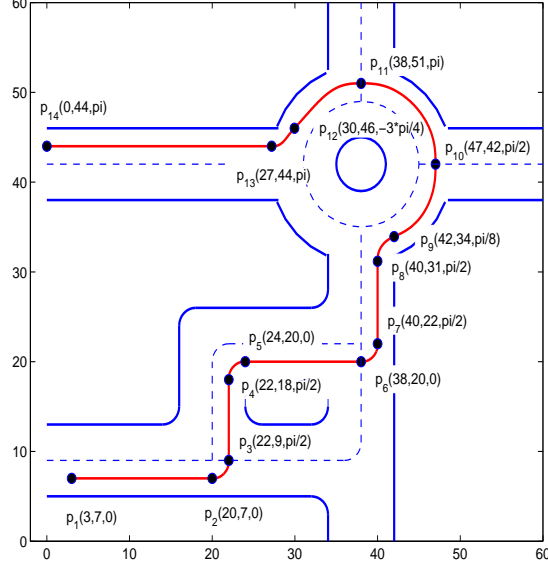


Figure 4.1: Path planning example using quintic polynomial curves.

Closed-form expressions of the quintic G^2 -splines can be presented as follows

$$p_{i,i+1}(u) = \begin{bmatrix} x_{i,i+1}(u) \\ y_{i,i+1}(u) \\ \phi_{i,i+1}(u) \end{bmatrix} = \begin{bmatrix} \alpha_{i0} + \alpha_{i1}u + \alpha_{i2}u^2 + \alpha_{i3}u^3 + \alpha_{i4}u^4 + \alpha_{i5}u^5 \\ \beta_{i0} + \beta_{i1}u + \beta_{i2}u^2 + \beta_{i3}u^3 + \beta_{i4}u^4 + \beta_{i5}u^5 \\ \phi_i(u) \end{bmatrix} \quad (4.1)$$

where

$$\begin{aligned} \alpha_{i0} &= x_i(0) \\ \alpha_{i1} &= \eta_1 \cdot \cos(\phi_i(0)) \\ \alpha_{i2} &= \frac{1}{2}(\eta_3 \cdot \cos(\phi_i(0)) - \eta_1^2 \cdot k_i \cdot \sin(\phi_i(0))) \\ \alpha_{i3} &= 10 \cdot (x_{i+1}(0) - x_i(0)) - \left(6 \cdot \eta_1 + \frac{3}{2} \cdot \eta_3\right) \cdot \cos(\phi_i(0)) - \\ &\quad - \left(4 \cdot \eta_2 - \frac{1}{2} \cdot \eta_4\right) \cdot \cos(\phi_{i+1}(0)) + \frac{3}{2} \cdot \eta_1^2 \cdot k_i \cdot \sin(\phi_i(0)) - \frac{1}{2} \cdot \eta_2^2 \cdot k_{i+1} \cdot \sin(\phi_{i+1}(0)) \\ \alpha_{i4} &= -15 \cdot (x_{i+1}(0) - x_i(0)) + \left(8 \cdot \eta_1 + \frac{3}{2} \cdot \eta_3\right) \cdot \cos(\phi_i(0)) + \\ &\quad + (7 \cdot \eta_2 - \eta_4) \cdot \cos(\phi_{i+1}(0)) - \frac{3}{2} \cdot \eta_1^2 \cdot k_i \cdot \sin(\phi_i(0)) + \eta_2^2 \cdot k_{i+1} \cdot \sin(\phi_{i+1}(0)) \\ \alpha_{i5} &= 6 \cdot (x_{i+1}(0) - x_i(0)) - \left(3 \cdot \eta_1 + \frac{1}{2} \cdot \eta_3\right) \cdot \cos(\phi_i(0)) - \\ &\quad - \left(3 \cdot \eta_2 - \frac{1}{2} \eta_4\right) \cdot \cos(\phi_{i+1}(0)) + \frac{1}{2} \cdot \eta_1^2 \cdot k_i \cdot \sin(\phi_i(0)) - \frac{1}{2} \eta_2^2 \cdot k_{i+1} \cdot \sin(\phi_{i+1}(0)) \end{aligned}$$

$$\begin{aligned}
\beta_{i0} &= y_i(0) \\
\beta_{i1} &= \eta_1 \cdot \cos(\phi_i(0)) \\
\beta_{i2} &= \frac{1}{2} (\eta_3 \cdot \cos(\phi_i(0)) + \eta_1^2 \cdot k_i \cdot \sin(\phi_i(0))) \\
\beta_{i3} &= 10 \cdot (y_{i+1}(0) - y_i(0)) - \left(6 \cdot \eta_1 + \frac{3}{2} \cdot \eta_3\right) \cdot \sin(\phi_i(0)) - \\
&\quad - \left(4 \cdot \eta_2 - \frac{1}{2} \cdot \eta_4\right) \cdot \sin(\phi_{i+1}(0)) - \frac{3}{2} \cdot \eta_1^2 \cdot k_i \cdot \cos(\phi_i(0)) + \frac{1}{2} \cdot \eta_2^2 \cdot k_{i+1} \cdot \cos(\phi_{i+1}(0)) \\
\beta_{i4} &= -15 \cdot (y_{i+1}(0) - y_i(0)) + \left(8 \cdot \eta_1 + \frac{3}{2} \cdot \eta_3\right) \cdot \sin(\phi_i(0)) + \\
&\quad + \left(7 \cdot \eta_2 - \eta_4\right) \cdot \sin(\phi_{i+1}(0)) + \frac{3}{2} \cdot \eta_1^2 \cdot k_i \cdot \cos(\phi_i(0)) - \eta_2^2 \cdot k_{i+1} \cdot \cos(\phi_{i+1}(0)) \\
\beta_{i5} &= 6 \cdot (y_{i+1}(0) - y_i(0)) - \left(3 \cdot \eta_1 + \frac{1}{2} \cdot \eta_3\right) \cdot \sin(\phi_i(0)) - \\
&\quad - \left(3 \cdot \eta_2 - \frac{1}{2} \eta_4\right) \cdot \sin(\phi_{i+1}(0)) - \frac{1}{2} \cdot \eta_1^2 \cdot k_i \cdot \cos(\phi_i(0)) + \frac{1}{2} \eta_2^2 \cdot k_{i+1} \cdot \cos(\phi_{i+1}(0))
\end{aligned}$$

Where k_i and k_{i+1} are scalar curvatures, $k_i \in \mathfrak{R}$, $i = 1, 2, \dots, n$ and can be arbitrary assigned (in this case $k_i = 0$). The real parameters η_m , $m = 1, 2, 3, 4$, appearing in above expressions can be packed together to form the four-dimensional vector $\eta := [\eta_1, \eta_2, \eta_3, \eta_4]^T \in H := \mathfrak{R}^+ \times \mathfrak{R}^+ \times \mathfrak{R} \times \mathfrak{R}$. η_1 mainly influences the shape of the curve at the beginning, η_2 affects its closing. In practice, to attain symmetric curves we have imposed $\eta_1 = \eta_2$. In Figure 4.2, η_1 and η_2 are varied whereas η_3 and η_4 are constant ($\eta_3 = \eta_4 = 0$). Parameters η_3 and η_4 modulate the curvature variation at the beginning and at the closing of the spline respectively. In Figure 4.3, η_1 and η_2 are kept constant and curves are traced for different values of η_3 and η_4 . Very negative values of η_3 (very positive value for η_4) cause strong curvature variations.

According to the theory of planar curves, an explicit expression of curvature, $k_{i,i+1}(u)$ is

$$k_{i,i+1}(u) = \frac{\dot{x}_{i,i+1}(u) \cdot \ddot{y}_{i,i+1}(u) - \ddot{x}_{i,i+1}(u) \cdot \dot{y}_{i,i+1}(u)}{\left(\dot{x}_{i,i+1}^2(u) + \dot{y}_{i,i+1}^2(u)\right)^{3/2}} \quad (4.2)$$

The function $k_{i,i+1}(u)$ is continuous over $[0, 1]$ because $p_{i,i+1}(u)$ is a G^2 -curve.

The *curve length* measured along two points p_i, p_{i+1} is denoted by $s_{i,i+1}(u)$; it can be expressed as

$$s_{i,i+1}(u) = \int_{u_0}^u \sqrt{\dot{x}_{i,i+1}^2(u) + \dot{y}_{i,i+1}^2(u)} \cdot du \quad (4.3)$$

and we denote by $s_{i,i+1}^{-1} : [0, s_{i,i+1}(u_1)] \rightarrow [u_0, u_1]$ its inverse function that is evidently a continuous function.

4.3 Velocity Planning

The aim of this section is to obtain a longitudinal and angular velocity profiles ($v(t)$ and $\omega(t)$). The profile must be compatible with the assigned total path length s_k and

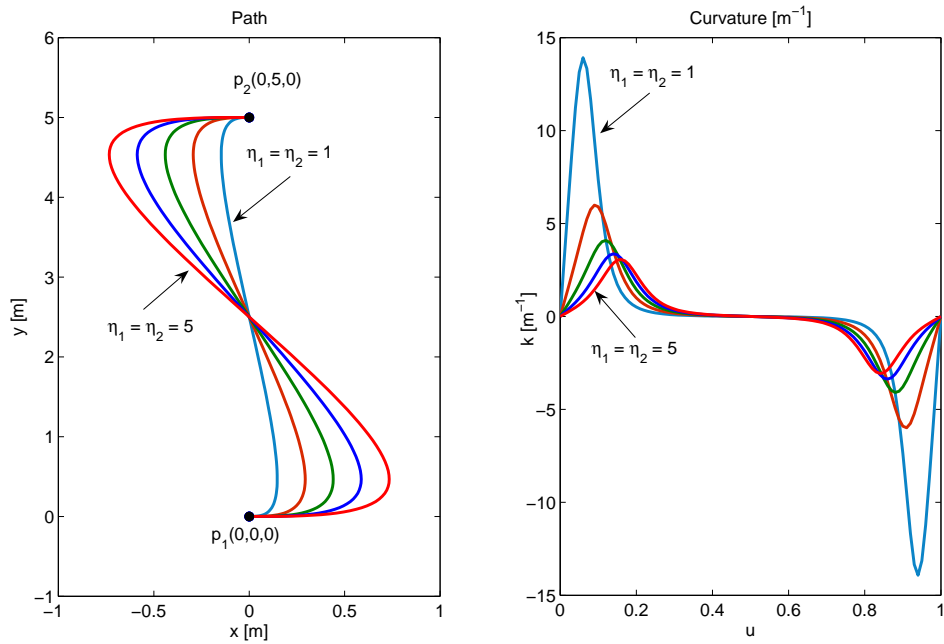


Figure 4.2: Lane change ($\eta_1 = \eta_2 = 1, 2, 3, 4, 5, \eta_3 = \eta_4 = 0$).

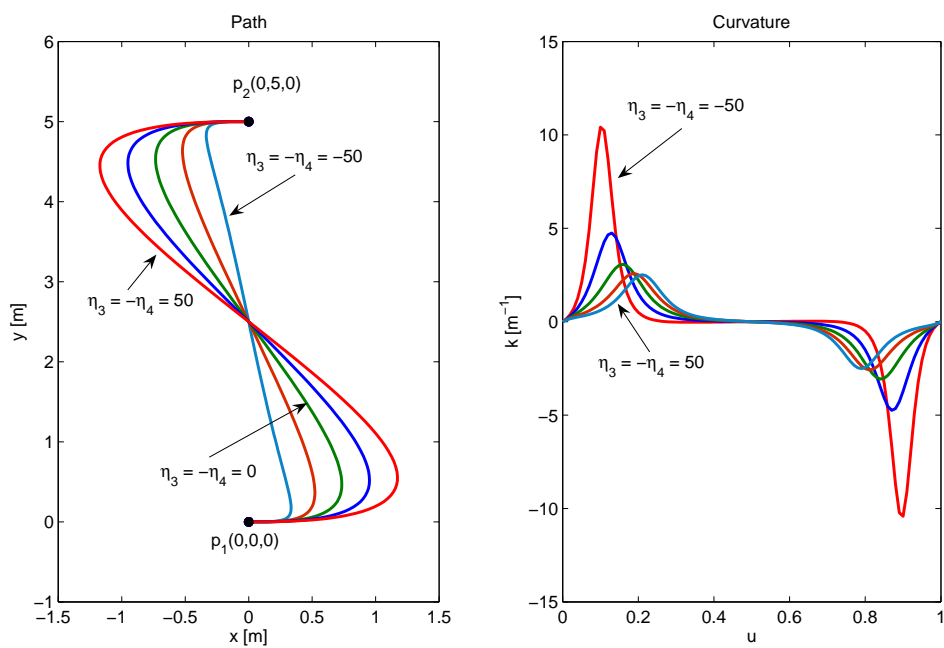


Figure 4.3: Lane change ($\eta_1 = \eta_2 = 5, \eta_3 = \eta_4 = -50, -25, 0, 25, 50$).

it must comply with human comfort travel (see Section 5 - *Human Body Comfort*). It is necessary to generate a velocity profile $v_{i,i+1}(t) \in C^1([0, t_m])$ such that

$$s_m = \int_0^{t_m} v_{i,i+1}(\tau) \cdot d\tau \quad (4.4)$$

and

$$v_{i,i+1}(t) > 0, \quad \forall t \in (0, t_m) \quad (4.5)$$

where t_k is the travelling time between two consecutive points (p_i and p_{i+1}) and it is given function by the comfort of human body (see Section 5). The generated velocity profile has to satisfy the following boundary conditions:

$$v_{i,i+1}(0) = v_i \geq 0, \quad v_{i,i+1}(t_m) = v_{i+1} \geq 0, \quad \dot{v}_{i,i+1}(0) = a_i, \quad \dot{v}_{i,i+1}(t_m) = a_{i+1} \quad (4.6)$$

The function $v_{i,i+1}(t)$ is made of five properly joined spline curves, see Figure 4.4. The travelling time between two consecutive points (p_i and p_{i+1}) is divided into five intervals:

$$\sum_{j=1}^5 t_{mj} = t_m \quad (4.7)$$

The velocity profiles corresponding to the five time intervals as $v_{(i,i+1)j}(t)$ with $t \in [0, t_{mj}]$, $j = 1, 2, \dots, 5$ are given by:

$$v_{(i,i+1)j}(t) = \gamma_{1j} + 2 \cdot \gamma_{2j} \cdot t + 3 \cdot \gamma_{3j} \cdot t^2 \quad (4.8)$$

Similarly, position and acceleration functions are indicated as $s_{(i,i+1)j}(t)$ and $a_{(i,i+1)j}(t)$ respectively:

$$s_{(i,i+1)j}(t) = \gamma_{1j} \cdot t + \gamma_{2j} \cdot t^2 + \gamma_{3j} \cdot t^3 \quad (4.9)$$

$$a_{(i,i+1)j}(t) = 2 \cdot \gamma_{2j} + 6 \cdot \gamma_{3j} \cdot t \quad (4.10)$$

where the coefficients γ are evaluated imposing the following conditions:

$$\begin{aligned} v_{(i,i+1)1}(t_{m1}) &= v_{(i,i+1)2}(0), & v_{(i,i+1)2}(t_{m2}) &= v_{(i,i+1)3}(0), \\ v_{(i,i+1)3}(t_{m3}) &= v_{(i,i+1)4}(0), & v_{(i,i+1)4}(t_{m4}) &= v_{(i,i+1)5}(0), \\ a_{(i,i+1)1}(t_{m1}) &= a_{(i,i+1)2}(0), & a_{(i,i+1)2}(t_{m2}) &= a_{(i,i+1)3}(0), \\ a_{(i,i+1)3}(t_{m3}) &= a_{(i,i+1)4}(0), & a_{(i,i+1)4}(t_{m4}) &= a_{(i,i+1)5}(0). \end{aligned} \quad (4.11)$$

and

$$\begin{aligned} v_{(i,i+1)1}(0) &= v_i(0), & v_{(i,i+1)5}(t_{m5}) &= v_{i+1}(0), \\ a_{(i,i+1)1}(0) &= a_i(0), & a_{(i,i+1)5}(t_{m5}) &= a_{i+1}(0). \end{aligned} \quad (4.12)$$

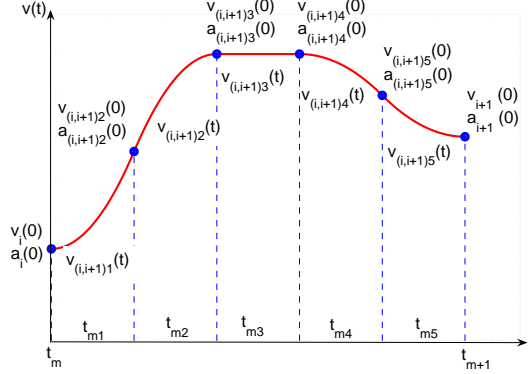


Figure 4.4: An example of a longitudinal velocity profile.

The velocity profile is completely defined if all the γ coefficients are known ($3 \times 5 = 15$ parameters) and all the travelling times are assigned (5 parameters). The 13 constraint equations given by (4.6), (4.11) and (4.12) reduce the number of available degrees of freedom to 7 ($15 + 5 - 13 = 7$ parameters):

$$\left[t_{m1}, t_{m2}, t_{m4}, t_{m5}, v_{(i,i+1),3}(0), v_{(i,i+1),4}(0), a_{(i,i+1),3}(0) \right].$$

Simple algebraic manipulations lead to the following expressions:

$$\begin{aligned} \gamma_{11} &= v_i(0) \\ \gamma_{21} &= \frac{a_i(0)}{2} \\ \gamma_{31} &= \frac{-2a_1(0)t_{m1} - (a_i(0) + a_{m3}(0))t_{m2} - 2v_i(0) + 2v_{m4}}{6t_{m1}(t_{m1} + t_{m2})} \\ \gamma_{12} &= \frac{2v_{m3}(0)t_{m1} + 2v_i(0) + (a_i(0) - a_{m3}(0))t_{m1}t_{m2}}{2(t_{m1} + t_{m2})} \\ \gamma_{22} &= \frac{-a_i(0)t_{m1} - a_{m3}(0)t_{m2} - 2v_i(0) + 2v_{m3}(0)}{2(t_{m1} + t_{m2})} \\ \gamma_{32} &= \frac{(a_i(0) + a_{m3}(0))t_{m1} + 2a_{m3}t_{m2} + 2v_i(0) - 2v_3(0)}{6t_{m2}(t_{m1} + t_{m2})} \\ \gamma_{13} &= v_{m3}(0) \\ \gamma_{23} &= \frac{a_{m3}(0)}{2} \\ \gamma_{33} &= \frac{-2a_{m3}(0)t_{m3} + 2v_{m4}(0) - 2v_{m3}}{6t_{m3}^2} \\ \gamma_{14} &= v_{m4}(0) \\ \gamma_{24} &= \frac{-a_{m3}(0)t_{m3} - 2v_{m3}(0) + 2v_{m4}(0)}{2t_{m3}} \\ \gamma_{34} &= \frac{2(v_{m3}(0) - v_{m4}(0))(t_{m5} + 2t_{m4}) + [2a_{m3}(0)t_{m4} - 2(v_{m4}(0) + v_{i+1}(0)) + (a_{m3}(0) - a_{i+1}(0))t_{m5}]t_{m3}}{6t_{m3}t_{m4}(t_{m4} + t_{m5})} \\ \gamma_{15} &= \frac{2(v_{i+1}(0)t_{m4} + v_{m4}(0)t_{m5})t_{m3} + (2v_{m4}(0) - 2v_{m3}(0) - a_{m3}(0)t_{m3} - a_{i+1}(0)t_{m3})t_{m4}t_{m5}}{2t_{m3}(t_{m4} + t_{m5})} \end{aligned} \quad (4.13)$$

$$\begin{aligned}\gamma_{25} &= \frac{2(v_{m3}(0)-v_{m4}(0))t_{m4}-(2v_{m4}(0)-2v_{i+1}(0)-a_{m3}(0)t_{m4}+a_{i+1}(0)t_{m5})t_{m3}}{2t_{m3}(t_{m4}+t_{m5})} \\ \gamma_{35} &= \frac{(2v_{m4}(0)-2v_{i+1}(0)-a_{m3}(0)t_{m4}+a_{i+1}(0)t_{m4}+2a_{i+1}(0)t_{m5})t_{m3}-2(v_{m3}(0)-v_{m4}(0))t_{m4}}{6t_{m3}t_{m5}(t_{m4}+t_{m5})}\end{aligned}\quad (4.14)$$

where $m := (i, i + 1)$

To satisfy (4.7) it is necessary to further impose $t_{m3} = t_m - (t_{m1} + t_{m2} + t_{m4} + t_{m5})$ where, necessarily, $t_{m1} + t_{m2} + t_{m4} + t_{m5} < t_m$. Velocities $v_i(0)$, $v_{(i,i+1)3}(0)$, $v_{(i,i+1)4}(0)$ and $v_{i+1}(0)$ can be freely assigned respecting constraints (4.6), and $v_{(i,i+1)2}(0)$, $v_{(i,i+1)5}(0)$ are calculated by (4.8). In the same way $a_i(0)$, $a_{(i,i+1)3}(0)$ and $a_{i+1}(0)$ are given respecting (4.6), and $a_{(i,i+1)2}(0)$, $a_{(i,i+1)4}(0)$, $a_{(i,i+1)5}(0)$ are calculated using (4.10).

If we impose the following two further constraints:

$$a_{(i,i+1)3}(0) = 0, \quad a_{(i,i+1)3}(t_{m3}) = 0 \quad (4.15)$$

the number of free parameters decreases to five: $[t_{m1}, t_{m2}, t_{m4}, t_{m5}, v_{(i,i+1)3}(0)]$ because $v_{(i,i+1)4}(0) = v_{(i,i+1)3}(0)$ and $a_{(i,i+1)3}(0) = 0$. In this case, equations (4.13) become

$$\begin{aligned}\gamma_{11} &= v_i(0) \\ \gamma_{21} &= \frac{a_i(0)}{2} \\ \gamma_{31} &= \frac{-2a_1(0)t_{m1}-a_i(0)t_{m2}-2v_i(0)+2v_{(i,i+1)4}}{6t_{m1}(t_{m1}+t_{m2})} \\ \gamma_{12} &= \frac{2v_{(i,i+1)3}(0)t_{m1}+2v_i(0)+a_i(0)t_{m1}t_{m2}}{2(t_{m1}+t_{m2})} \\ \gamma_{22} &= \frac{-a_i(0)t_{m1}-2v_i(0)+2v_{(i,i+1)3}(0)}{2(t_{m1}+t_{m2})} \\ \gamma_{32} &= \frac{a_i(0)t_{m1}+2v_i(0)-2v_3(0)}{6t_{m2}(t_{m1}+t_{m2})} \\ \gamma_{13} &= v_{(i,i+1)3}(0) \\ \gamma_{23} &= 0 \\ \gamma_{33} &= 0 \\ \gamma_{14} &= v_{(i,i+1)3}(0) \\ \gamma_{24} &= 0 \\ \gamma_{34} &= \frac{-2(v_{(i,i+1)3}(0)-v_{i+1}(0))-a_{i+1}(0)t_{m5}}{6t_{m4}(t_{m4}+t_{m5})} \\ \gamma_{15} &= \frac{2(v_{i+1}(0)t_{m4}+v_{(i,i+1)4}(0)t_{m5})-a_{i+1}(0)t_{m4}t_{m5}}{2(t_{m4}+t_{m5})} \\ \gamma_{25} &= \frac{-(2v_{(i,i+1)3}(0)-2v_{i+1}(0)+a_{i+1}(0)t_{m5})}{2(t_{m4}+t_{m5})} \\ \gamma_{35} &= \frac{2v_{(i,i+1)3}(0)-2v_{i+1}(0)+a_{i+1}(0)t_{m4}+2a_{i+1}(0)t_{m5}}{6t_{m5}(t_{m4}+t_{m5})}\end{aligned}\quad (4.16)$$

From (4.4) and (4.9)

$$s_{(i,i+1)} = \sum_{j=1}^5 \int_0^{t_{mj}} v_{(i,i+1)j}(t_{mj}) = \sum_{j=1}^5 s_{(i,i+1)j}(t_{mj}) \quad (4.17)$$

Consider a wheeled mobile robot governed by the nonholonomic unicycle model

$$\begin{aligned} \dot{x}_r(t) &= v_r(t) \cdot \cos\phi_r(t) \\ \dot{y}_r(t) &= v_r(t) \cdot \sin\phi_r(t) \\ \dot{\phi}_r &= \omega_r(t) \end{aligned} \quad (4.18)$$

where x_r and y_r indicate the robot position with respect to a stationary frame (see Figure 3.1), ϕ_r is the heading angle, and v_r and ω_r are its linear and angular velocities to be considered as the control inputs of the robot. In order to achieve high-motion performance, these inputs $v_r(t)$ and $\omega_r(t)$ will be synthesized as C^1 -functions.

The velocity planning algorithm is:

Given a set of waypoints $\wp = A, B, C, \dots, W$, find desired inputs $v_d(t)$, $\omega_d(t)$ such that the robot starting from an arbitrary initial state:

$$A = \begin{bmatrix} x_A & y_A & \theta_A \end{bmatrix}^T, \quad \begin{aligned} v_A &= 0, & \dot{v}_A &= 0, \\ \omega_A &= 0, & \dot{\omega}_A &= 0. \end{aligned} \quad (4.19)$$

reaches the arbitrary final state:

$$W = \begin{bmatrix} x_W & y_W & \theta_W \end{bmatrix}^T, \quad \begin{aligned} v_W &= 0, & \dot{v}_W &= 0, \\ \omega_W &= 0, & \dot{\omega}_W &= 0. \end{aligned} \quad (4.20)$$

crossing all the given waypoints. The comfort of human body constraint $a_w < a_{TH}$ is to be satisfied (an adequate value is $a_{TH} = 0.31m/s^2$). The ISO 2631-1 standard [133] relates comfort with the overall r.m.s. acceleration (a_w), acting on the human body (see Table 6.2):

$$a_w = \sqrt{\tau_x^2 \cdot a_{wx}^2 + \tau_y^2 \cdot a_{wy}^2 + \tau_z^2 \cdot a_{wz}^2} \quad (4.21)$$

where a_{wx} , a_{wy} , a_{wz} , are the r.m.s. accelerations along x , y , z axes respectively, and τ_x , τ_y , τ_z , are multiplying factors. For a seated person $\tau_x = \tau_y = 1.4$, $\tau_z = 1$. For motion on the xy -plane, $a_{wz} = 0$.

Solution:

1. Determine a path connecting A (start point) with W (final point) using

$$\wp_{(i,i+1)}(u) = \begin{bmatrix} x_{(i,i+1)}(u) \\ y_{(i,i+1)}(u) \\ \theta_{(i,i+1)}(u) \end{bmatrix} = \begin{bmatrix} \alpha_{i0} + \alpha_{i1}u + \alpha_{i2}u^2 + \alpha_{i3}u^3 + \dots \\ \beta_{i0} + \beta_{i1}u + \beta_{i2}u^2 + \beta_{i3}u^3 + \dots \\ \theta_i(u) \end{bmatrix} \quad (4.22)$$

where $u \in [0, 1]$, α_{ij} and β_{ij} , with $i = A, B, C, \dots$, $j = 0, 1, \dots$ are constants to be found function of the type of the curve (e.g. cubic splines, trigonometric splines or quintic splines). Next, calculate the curvature of each segment path

$$k_{(i,i+1)}(u) = \frac{1}{\left(\dot{x}_{(i,i+1)}^2(u) + \dot{y}_{(i,i+1)}^2(u)\right)^{3/2}} \cdot \left(\dot{x}_{(i,i+1)}(u) \cdot \ddot{y}_{(i,i+1)}(u) - \ddot{x}_{(i,i+1)}(u) \cdot \dot{y}_{(i,i+1)}(u)\right) \quad (4.23)$$

and curve length

$$s_{(i,i+1)}(u) = \int_0^1 \sqrt{\dot{x}_{(i,i+1)}^2(u) + \dot{y}_{(i,i+1)}^2(u)} \cdot du \quad (4.24)$$

where $i = A, B, C, \dots$ and $u \in [0, 1]$.

2. Determine a time $t_{(i,i+1)}$ and an average velocity $\bar{v}_{(i,i+1)}$ for each segment $(i, i+1)$ of the path \wp . The time and the average velocity are calculate function of the comfort of human body constraint:

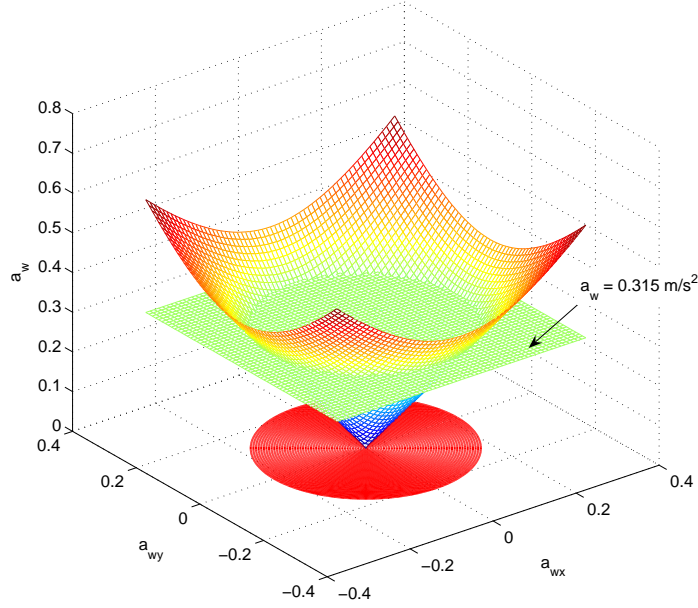
$$t_{(i,i+1)} = \sqrt{\frac{2 \cdot s_{(i,i+1)}}{a_{wxy}(i,i+1)}} \quad (4.25)$$

$$\bar{v}_{(i,i+1)} = a_{wxy}(i,i+1) \cdot t_{(i,i+1)}. \quad (4.26)$$

Accordingly (4.21) when $a_w = 0.315m/s^2$, the maximum value of a_{wx} or a_{wy} must be less than $0.225m/s^2$ (see Fig. 4.5). The most restrictive case is when the trajectory of the robot is an arc of a circle, with $a_{wxy} = a_{wx} = a_{wy}$. In this case the accelerations should be under $0.16m/s^2$, i.e. $a_{wx} = a_{wy} \leq 0.16m/s^2$.

3. Calculate an initial linear velocity profile $v_{(i,i+1)j}(t)$ with $t \in [t_i, t_{i+1}]$. Each velocity profile is generated with five properly joined spline curves:

$$v_{(i,i+1)j}(t) = \gamma_{1j} + 2 \cdot \gamma_{2j} \cdot t + 3 \cdot \gamma_{3j} \cdot t^2 \quad (4.27)$$

Figure 4.5: Restrictive cases of a_w .

where $i = A, B, C, \dots$ and $j = 1, 2, \dots, 5$. Next, calculate the curve length, $s_{(i,i+1)}(t)$, and the acceleration profile, $a_{(i,i+1)}(t)$, using:

$$s_{(i,i+1)j}(t) = \gamma_{1j} \cdot t + \gamma_{2j} \cdot t^2 + \gamma_{3j} \cdot t^3 \quad (4.28)$$

$$a_{(i,i+1)j}(t) = 2 \cdot \gamma_{2j} + 6 \cdot \gamma_{3j} \cdot t \quad (4.29)$$

where the coefficients γ are defined by (4.13).

4. Calculate angular velocity profile $\omega_{(i,i+1)}(t)$ using *Frenet formula*

$$\omega_{(i,i+1)}(t) := v_{(i,i+1)}(t) \cdot k_{(i,i+1)}(s_{(i,i+1)}) \Big|_{s_{(i,i+1)} = \int_0^t v_{(i,i+1)}(\tau) \cdot d\tau} \quad (4.30)$$

5. Calculate the overall r.m.s. acceleration $a_{w(i,i+1)}$ for each path segment using equation (4.21).
6. IF $a_{w(i,i+1)} > a_{TH}$ THEN increase the time interval for this path segment (a good performance has been achieved using an increase of 10% in each iteration) and GO TO step 3.

Consider the example depicted in Figure 4.1 where the larger circles represent

waypoints $(p_1, p_2, \dots, p_{14})$. Each waypoint is defined by a position, in meters, and an orientation, in radians. Figures 4.6 - 4.8 show results of the application of the proposed trajectory planning algorithm satisfying the comfort condition. Table 4.1 summarizes the results of the applied trajectory planning algorithm: length, time and r.m.s. acceleration values for each curve $(i, i + 1)$, $i = 1, 2, \dots, 10$. Three acceleration components are considered: lateral, longitudinal and overall acceleration. In accordance with the 6th column of Table 4.1, $a_{w(i,i+1)}$ satisfies $a_{w(i,i+1)} < 0.4m/s^2$.

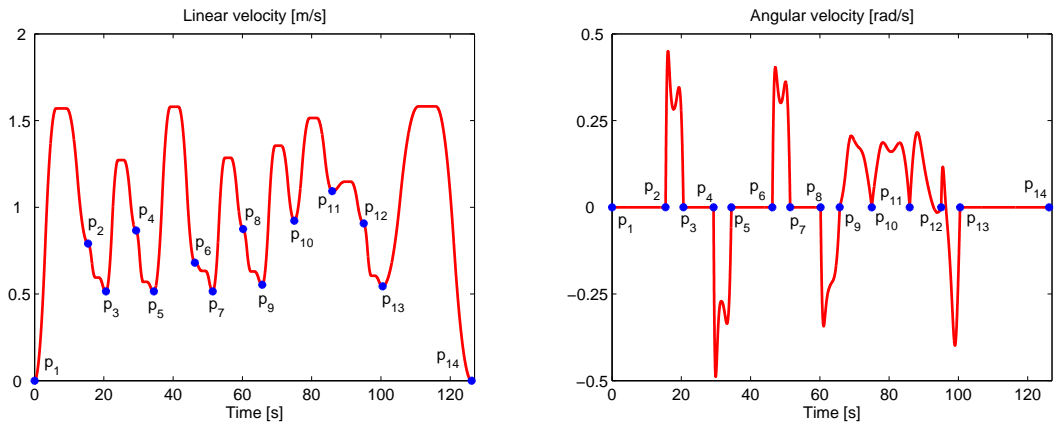


Figure 4.6: Linear and angular velocity for path example depicted in Fig. 4.1.

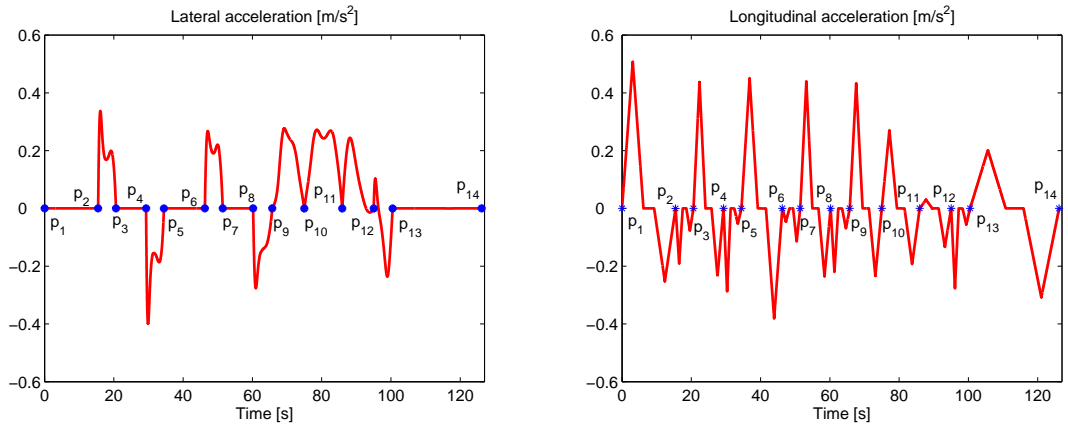


Figure 4.7: Lateral and longitudinal accelerations for path example depicted in Fig. 4.1.

Another example depicted in Figure 4.9 was considered. Figures 4.10-4.12 compares results of the application of the proposed velocity planning algorithm without (case *A*) and with (case *B*) imposing the comfort condition: $a_{w(i,i+1)} < 0.4m/s^2$. Table 4.2 summarizes the results of the applied velocity planning algorithm for both

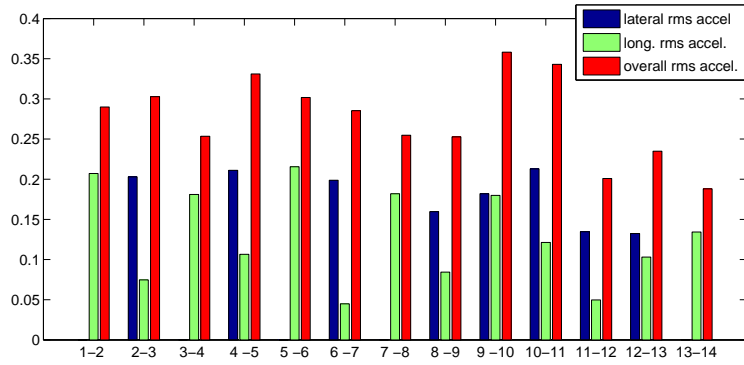


Figure 4.8: R.m.s. acceleration values for path example depicted in Fig. 4.1.

Table 4.1: Length, time and r.m.s. acceleration values for each curve

no	$s_{(i,i+1)}$ [m]	$t_{(i,i+1)}$ [s]	$a_{wx(i,i+1)}$ [m/s ²]	$a_{wy(i,i+1)}$ [m/s ²]	$a_w(i,i+1)$ [m/s ²]
1	17.0000	15.4500	0.2071	0.0000	0.2899
2	3.19000	5.1600	0.0747	0.2029	0.3027
3	9.0000	8.6600	0.1810	0.0000	0.2534
4	3.1900	5.1600	0.1065	0.2110	0.3310
5	14.0000	11.8000	0.2154	0.0000	0.3016
6	3.1900	5.1600	0.0449	0.1987	0.2852
7	9.1800	8.7500	0.1819	0.0000	0.2547
8	3.6700	5.5300	0.0843	0.1596	0.2527
9	10.2200	9.2300	0.1799	0.1818	0.3581
10	14.3500	10.9400	0.1212	0.2128	0.3429
11	9.8700	9.0700	0.0496	0.1346	0.2008
12	3.5600	5.4500	0.1030	0.1324	0.2349
13	27.1800	25.7000	0.1343	0.0000	0.1880
Total	r.m.s	acceler.	0.1523	0.1211	0.2724

$$s_{fin} = 127.60 \text{ m}$$

$$t_{fin} = 126.06 \text{ s}$$

cases (*A* and *B*): length, time and r.m.s. accelerations values for each curve between two consecutive waypoints.

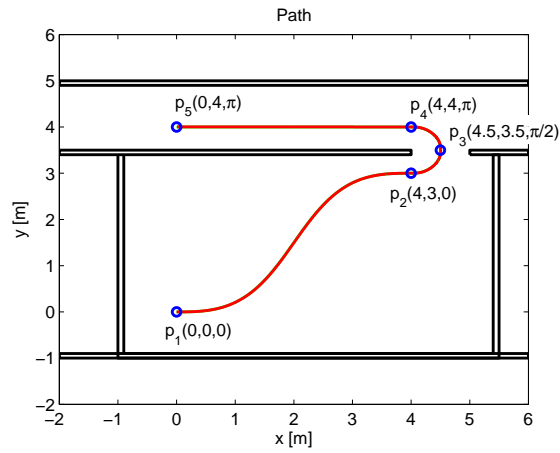


Figure 4.9: Path planning example

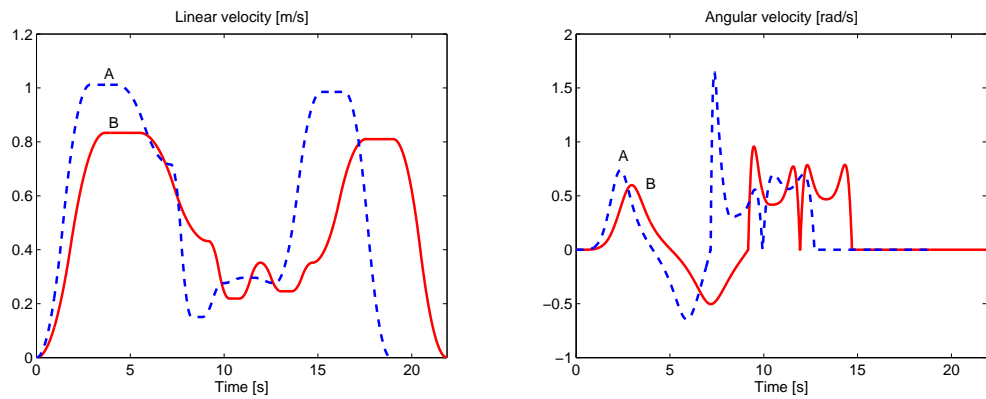


Figure 4.10: Linear and angular velocity for path example (Figure 4.9); case *A* and *B*.

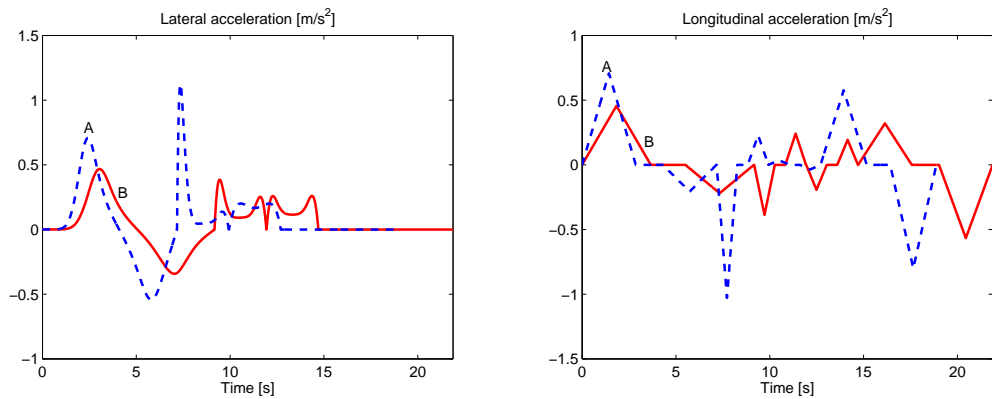


Figure 4.11: Lateral and longitudinal accelerations for path example (Figure 4.9); case *A* and *B*.

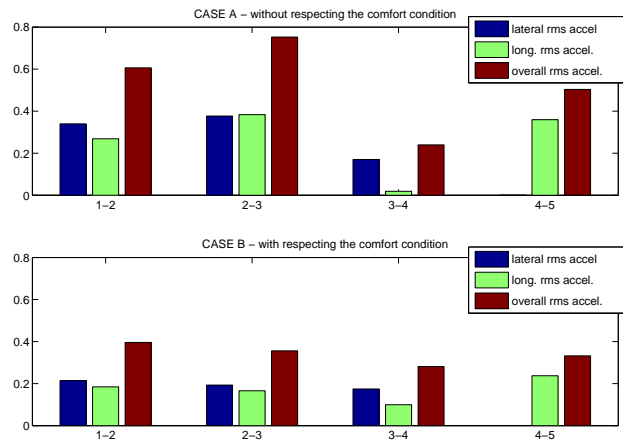
Figure 4.12: R.m.s. acceleration values for path example (Figure 4.9); case *A* and *B*

Table 4.2: Length, time and r.m.s. acceleration values for each curve (Fig. 4.9)

CASE A					
no	$s(i,i+1)$ [m]	$t(i,i+1)$ [s]	$a_{wx(i,i+1)}$ [m/s ²]	$a_{wy(i,i+1)}$ [m/s ²]	$a_w(i,i+1)$ [m/s ²]
1	5.3800	7.1600	0.2688	0.3396	0.6064
2	0.8000	2.7600	0.3834	0.3768	0.7525
3	0.8000	2.7600	0.0188	0.1701	0.2396
4	4.0000	6.1700	0.3596	0.0000	0.5034
Total	r.m.s	acceler.	0.3022	0.2624	0.5603
$s_{fin} =$	10.98 m				
$t_{fin} =$	18.85 s				
CASE B					
no	$s(i,i+1)$ [m]	$t(i,i+1)$ [s]	$a_{wx(i,i+1)}$ [m/s ²]	$a_{wy(i,i+1)}$ [m/s ²]	$a_w(i,i+1)$ [m/s ²]
1	5.3800	9.1600	0.1844	0.2141	0.3956
2	0.8000	2.7600	0.1659	0.1928	0.3561
3	0.8000	2.7600	0.0995	0.1744	0.2811
4	4.0000	7.1700	0.2372	0.0000	0.3321
Total	r.m.s	acceler.	0.1925	0.1666	0.3575
$s_{fin} =$	10.98 m				
$t_{fin} =$	21.85 s				

Chapter 5

Sliding Mode Control Design

A challenge control problem is to control a system under heavy uncertainty conditions. While there are a number of sophisticated methods like adaptation based on identification and observation, or absolute stability methods, the most obvious way to withstand the uncertainty is to keep some constraints by "brutal force". Indeed any strictly kept equality removes one "uncertainty dimension". Implemented directly, the approach leads to so-called sliding modes, which became main operation modes in the variable structure systems (VSS). Having proved their high accuracy and robustness with respect to various internal and external disturbances, they also reveal their main drawback: the so-called chattering effect, i.e. dangerous high-frequency vibrations of the controlled system. Such an effect was considered as an obvious intrinsic feature of the very idea of immediate powerful reaction to a minutest deviation from the chosen constraint. Another important feature is proportionality of the maximal deviation from the constraint to the time interval between the measurements (or to the switching delay).

5.1 Definitions and Preliminaries

In this section, a brief review of the main SMC design methods, application problems and corresponding solutions are presented. To provide a clear introduction to the key design techniques of SMC and to minimize confusion, the discussion concentrates only on linear systems or systems which are at least linear in the control variables. Some basic definitions are first given in the following:

The switching surface: Consider a general type of system represented by the

state equation,

$$\dot{x} = f(x, u, t), \quad x \in R^n, \quad u \in R^m \quad (5.1)$$

The control $u(x, t)$ with its respective entry $u_i(x, t)$ has the form:

$$u_i(x, t) = \begin{cases} u_i^+(x, t) & \text{when } s_i(x) > 0 \\ u_i^-(x, t) & \text{when } s_i(x) < 0 \end{cases} \quad i = 1, \dots, m \quad (5.2)$$

where $u_i^+(x, t)$, $u_i^-(x, t)$ and $s_i(x)$ are continuous functions. $s_i(x)$ is an $(n - 1)$ - dimensional *switching function*. Since $u_i(x, t)$ undergoes discontinuity on the surface $s_i(x) = 0$ ($s_i(x) = 0$ - is called a *switching surface* or *switching hyperplane*).

Sliding mode: Let $S = \{x | s(x) = 0\}$ be a switching surface that includes the origin $x = 0$. If, for any x_0 in S , we have $x(t)$ in S for all $t > t_0$, then $x(t)$ is a *sliding mode* of the system.

A sliding mode exists, if in the vicinity of the switching surface S , the tangent or velocity vectors of the state trajectory always point towards the switching surface.

Sliding surface: If sliding mode exists on $S = \{x | s(x) = 0\}$, i.e., if for every point in the surface there are trajectories reaching it from both sides of the surface, then the switching surface S is called a *sliding surface* or *sliding manifold*.

Reaching condition and region of attraction: Existence of a sliding mode requires stability of the state trajectory towards the sliding surface $S = \{x | s(x) = 0\}$ at least in a neighborhood of S , i.e., the representative point must approach the surface at least asymptotically. This sufficient condition for sliding mode is called *reaching condition*. The largest neighborhood of S for which the reaching condition is satisfied is called the *region of attraction*.

Reaching mode: The state trajectory under the reaching condition is called the *reaching mode* or *reaching phase*.

From the definitions above, it is shown next that an n^{th} -order system with m inputs will have $2^m - 1$ switching surfaces:

1. m surfaces of dimension $(n - 1)$, i.e., $S = \{x | s(x) = 0\}$, $i = 1, \dots, m$.
2. Consider the intersection of two surfaces S_i and S_j , $i \neq j$. Their intersection is an $(n - 2)$ -dimensional switching surface. The total number of such intersections equals the number of combinations of m surfaces S_i taken two at a time

$$\binom{m}{2} = \frac{m!}{(m-2)! \cdot 2!} = \frac{m \cdot (m-1)}{2} \quad (5.3)$$

These switching surfaces are mathematically described by $S_{ij} = S_i \cap S_j$, $i, j = 1, \dots, m$, $i \neq j$. A geometric interpretation is shown in Fig. 5.1. The intersection of the two planes, S_i and S_j , is the switching surface S_{ij} , which is a line.

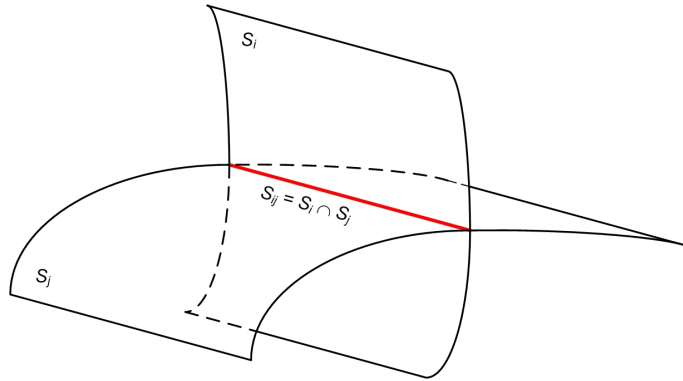


Figure 5.1: Geometric interpretation of two intersecting switching surfaces.

3. The intersection of three surfaces S_i , S_j and S_k is a switching surface S_{ijk} of dimension $(n - 3)$. There are $\binom{m}{3}$ of such surfaces; $S_{ijk} = S_i \cap S_j \cap S_k$, $i, j, k = 1, \dots, m$, $i \neq j \neq k$.

.....

4. Finally, there is a single switching surface S_E of dimension $(n - m)$, which is the intersection of all surfaces S_i , $i = 1, \dots, m$ taken together. The surface is given by $S_E = \{x | s(x) = 0\} = S_1 \cap S_2 \cap \dots \cap S_m$.

Therefore, it is possible to have $2^m - 1$ different sliding modes in such a system. The sliding mode associated with is called the *eventual sliding mode* [81]. Many authors consider only the motion on S_E as the sliding motion. However, there are many ways in which a sliding motion can begin, and these are called *switching schemes*.

Having defined all the basic concepts, the most commonly used design procedures of SMC are presented in the following sub-sections. Normally, the design of SMC consists of two parts: **First**, the sliding surface, which is usually of lower order than the given process, must be constructed such that the system performance during sliding mode satisfies the design objectives, in terms of stability, performance index minimization, linearization of nonlinearities, order reduction, etc. **Second**, the switched feedback control is designed such that it satisfies the reaching condition and thus drives the state trajectory to the sliding surface in finite time and maintains it there thereafter.

5.2 Sliding Surface Design

Sliding surfaces can be either linear or nonlinear. The theory of designing linear switching surfaces for linear dynamics system has been developed in great depth and completeness while the design of sliding surfaces for more general nonlinear systems remains a largely open problem. Some common methods for defining the differential equation of sliding mode are summarized here.

Consider a general system

$$\dot{x} = A(x) + B(x) \cdot u \quad (5.4)$$

with a sliding surface

$$S = \{x | s(x) = 0\} \quad (5.5)$$

where $A(x)$, $B(x)$ are general nonlinear functions of x , and $x \in R^n, u \in R^m$.

Canonical form: [82] For a linear single input system, if the system model can be transformed to controllable canonic form

$$\begin{aligned} \dot{x}_i &= x_{i+1}, \quad i = 1, \dots, n-1 \\ \dot{x}_n &= -\sum_{i=1}^n a_i \cdot x_i + b \cdot u \end{aligned} \quad (5.6)$$

the sliding surface can be defined by

$$\dot{s} = \frac{\partial s}{\partial x} \cdot \dot{x} = \frac{\partial s}{\partial x} s(x) = \Lambda \cdot x = \lambda_1 \cdot x_1 + \lambda_2 \cdot x_2 + \dots + x_n = 0 \quad (5.7)$$

where $\lambda_i = \text{const}$, $i = 1, 2, \dots, n-1$. The coefficients in the switch function (5.7) define the desired characteristics of the sliding mode, i.e., the characteristics of the closed loop system after the reaching phase.

Coordinate transformation [83]: If the system (5.4) is linear and described

$$\dot{x} = A \cdot x + B \cdot u \quad (5.8)$$

suppose there exists a nonsingular transformation Q such that

$$Q \cdot B = \begin{pmatrix} 0 \\ B_2 \end{pmatrix} \quad (5.9)$$

where B_2 is $m \times m$ and nonsingular. The system is then transformed to

$$\begin{aligned}\dot{x}_1 &= A_{11}x_1 + A_{12}x_2 \\ \dot{x}_2 &= A_{21}x_1 + A_{22}x_2 + B_2u\end{aligned}\tag{5.10}$$

where $x_1 \in R^{n-m}$, $x_2 \in R^m$. The switching surface can be written as $s(x) = \Lambda_1 \cdot x_1 + \Lambda_2 \cdot x_2$. Without loss of generality, we can assume that Λ_2 is nonsingular, and in sliding mode we have $\Lambda_1 \cdot x_1 + \Lambda_2 \cdot x_2 = 0$, i.e., x_2 is related linearly to x_1 and the system satisfies

$$\begin{aligned}\dot{x}_1 &= A_{11}x_1 + A_{12}x_2 \\ \dot{x}_2 &= -Kx_1\end{aligned}\tag{5.11}$$

where $K = \Lambda_2^{-1} \cdot \Lambda_1$. (5.11) represents an $(n-m)^{th}$ order system in which x_2 is viewed as the control input to the constrained system, hence the dynamic behavior of the sliding mode is determined by

$$\dot{x}_1 = (A_{11} - A_{12} \cdot K) \cdot x_1\tag{5.12}$$

The above procedures show that the design of an appropriate sliding surface has been transformed to a reduced-order state feedback design problem. In general, if the pair (A, B) is controllable, (A_{11}, A_{12}) is also controllable, thus it is possible to use classical feedback design, e.g., pole placement or linear quadratic methods to compute K such that $A_{11} - A_{12} \cdot K$ has desired characteristics. Having found K , the desired switching function can be designed as

$$s(x) = \Lambda \cdot x = \Lambda_2 \cdot [K, I] \cdot x\tag{5.13}$$

where Λ_2 can be selected arbitrary. A simple selection is to let $\Lambda_2 = I$

The linear quadratic (LQ) approach [83]: For linear time-invariant systems, optimal sliding mode, or more precisely, optimal choice of the vector K of (5.13) can be obtained by minimising a quadratic cost over an infinite time interval. For example, since x_2 can be regarded as the input of the system (5.11), LQ optimization can be used to find the optimal sliding mode for (5.11) by minimizing

$$J = \int_{t_s}^{\infty} (x_1^T \cdot Q_{11} \cdot x_1 + 2x_1^T \cdot Q_{12} \cdot x_2 + x_2^T \cdot Q_{22} \cdot x_2) dt\tag{5.14}$$

Without loss of generality, we can let $Q_{12} = 0$, and then the optimal control x_2 is

obtained by

$$x_2 = -Q_{22}^{-1} \cdot A_{12}^T \cdot P \cdot x_1 = -K \cdot x_1 \quad (5.15)$$

where P is a positive definite matrix which is the solution of the Riccati equation

$$A_{11}^T \cdot P + P \cdot A_{11} - P \cdot A_{12} \cdot Q_{22}^{-1} \cdot A_{12}^T \cdot P = -Q_{11} \quad (5.16)$$

Then the switching function (5.13) is obtained by

$$s(x) = K \cdot x_1 + x_2 = [Q_{22}^{-1} \cdot A_{12}^T \cdot P, I] \cdot x \quad (5.17)$$

Time varying surface for tracking control [84], [85]: For a single input system, one way is to define the sliding surface according to the desired control bandwidth

$$s(x, t) = \left(\frac{d}{dt} + \lambda \right)^{n-1} \cdot x = 0 \quad (5.18)$$

where x is the tracking error and λ is a strictly positive constant which determines the closed-loop bandwidth. We can see that s depends only on the tracking error x . For example, if $n = 2$,

$$s = \dot{x} + \lambda \cdot x \quad (5.19)$$

which is simply a weighted sum of the position and velocity errors; and if $n = 3$,

$$s = \ddot{x} + 2 \cdot \lambda \cdot \dot{x} + \lambda^2 \cdot x \quad (5.20)$$

It can also be seen that the scalar s represents a true measure of tracking performance.

Equivalent control method [86]: The equivalent control is found by recognizing that $\dot{s}(x) = 0$ is a necessary condition for the state trajectory to stay on the sliding surface $s(x) = 0$. Therefore, setting $\dot{s}(x) = 0$, i.e.,

$$\dot{s} = \frac{\partial s}{\partial x} \cdot \dot{x} = \frac{\partial s}{\partial x} \cdot A(x) + \frac{\partial s}{\partial x} \cdot B(x) \cdot u_{eq} = 0 \quad (5.21)$$

Solving (5.21) for u_{eq} yields the equivalent control

$$u_{eq} = -\frac{\partial s}{\partial x} \cdot A(x) \cdot \left(\frac{\partial s}{\partial x} \cdot B(x) \right)^{-1} \quad (5.22)$$

where $\frac{\partial s}{\partial x} \cdot B(x)$ is nonsingular.

The dynamics of the system is governed by:

$$\dot{x} = \left(I - B(x) \cdot \left(\frac{\partial s}{\partial x} \cdot B(x) \right)^{-1} \cdot \frac{\partial s}{\partial x} \right) \cdot A(x) \quad (5.23)$$

If the system (5.4) is linear and described by

$$\dot{x} = A \cdot x + B \cdot u \quad (5.24)$$

where A and B are properly dimensioned constant matrices, then the switch surface can be defined as

$$s(x) = \Lambda \cdot x(t) = 0 \quad (5.25)$$

i.e., $\frac{\partial s}{\partial x} = \Lambda$, where $\Lambda = [\lambda_1, \dots, \lambda_m]^T$ is a $m \times n$ matrix, and then we have:

$$u_{eq} = -(\Lambda \cdot B)^{-1} \cdot \Lambda \cdot A \cdot x \quad (5.26)$$

and (5.23) becomes

$$\dot{x} = \left(I - B \cdot (\Lambda \cdot B)^{-1} \cdot \Lambda \right) \cdot A \cdot x \quad (5.27)$$

Equations (5.23) and (5.27) describe the behavior of the systems (5.4) and (5.24), respectively, which are restricted to the switching surface if the initial condition $x(t_0)$ satisfies $s(x(t_0)) = 0$. For the linear case, the system dynamics is ensured by a suitable choice of the feedback matrix $K = (\Lambda \cdot B)^{-1} \cdot \Lambda \cdot A$. In other words, the choice of the matrix Λ can be made without prior knowledge of the form of the control vector u .

Dynamic sliding surface/frequency-shaped sliding surface [87]: The sliding surfaces designed above are all static, i.e., they are different linear combinations of the state variables. Young and Ozguner in [87] proposed a new type of switching surface which appears as a linear operator. The purpose of the design was to attenuate high frequency components in the error dynamics, thus to avoid vibrations due to the interaction of sliding mode and unmodelled dynamics of the system.

Other methods for design of both linear and nonlinear sliding surfaces can also be found in the literature, such as designing robust sliding hyperplanes via a Riccati approach (Kim, et al., 2000), constructing a discontinuous surface for VSS by a Lyapunov approach (Su, et al., 1996b) and designing an adaptive sliding surface for model reference VSC (Nonaka, et al., 1996; Yao and Tomizuka, 1994; Su and Leung,

1993; Bartolini, et al.,1997; Bartolini and Ferrara,1999).

5.3 Control Law Design

Once the sliding surfaces have been selected, attention must be turned to solving the reachability problem. This involves the selection of a state feedback control function $u : R^n \rightarrow R^m$ which can drive the state x towards the surface and thereafter maintains it on the surface. In other words, the controlled system must satisfy the reaching conditions. For general MIMO systems, different switching schemes use different reaching laws during approach of the sliding mode. The commonly used reaching laws and the developed control methods were summarized in [81] and [88].

Reaching laws

For both SISO and MIMO systems, the commonly used reaching conditions are specified in the following forms:

- *The direct switching function approach*

The classic sufficient condition for sliding mode to appear is to satisfy the condition

$$s_i \cdot \dot{s}_i < 0, \quad i = 1, \dots, m \quad (5.28)$$

and a similar condition was also proposed in [82], i.e.,

$$\lim_{s_i \rightarrow 0^+} \dot{s}_i < 0 \quad \text{and} \quad \lim_{s_i \rightarrow 0^-} \dot{s}_i > 0 \quad (5.29)$$

These reaching laws result in a VSC where individual switching surfaces and their intersection are all sliding surfaces. This reaching is global but does not guarantee finite reaching time.

- *The Lyapunov function approach*

Choosing the Lyapunov function candidate

$$V(x, t) = \frac{1}{2} \cdot s^T \cdot s \quad (5.30)$$

The global reaching condition is then given by

$$\dot{V}(x, t) < 0 \quad (5.31)$$

This reaching law results in a VSC where sliding mode is guaranteed only on the

intersection of all switching surfaces, i.e., the *eventual sliding mode*, whereas points on the individual switching surfaces may or may not belong to the sliding surface. Finite reaching time can be guaranteed if (5.31) is modified to $\dot{V}(x,t) < -\epsilon$, ϵ is strictly positive.

- *Gao's reaching law approach* Gao and Hung in [89] proposed a reaching law which directly specifies the dynamics of the switching surface by the differential equation

$$\dot{s} = -Q \cdot \text{sgn}(s) - P \cdot h(s) \quad (5.32)$$

where

$$Q = \text{diag} [q_1, q_2, \dots, q_m], \quad q_i > 0, \quad i = 1, 2, \dots, m$$

$$P = \text{diag} [p_1, p_2, \dots, p_m], \quad p_i > 0, \quad i = 1, 2, \dots, m$$

and

$$\text{sgn}(s) = [\text{sgn}(s_1), \text{sgn}(s_2), \dots, \text{sgn}(s_m)]^T$$

$$h(s) = [h_1(s_1), h_2(s_2), \dots, h_m(s_m)]^T$$

$$s_i \cdot h_i(s) > 0, \quad h_i(0) = 0.$$

Three practical special cases of (5.32) are given below.

A. Constant rate reaching

$$\dot{s} = -Q \cdot \text{sgn}(s) \quad (5.33)$$

This law forces the switching variable $s(x)$ to reach the switching manifold S at a constant rate $|\dot{s}_i| = -q_i$. The merit of this reaching law is its simplicity. But, as we know, if q_i is too small, the reaching time will be too long. On the other hand, a too large q_i will cause severe chattering.

B. Constant plus proportional rate reaching

$$\dot{s} = -Q \cdot \text{sgn}(s) - P \cdot s \quad (5.34)$$

Clearly, by adding the proportional rate term $-P \cdot s$, the state is forced to approach the switching manifolds faster when s is large. It can be shown that the reaching

time for x to move from an initial state x_0 to the switching manifold s_i is finite, and is given by:

$$T_i = \frac{1}{p_i} \cdot \ln \frac{p_i \cdot |s_i| + q_i}{q_i} \quad (5.35)$$

C. Power rate reaching

$$\dot{s}_i = -p_i \cdot |s_i|^\alpha \cdot \text{sgn}(s_i), \quad 0 < \alpha < 1, \quad i = 1, \dots, m \quad (5.36)$$

This reaching law increases the reaching speed when the state is far away from the switching manifold, but reduces the rate when the state is near the manifold. The result is a fast reaching and low chattering reaching mode. Integrating (5.36) from $s_i = s_{i0}$ to $s_i = 0$ yields

$$T_i = \frac{|s_i(0)|^{1-\alpha}}{(1-\alpha) \cdot p_i} \quad (5.37)$$

showing that the reaching time T_i , is finite. Thus power rate reaching law gives a finite reaching time. In addition, because of the absence of the $-Q \cdot \text{sgn}(s)$ term on the right-hand side of (5.36), this reaching law eliminates the chattering.

A particular form of speed control relationship in the reaching phase was developed in [90]:

C'. Particular rate reaching

$$\dot{s}_i = -p_i \cdot \exp(\alpha \cdot |s_i|) \cdot \text{sgn}(s_i), \quad p_i > 0, \quad \alpha > 0, \quad i = 1, \dots, m \quad (5.38)$$

and the reaching time T_i becomes:

$$T_i = \frac{1}{\alpha \cdot p_i} \cdot (1 - \exp(-\alpha \cdot |s_i(0)|)) \quad (5.39)$$

Control laws

Having selected the reaching law equation, the control law can now be determined. In this section, various design approaches are presented.

- Augmenting the equivalent control

Recall that during sliding mode, one can compute the equivalent control u_{eq} according to (5.22) or (5.26). However, only using cannot drive the state towards the sliding surface S if the initial conditions of the system are not on S . One popular design method is to augment the equivalent control with a discontinuous or switched part, i.e.,

$$u = u_{eq} + u_N \quad (5.40)$$

where u_N is added to satisfy the reaching condition which may have different forms. For a controller having the structure of (5.40), we have

$$\begin{aligned}\dot{s}(x) &= \frac{\partial s}{\partial x} \cdot \dot{x} = \frac{\partial s}{\partial x} \cdot [A(x) + B(x) \cdot (u_{eq} + u_N)] \\ &= \frac{\partial s}{\partial x} \cdot [A(x) + B(x) \cdot u_{eq}] + \frac{\partial s}{\partial x} \cdot B(x) \cdot u_N \\ &= \frac{\partial s}{\partial x} \cdot B(x) \cdot u_N\end{aligned}\quad (5.41)$$

For simplicity, assume $\frac{\partial s}{\partial x} \cdot B(x) = I$, the identity. Then $\dot{s}(x) = u_N$. According to [88] some often used forms of u_N are given below

A - Relay with gains

$$u_N = \begin{cases} -\alpha \cdot \text{sgn}(s), & s \neq 0, \alpha > 0 \\ 0, & s = 0, \end{cases}\quad (5.42)$$

α can be either a constant matrix or state dependent $\alpha(x)$. Each control unit u_{Ni} meets the reaching condition since

$$\dot{s}_i \cdot s_i = -\alpha \cdot s_i(x) \cdot \text{sgn}(s_i(x)) < 0, \text{ for } s_i(x) \neq 0\quad (5.43)$$

B - Linear feedback with switching gains

$$u_{Ni} = \psi \cdot x; \quad \psi = [\psi_{ij}], \quad \psi_{ij} = \begin{cases} -\alpha_{ij}, & s_i \cdot x_j > 0 \\ \beta_{ij}, & s_i \cdot x_j < 0 \end{cases}\quad (5.44)$$

with $\alpha_{ij}, \beta_{ij} > 0$. The reaching condition is satisfied with

$$\dot{s}_i \cdot s_i = s_i \cdot (\psi_{i1} \cdot x_1 + \psi_{i2} \cdot x_2 + \dots + \psi_{in} \cdot x_n) < 0\quad (5.45)$$

C - Linear continuous feedback

$$u_N = -\alpha \cdot s(x)\quad (5.46)$$

where α is defined in the same way as above, and hence the reaching condition is

$$\dot{s}_i \cdot s_i = -\alpha \cdot s_i^2(x) < 0\quad (5.47)$$

D - Univector nonlinearity with scalar factor

$$u_N = -\frac{s(x)}{\|s(x)\|} \cdot \gamma \quad (5.48)$$

where $\gamma > 0$ is a scalar. Thus the reaching condition is satisfied with

$$\dot{s}(x) \cdot s^T(x) = -\|s(x)\| \cdot \gamma < 0 \text{ if } s(x) \neq 0 \quad (5.49)$$

- The reaching law method

By using the reaching law approach proposed in [81], the control can be directly obtained by computing the time derivative $s(x)$ of along the reaching mode trajectory, i.e.,

$$\dot{s} = \frac{\partial s}{\partial x} \cdot (A(x) + B(x) \cdot u) = -Q \cdot \text{sgn}(s) - P \cdot h(s) \quad (5.50)$$

Thus, we have

$$u = -\left(\frac{\partial s}{\partial x} \cdot A(x) + Q \cdot \text{sgn}(s) + P \cdot h(s)\right) \cdot \left(\frac{\partial s}{\partial x} \cdot B(x)\right)^T \quad (5.51)$$

By this approach, the resulting sliding mode is not preassigned but follows the natural trajectory on a first-reach-first-switch scheme. The switching takes place depending on the location of the initial state.

- Control hierarchy method

The hierarchical control method uses the first reaching law i.e., the classical sufficient condition for a sliding mode. This method is used to establish a control scheme, such that sliding modes take place in a preassigned order, i.e., the system state starts from the initial condition x_0 , moves progressively onto lower dimensional switching surfaces and eventually reaches the final sliding surface S_E :

$$x_0 \rightarrow S_1 \rightarrow (S_1 \cap S_2) \rightarrow (S_1 \cap S_2 \cap S_3) \rightarrow \dots \rightarrow S_E$$

The disadvantage of this method is that the control is determined by a set of complicated inequalities. For example, for the system (5.24), the determination of the control u involves the solution of m pairs of inequalities,

$$\dot{s}_i = \frac{\partial s_i}{\partial x} \cdot (A \cdot x + B \cdot u) = \begin{cases} > 0, \text{ when } s_i < 0 \\ < 0, \text{ when } s_i > 0 \end{cases}, \quad i = 1, \dots, m \quad (5.52)$$

Solving (5.52) is usually a very difficult task. As a result, the scheme is seldom used.

5.4 Chattering Problem and its Reduction

It has already been mentioned that to guarantee the desired behaviour of the close-loop system, the sliding mode controllers require an infinitely fast switching mechanism. However, due to physical limitations in real-world systems, directly applying the above developed control algorithms will always lead to oscillations in some vicinity of the switching surface, i.e., the so called *chattering phenomenon*. There are two possible mechanisms which produce chattering (Young, et al., 1999). First, chattering may be caused by the switching nonidealities, such as time delays or time constants, which exist in any implementation of switching devices, typically including both analog and digital circuits as well as microprocessor based implementations. Second, even if the switching device is considered ideal and capable of switching at an infinite frequency, the presence of parasitic dynamics, i.e., unmodelled dynamics, also causes chattering to appear in the neighborhood of the sliding surface. The parasitic dynamics are those of fast dynamics of actuators, sensors and other high frequency modes of the controlled process, which are usually neglected in the open-loop model used for control design if the associated poles are well damped and outside the desired bandwidth of the feedback control system. However, in sliding mode controlled systems, due to the discontinuity of the control signal, the interactions between the parasitic dynamics and the switching term may result in a nondecaying oscillation with finite amplitude and frequency, i.e., chattering. If the switching gain is large, such kind of chattering may even cause unpredictable instability.

The chattering problem is considered as a major obstacle for SMC to become a more appreciated control method among practicing control engineers. To reduce the chattering effect has long been a major objective in research on SMC. The existing approaches for chattering reduction in design of SMC are summarized in the following.

Boundary layer control [84], [85]: A boundary layer around the sliding surface is specified. Inside the boundary layer, the switching function is usually replaced by a linear feedback gain, thus the control signal becomes continuous and chattering is avoided. The shortcoming of this approach is that the robustness properties of the sliding mode are actually lost inside the boundary layer, such that uncertainties and parasitic dynamics must be carefully considered and modeled in the feedback design in order to avoid instability.

Observer-based sliding mode control [86], [91], [92]: This approach utilizes asymptotic state observers to construct a high frequency by pass loop, i.e., the control

is discontinuous only with respect to the observer variables, thus chattering is localized inside the observer loop which bypasses the plant, see Fig. 5.2. This approach assumes that an asymptotic observer can indeed be designed such that the observation error converges to zero asymptotically.

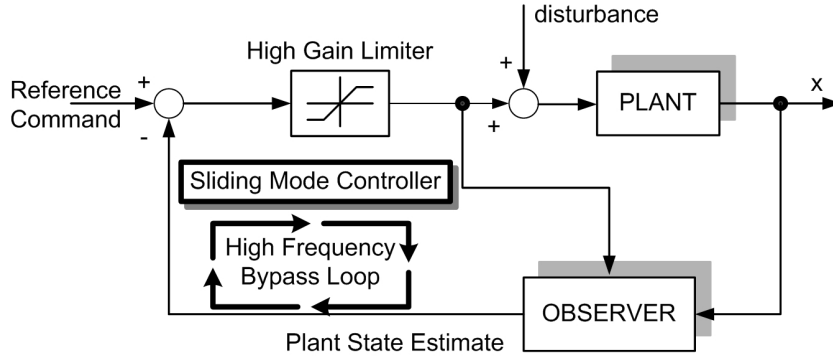


Figure 5.2: Block diagram of observer based sliding mode control.

Disturbance observer and compensation [93], [94]: A disturbance may be compensated first by introducing a disturbance observer, in this case the switching gain will depend on the upper bound of the disturbance estimation error, instead of the disturbance upper bound itself, thus a SM control can be obtained by a much lower switching gain than in its conventional counterparts. The disturbance observer can also be sliding mode based, in this case the control law consists of a conventional continuous feedback control component and a component derived from the SM disturbance estimator for disturbance compensation. If the compensation is sufficient, there is no need to employ a discontinuity in the feedback control for achieving sliding mode. Hence, the chattering is no longer a matter of concern since a conventional feedback control instead of SMC is applied. This scheme is illustrated in Fig. 5.3.

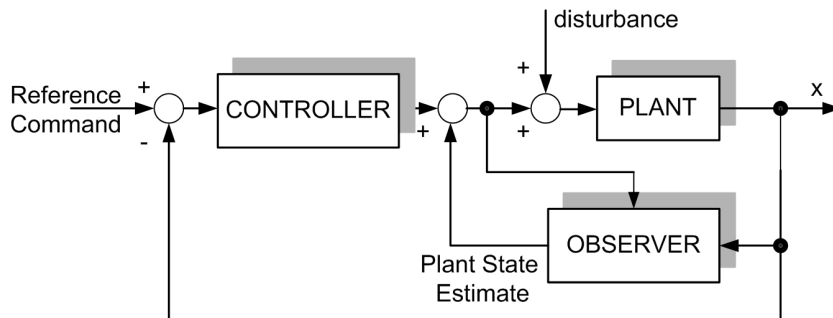


Figure 5.3: Disturbance compensation with sliding mode disturbance observer.

High-order/second-order sliding mode control [95], [96]: The control action is in this case a function of higher order time derivatives of the sliding variable. For example, the second order sliding mode approach allows the definition of a discontinuous control \dot{u} steering both the sliding variable s and its time derivative \dot{s} to zero, so that the plant input u is a continuous control and thus chattering can be avoided. The difficulty is that there is no general method for tuning the parameters which characterize the various algorithms.

VSC control with sliding sector [97]: A Lyapunov function is used as an effective method to design a robust controller for uncertain systems. For a single input system described as $\dot{x} = A \cdot x + B \cdot u, x \in R^n$, a Lyapunov function candidate is usually chosen as the square of the P-norm, i.e.,

$$V = \|x\|_p^2 = x^T \cdot P \cdot x > 0, x \neq 0 \quad (5.53)$$

where P is a positive definite symmetric matrix. It has been proved by the authors that for any controllable system, there always exists a special subset around a hyperplane, inside which the P-norm decreases, i.e., $\dot{V} \leq -x^T \cdot R \cdot x$ without needing any control action, where R is a positive semi-definite symmetric matrix. Such a subset is named as the PR-sliding sector. One can use this property to design a VS controller such that outside the sliding sector, the VS control law is used to move the state into the sliding sector, and once the state is inside the sector, the Lyapunov function decreases with a specified velocity and zero input.

5.5 Sliding Mode Trajectory-Tracking Control for WMR

It is supposed that a feasible desired trajectory for the mobile robot is pre-specified by a velocity planner. The problem is to design a robust controller so that the robot will correctly track the desired trajectory under a large class of disturbances.

We consider a unicycle WMR having the following simplified nonholonomic system:

$$\begin{cases} \dot{x}_r(t) = v_r(t) \cdot \cos\phi_r(t) \\ \dot{y}_r(t) = v_r(t) \cdot \sin\phi_r(t) \\ \dot{\phi}_r(t) = \omega_r(t) \end{cases} \quad (5.54)$$

where x_r and y_r are the Cartesian coordinates of the geometric center, v_r is the linear velocity, ϕ_r is the vehicle's heading angle and ω_r is the angular velocity (see Figure 3.1).

The trajectory tracking errors can be described by (x_e, y_e, ϕ_e) . The aim of this section is to design a stable controller that generates a command vector (v_c, ω_c) .

From Figure 3.6, the error vector for trajectory-tracking is

$$\begin{bmatrix} x_e \\ y_e \\ \phi_e \end{bmatrix} = \begin{bmatrix} \cos\phi_d & \sin\phi_d & 0 \\ -\sin\phi_d & \cos\phi_d & 0 \\ 0 & 0 & 1 \end{bmatrix} \cdot \begin{bmatrix} x_r - x_d \\ y_r - y_d \\ \phi_r - \phi_d \end{bmatrix} \quad (5.55)$$

where: (x_d, y_d, ϕ_d) is the virtual robot pose.

The corresponding error derivatives are:

$$\begin{cases} \dot{x}_e = -v_d + v_r \cdot \cos\phi_e + y_e \cdot \omega_d \\ \dot{y}_e = v_r \cdot \sin\phi_e - x_e \cdot \omega_d \\ \dot{\phi}_e = \omega_r - \omega_d \end{cases} \quad (5.56)$$

where v_d and ω_d are the desired linear and angular velocities, respectively.

In this thesis it is assumed that $|\phi_e| < \pi/2$, which means that the robot orientation must not be perpendicular to the desired trajectory.

We propose a new design of sliding surface such that lateral error, y_e , and angular variable, ϕ_e , are internally coupled with each other in a sliding surface leading to convergence of both variables. For that purpose the following sliding surfaces are proposed:

$$s_1 = \dot{x}_e + k_1 \cdot x_e \quad (5.57)$$

$$s_2 = \dot{y}_e + k_2 \cdot y_e + k_0 \cdot \text{sgn}(y_e) \cdot \phi_e \quad (5.58)$$

where k_0, k_1, k_2 are positive constant parameters, x_e, y_e and θ_e are the trajectory-tracking errors defined in (5.55).

If s_1 converges to zero, trivially x_e converges to zero. If s_2 converges to zero, in steady-state it becomes $\dot{y}_e = -k_2 \cdot y_e - k_0 \cdot \text{sgn}(y_e) \cdot \phi_e$. For $y_e < 0 \Rightarrow \dot{y}_e > 0$ if only if $k_0 < k_2 \cdot |y_e| / |\phi_e|$. For $y_e > 0 \Rightarrow \dot{y}_e < 0$ if only if $k_0 < k_2 \cdot |y_e| / |\phi_e|$. Finally, it can be known from s_2 that convergence of y_e and \dot{y}_e leads to convergence of ϕ_e to zero.

A practical general form of reaching the control law is:

$$\dot{s} = -Q \cdot s - P \cdot \text{sgn}(s) \quad (5.59)$$

where Q and P are positive constant values. By adding the proportional rate term $-Q \cdot s$, the state is forced to approach the switching manifold faster when s is large.

From the time derivations of (5.57) and (5.58), and knowing that

$$\dot{\phi}_e = \dot{\phi}_r - \dot{\phi}_d = \omega_r - \omega_d$$

after some mathematical manipulation one achieves

$$\dot{v}_c = \frac{-Q_1 \cdot s_1 - P_1 \cdot \text{sgn}(s_1) - k_1 \cdot \dot{x}_e - \dot{\omega}_d \cdot y_e - \omega_d \cdot \dot{y}_e + v_r \cdot \dot{\phi}_e \cdot \sin\phi_e + \dot{v}_d}{\cos\phi_e} \quad (5.60)$$

$$\omega_c = \frac{-Q_2 \cdot s_2 - P_2 \cdot \text{sgn}(s_2) - k_2 \cdot \dot{y}_e - \dot{v}_r \cdot \sin\phi_e + \dot{\omega}_d \cdot x_e + \omega_d \cdot \dot{x}_e}{v_r \cdot \cos\phi_e + k_0 \cdot \text{sgn}(y_e)} + \omega_d \quad (5.61)$$

Let us define $V = \frac{1}{2} \cdot s^T \cdot s$ as a Lyapunov function candidate, therefore its time derivative is

$$\begin{aligned} \dot{V} &= s_1 \cdot \dot{s}_1 + s_2 \cdot \dot{s}_2 = s_1 \cdot (-Q_1 \cdot s_1 - P_1 \cdot \text{sgn}(s_1)) + s_2 \cdot (-Q_2 \cdot s_2 - P_2 \cdot \text{sgn}(s_2)) = \\ &= -s^T \cdot Q \cdot s - P_1 \cdot |s_1| - P_2 \cdot |s_2| \end{aligned}$$

For \dot{V} to be negative semi-definite, it is sufficient to choose Q_i and P_i such that $Q_i, P_i \geq 0$.

5.5.1 Simulation Results

In this subsection, simulation results of the proposed method are presented. The simulation model block diagrams are shown in Figs. 5.4 and 5.5.

Figures 5.7 and 5.8 were automatically generated by the trajectory planner described in Chapter 4. These profiles are generated respecting the human comfort condition ($a_w < 0.31 \text{ m/s}^2$). This result can be observed in the graphics shown in Fig. 5.8, which are related with the trajectories shown in Fig. 5.6.

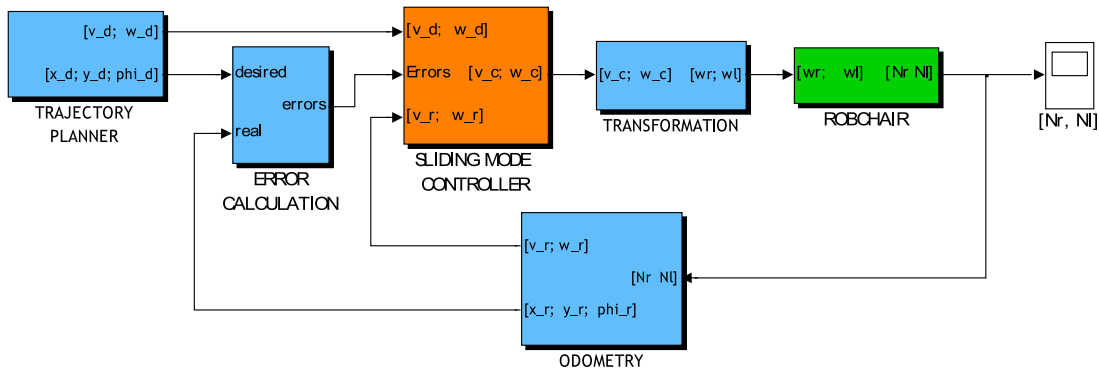


Figure 5.4: Simulation model block diagram (Simulink scheme).

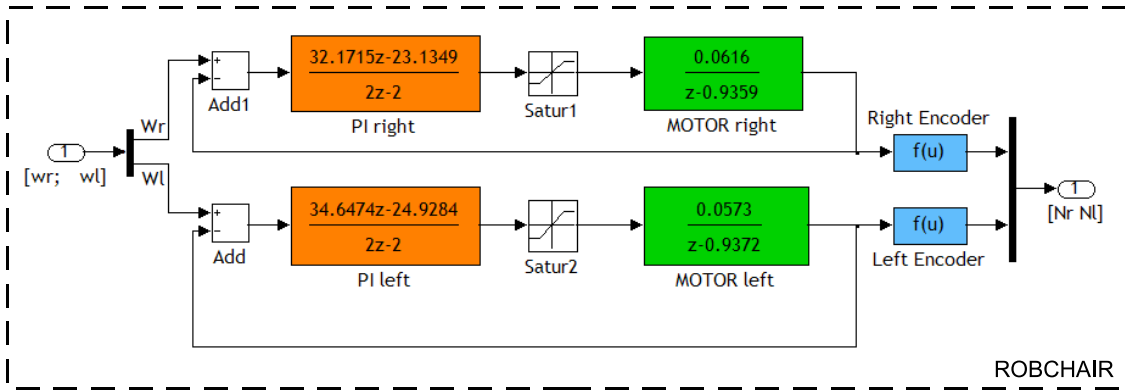


Figure 5.5: Simulink model for RobChair.

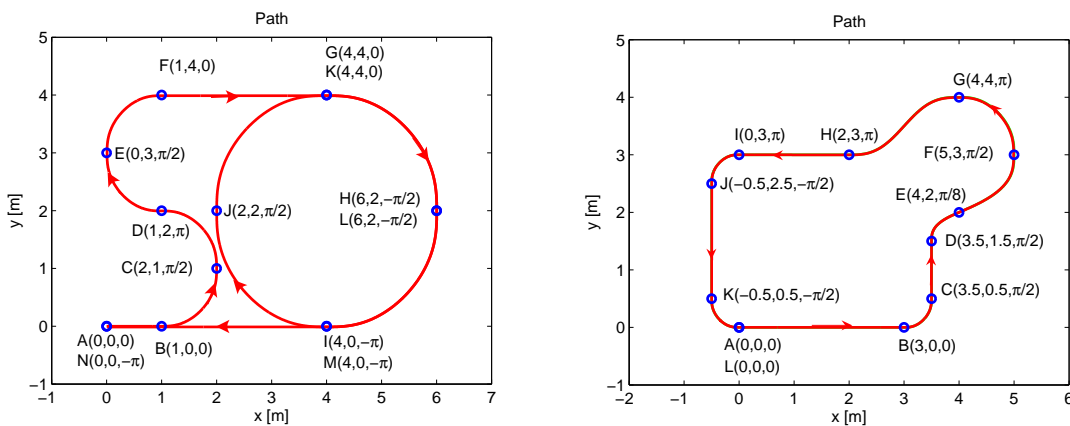


Figure 5.6: Path examples calculated by the trajectory planner (see Chapter 4).

Figures 5.9 - 5.12 indicate the results of the simulation in closed-loop using SM-TT control described above. We can observe that profiles of the velocities and accelerations are similar to those desired (depicted in Fig. 5.7).

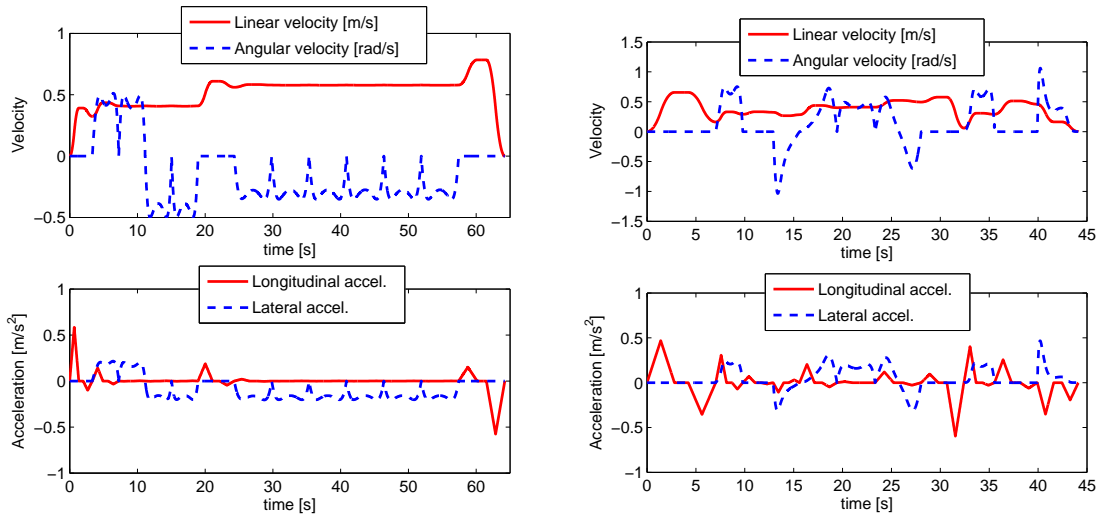


Figure 5.7: Velocities and accelerations for the path depicted in Fig. 5.6.

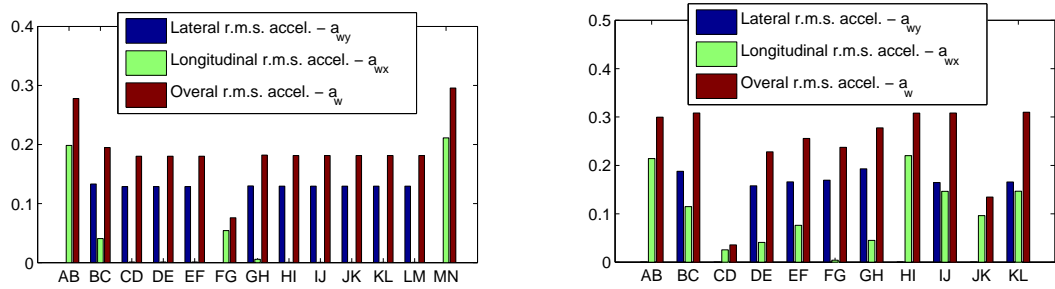


Figure 5.8: R.M.S. acceleration values for each path-segment (AB, BC,...) of the paths depicted in Fig. 5.6.

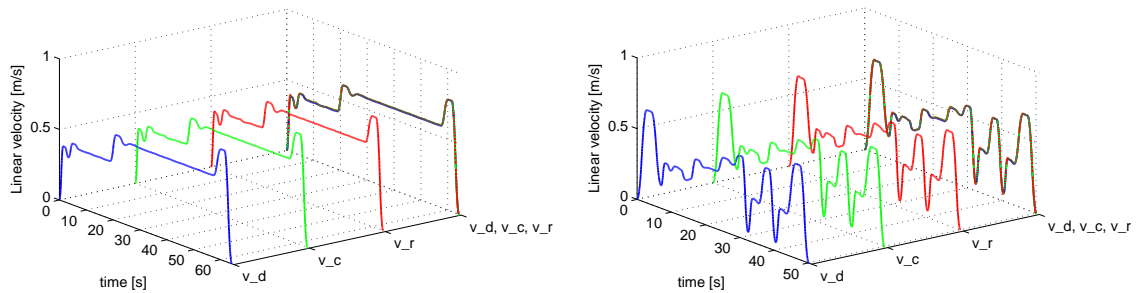


Figure 5.9: Desired v_d , command v_c and real v_r linear velocities for SM-TT control - Path 1 and Path 2.

From Fig. 5.13 we can observe that position errors (x_e and y_e) and orientation error (ϕ_e) are maintained around zero. Simulation results of the SM-TT controller, for the case with initial pose errors, are shown in Fig. 5.14a. After the initial error conditions, the pose error converges to zero as shown in Fig. 5.14b. The same figure

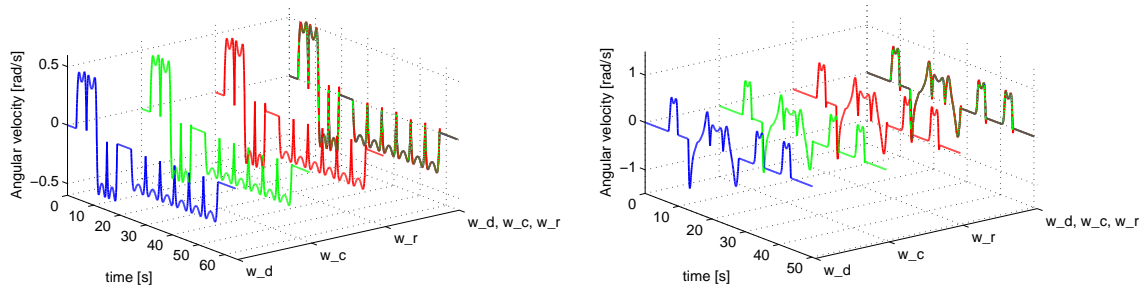


Figure 5.10: Desired ω_d , command ω_c and real ω_r angular velocities for SM-TT control - Path1 and Path 2.

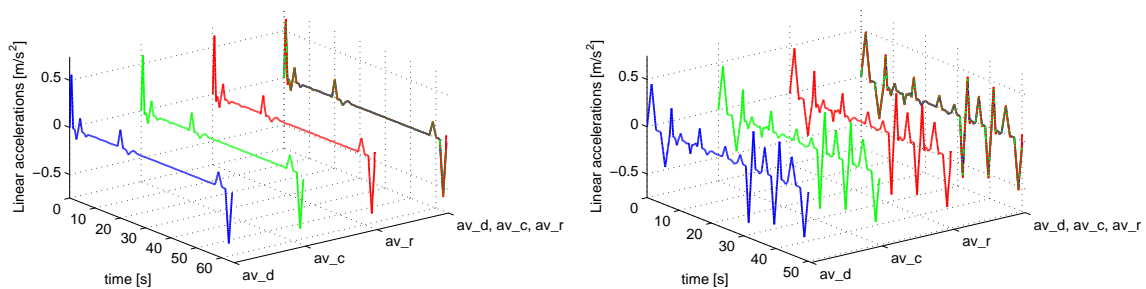


Figure 5.11: Desired av_d , command av_c and real av_r longitudinal accelerations for SM-TT control - Path 1 and Path 2.

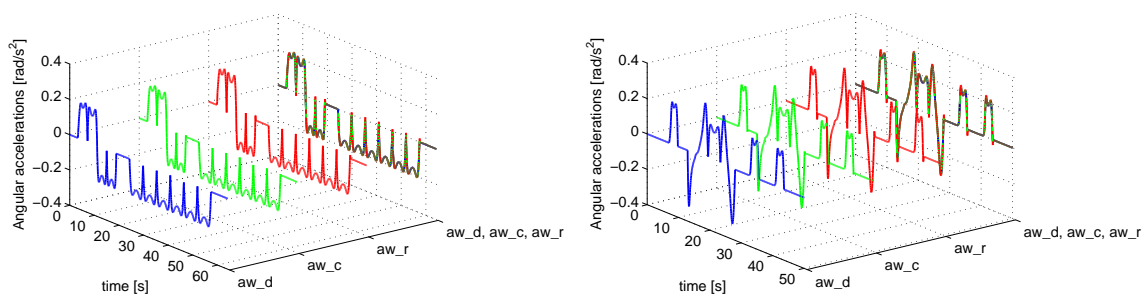


Figure 5.12: Desired aw_d , command aw_c and real aw_r angular accelerations for SM-TT control - Path1 and Path 2.

shows that the robot retrieved quickly ($\Delta t \approx 5$ s) and smoothly from its initial pose error.

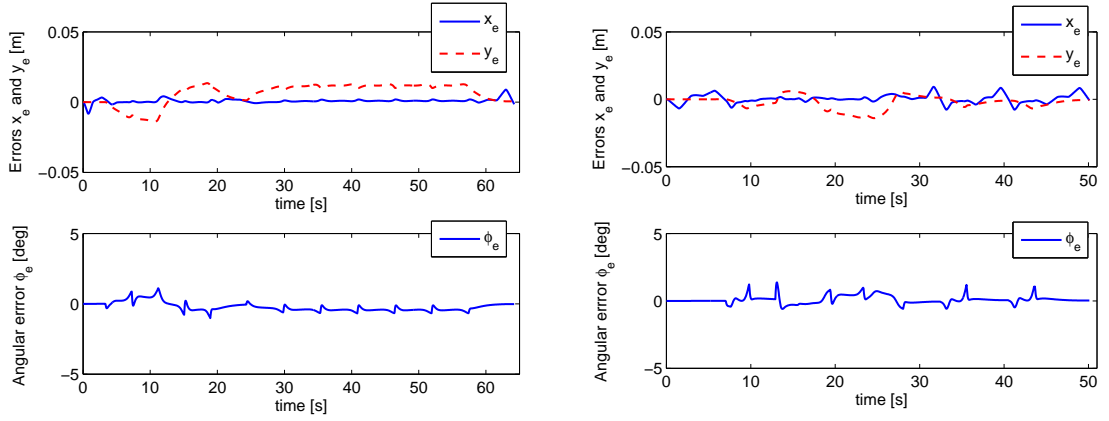


Figure 5.13: Longitudinal, lateral and angular errors of SM-TT control - Path 1 and Path 2.

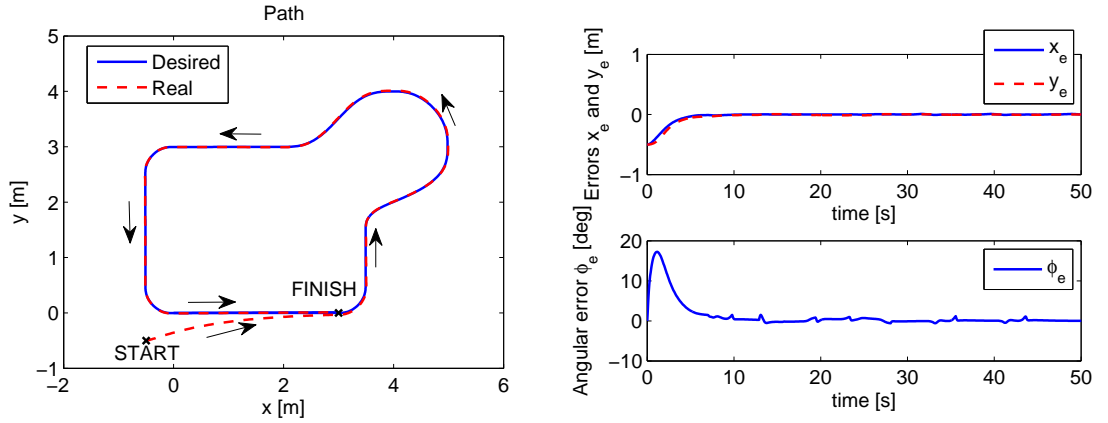


Figure 5.14: Simulation SM-TT control starting from an initial error state ($x_e(0) = -0.5$, $y_e(0) = -0.5$, $\phi_e(0) = 0$).

5.6 Sliding Mode Trajectory-Tracking Control for Car-like Vehicle

It is supposed that a feasible desired trajectory for the vehicle is pre-specified by a trajectory planner. The problem is to design a robust controller so that the vehicle will correctly track the desired trajectory under a large class of disturbances.

We consider as a motion model of a vehicle the following simplified nonholonomic system:

$$\begin{cases} \dot{x}_r(t) = v_r(t) \cdot \cos\phi_r(t) \\ \dot{y}_r(t) = v_r(t) \cdot \sin\phi_r(t) \\ \dot{\phi}_r(t) = \frac{v_r}{L} \cdot \tan\delta_r(t) \end{cases} \quad (5.62)$$

where (see Fig. 5.15) x_r and y_r are the Cartesian coordinates of the rear axle midpoint,

v_r is the velocity of this midpoint, ϕ_r is the vehicle's heading angle, L is the inter-axle distance, and δ_r the front wheel angle, which is the control variable to steer the vehicle.

In this section, the kinematic bicycle model is considered (see Figs. 5.15 - 5.16). The trajectory tracking errors can be described by (x_e, y_e, ϕ_e) . The aim is to design a stable controller with commands (v_c, δ_c) .

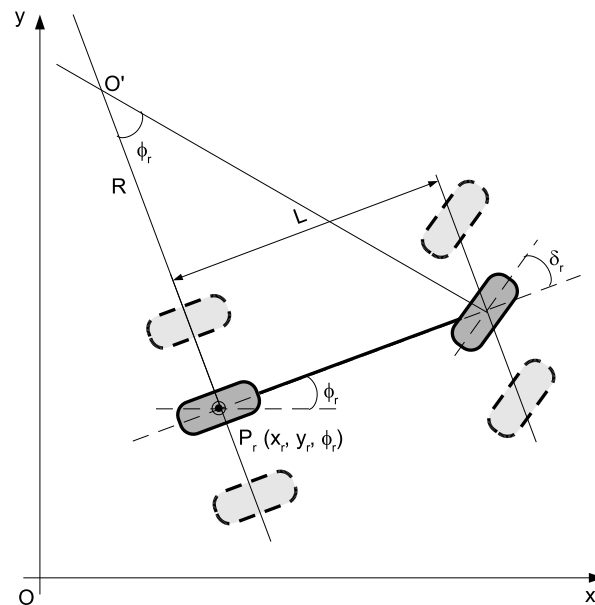


Figure 5.15: Bicycle model (5.62)

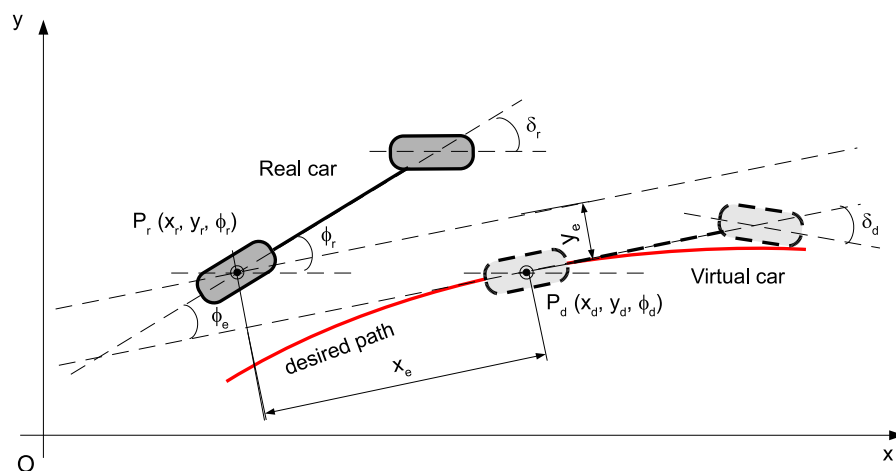


Figure 5.16: Lateral, longitudinal and orientation error (trajectory-tracking)

The error vector for trajectory-tracking is easily obtained from Figs. 5.15 and

5.16,

$$\begin{bmatrix} x_e \\ y_e \\ \phi_e \end{bmatrix} = \begin{bmatrix} \cos\phi_d & \sin\phi_d & 0 \\ -\sin\phi_d & \cos\phi_d & 0 \\ 0 & 0 & 1 \end{bmatrix} \cdot \begin{bmatrix} x_r - x_d \\ y_r - y_d \\ \phi_r - \phi_d \end{bmatrix} \quad (5.63)$$

where (x_d, y_d, ϕ_d) denotes the virtual car pose. The corresponding error derivatives are

$$\begin{cases} \dot{x}_e = -v_d + v_r \cdot \cos\phi_e + y_e \cdot \frac{v_d}{L} \cdot \tan\delta_d \\ \dot{y}_e = v_r \cdot \sin\phi_e - x_e \cdot \frac{v_d}{L} \cdot \tan\delta_d \\ \dot{\phi}_e = \frac{v_r}{L} \cdot \tan\delta_r - \frac{v_d}{L} \cdot \tan\delta_d \end{cases} \quad (5.64)$$

where v_d and δ_d are the linear velocity and desired front wheel angle, respectively.

In this section it is assumed that $|\phi_e| < \pi/2$, which means that the vehicle orientation must not be perpendicular to the desired trajectory.

In trajectory-tracking there are three variables (x_e, y_e, ϕ_e) and just two control variables, which implies that we have only two sliding surfaces. We chose to couple y_e and ϕ_e in one sliding surface.

$$s_1 = \dot{x}_e + k_1 \cdot x_e \quad (5.65)$$

$$s_2 = \dot{y}_e + k_2 \cdot y_e + k_0 \cdot \text{sgn}(y_e) \cdot \phi_e \quad (5.66)$$

where k_0, k_1, k_2 are positive constant parameters, x_e, y_e and θ_e are the trajectory-tracking errors defined in (5.63).

If s_1 converges to zero, trivially x_e converges to zero. If s_2 converges to zero, in steady-state it becomes $\dot{y}_e = -k_2 \cdot y_e - k_0 \cdot \text{sgn}(y_e) \cdot \phi_e$. For $y_e < 0 \Rightarrow \dot{y}_e > 0$ if only if $k_0 < k_2 \cdot |y_e| / |\phi_e|$. For $y_e > 0 \Rightarrow \dot{y}_e < 0$ if only if $k_0 < k_2 \cdot |y_e| / |\phi_e|$. Finally, it can be known from s_2 that convergence of y_e and \dot{y}_e leads to convergence of ϕ_e to zero.

In this section the second reaching law (5.34) was selected. From the time derivative of (5.65) and (5.66) and using (5.34), results

$$\dot{s}_1 = \ddot{x}_e + k_1 \cdot \dot{x}_e = -q_1 \cdot s_1 - p_1 \cdot \text{sgn}(s_1) \quad (5.67)$$

$$\dot{s}_2 = \ddot{y}_e + k_2 \cdot \dot{y}_e + k_0 \cdot \text{sgn}(y_e) \cdot \dot{\phi}_e = -q_2 \cdot s_2 - p_2 \cdot \text{sgn}(s_2) \quad (5.68)$$

From (5.64), (5.67) and (5.68), and after some mathematical manipulation, we

get the commands:

$$\dot{v}_c = \frac{1}{\cos\phi_e} \cdot (-q_1 \cdot s_1 - p_1 \cdot \text{sgn}(s_1) - k_1 \cdot \dot{x}_e - \dot{\omega}_d \cdot y_e - \omega_d \cdot \dot{y}_e + v_r \cdot \dot{\phi}_e \cdot \sin\phi_e + \dot{v}_d) \quad (5.69)$$

$$\delta_c = \arctan\left(\frac{L}{v_r} \cdot \omega_d + \frac{L}{v_r \cdot (v_r \cdot \cos\phi_e + k_0 \cdot \text{sgn}(y_e))} \cdot (-q_2 s_2 - p_2 \text{sgn}(s_2) - k_2 \cdot \dot{y}_e - \dot{v}_r \cdot \sin\phi_e + \dot{\omega}_d \cdot x_e + \omega_d \cdot \dot{x}_e)\right) \quad (5.70)$$

Let us define $V = \frac{1}{2} \cdot s^T \cdot s$ as a Lyapunov function candidate, therefore its time derivative is

$$\begin{aligned} \dot{V} &= s_1 \cdot \dot{s}_1 + s_2 \cdot \dot{s}_2 \\ &= s_1 \cdot (-q_1 \cdot s_1 - p_1 \cdot \text{sgn}(s_1)) + s_2 \cdot (-q_2 \cdot s_2 - p_2 \cdot \text{sgn}(s_2)) \\ &= -s^T \cdot Q \cdot s - p_1 \cdot |s_1| - p_2 \cdot |s_2| \end{aligned}$$

For \dot{V} to be negative semi-definite, it is sufficient to choose q_i and p_i such that $q_i, p_i > 0$.

5.6.1 Simulation Results

In this subsection, simulation results of the proposed method are presented. The simulation model block diagrams are shown in Figs. 5.17 and 5.18. The simulations were made using the trajectory example from Fig. 4.1.

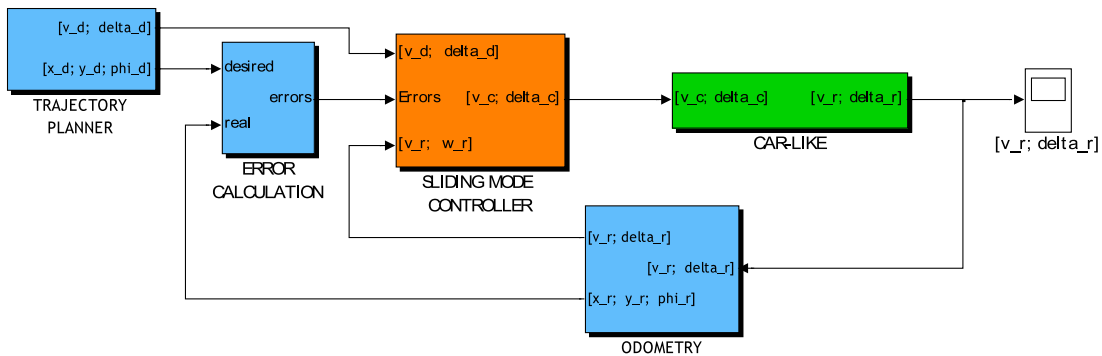


Figure 5.17: Simulation model block diagram (Simulink scheme).

The results shown in Figs. 5.19 - 5.21 are obtained from the simulation in closed-loop using the SM-TT described above. The Trajectory Planner generate the profiles

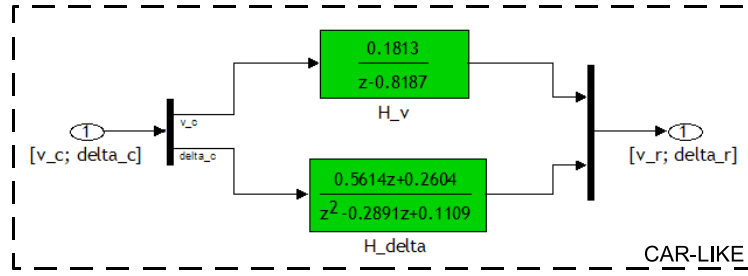


Figure 5.18: Simulink model for car-like vehicle.

of the velocities (linear and angular), see Fig. 4.7, taking account the trajectory example (shown in Fig. 4.1) and the human comfort condition ($a_w < 0.4 \text{ m/s}^2$).

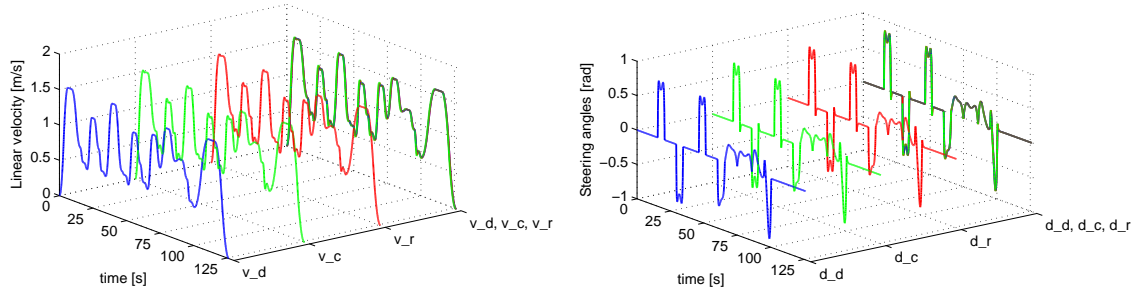


Figure 5.19: Desired (v_d, δ_d) , command (v_c, δ_c) and real (v_r, δ_r) linear velocities and steering angles for SM-TT controller without initial pose error - Path Fig. 4.1

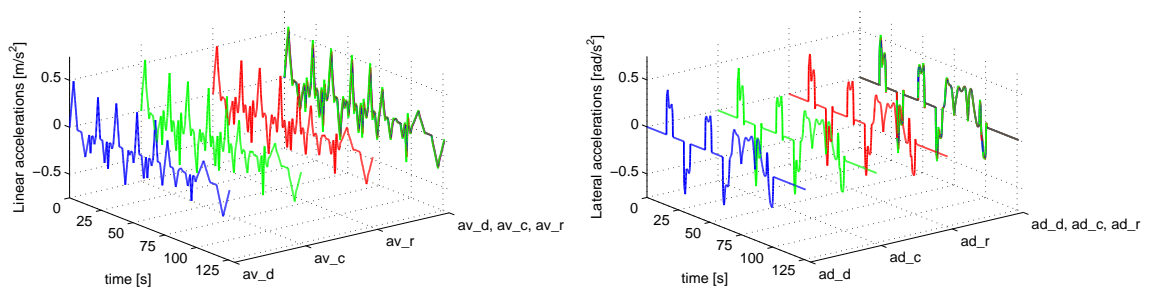


Figure 5.20: Desired $(av_d, a\delta_d)$, command $(av_c, a\delta_c)$ and real $(av_r, a\delta_r)$ longitudinal and lateral accelerations for SM-TT controller without initial pose error - Path Fig. 4.1

From Fig. 5.21 we can observe that position errors (x_e and y_e) and orientation error (ϕ_e) are maintained around zero. Simulation results of the SM-TT controller, for the case with initial pose errors, are shown in Fig. 5.22a. After the initial error conditions, the pose error converges to zero as shown in Fig. 5.22b. The same figure

shows that the robot retrieved quickly ($\Delta t \approx 5$ s) and smoothly from its initial pose error.

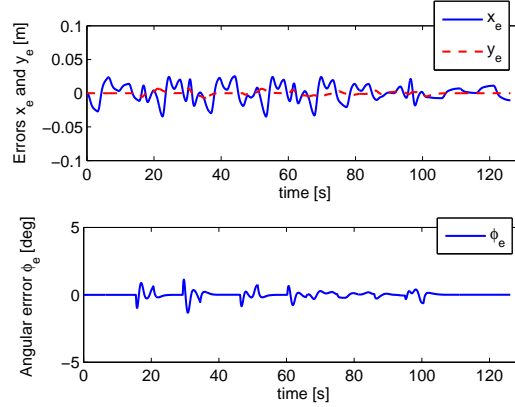


Figure 5.21: Longitudinal (x_e), lateral (y_e) and orientation (ϕ_e) errors for SM-TT controller without initial pose error - Path Fig. 4.1

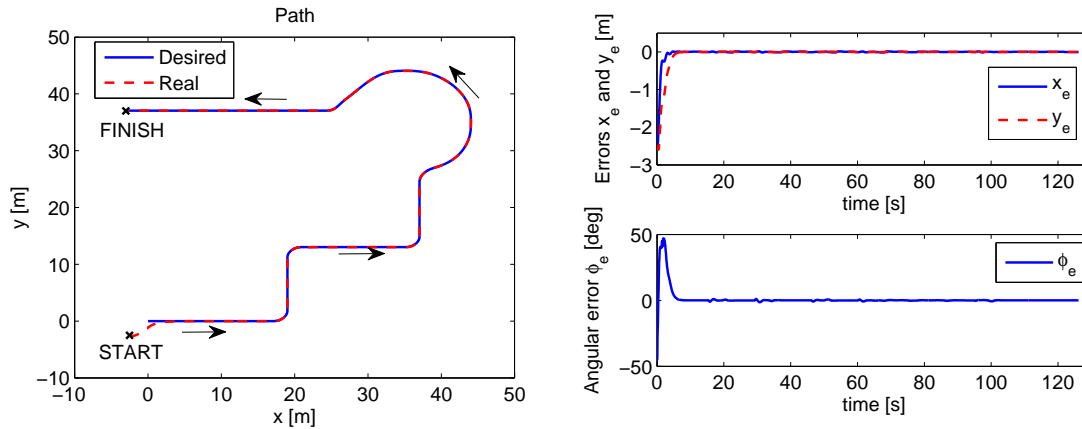


Figure 5.22: Simulation SM-TT control starting from an initial error state ($x_e(0) = -2.5$, $y_e(0) = -2.5$, $\phi_e(0) = \pi/4$).

5.7 Sliding-Mode Path-Following Control for WMR

In path-following, the control objective is to ensure that the robot will correctly follow the reference path. For this purpose, both the lateral error, y_e , and the orientation error, ϕ_e , must be minimized. It is supposed that a feasible desired path for the robot is pre-specified by a trajectory planner.

The main characteristics that must rule PF and that differentiate it from TT, can be summarized as follows: a) In PF the desired trajectory evolution (governed

by time) does not play the same central role as it does in TT. b) Differently to TT (where the desired posture is exactly determined by the time), in PF we must choose some relationship to determine the desired posture. Usually this relationship is called projecting function as it projects the actual posture to the desired path. A classical example of projecting function is the normal projection described in [44] and [52], equivalent to making x_e null. That is, the first error coordinate x_e , is eliminated and the robot posture is expressed by only two: y_e and ϕ_e . c) In PF, if the robot stops, the reference or goal point also stops, as the parameter P_d (see Fig. 3.7) does not move by itself. The progress of P_d must not be independent (as in TT) but dependent on the real robot movement, that is \dot{P}_d equation must be driftless. d) The existence of the rigid law $P_d = P_d(t)$ in TT means pulling or dragging the robot to reach the desired path. On the other hand, in PF the desired path can not pull (or drag) the robot: the robot must move independently by some condition (of course, meanwhile a control law must ensure convergence to the path). We must impose a motion in the real system to guarantee it moves or progresses. In the current mobile robot literature most motion exigencies are applied to WMR robots, so it is usual to have $v_d = constant$ or a velocity profile for v_d is supposed to be given between the initial and final position. e) A direct result of what is explained before is that there is no intrinsic time exigency in the PF. This means that we can not ensure that the robot will reach a desired point in a predictable period of time.

For the path-following without Look-ahead ($Lh = 0$) (see Figure 3.7) the error vector is:

$$\begin{bmatrix} y_e \\ \phi_e \end{bmatrix} = \begin{bmatrix} -\sin\phi_d & \cos\phi_d & 0 \\ 0 & 0 & 1 \end{bmatrix} \cdot \begin{bmatrix} x_r - x_d \\ y_r - y_d \\ \phi_r - \phi_d \end{bmatrix} \quad (5.71)$$

The lateral error y_e is defined as the distance between the vehicle control point (CP) and the closest point along the desired trajectory. The corresponding error derivatives are:

$$\begin{cases} \dot{y}_e = v_r \cdot \sin\phi_e \\ \dot{\phi}_e = \dot{\phi}_r - \dot{\phi}_d = \omega_r - \omega_d \end{cases} \quad (5.72)$$

Defining the control point CP (see Figure 3.8) at a distance $Lh \neq 0$ in front of the robot (called Look-ahead distance), (5.71) becomes:

$$\begin{bmatrix} y_e \\ \phi_e \end{bmatrix} = \begin{bmatrix} -\sin\phi_d & \cos\phi_d & 0 \\ 0 & 0 & 1 \end{bmatrix} \cdot \begin{bmatrix} x_r - x_d + Lh \cdot \cos\phi_r \\ y_r - y_d + Lh \cdot \sin\phi_r \\ \phi_r - \phi_d \end{bmatrix}$$

and

$$\begin{cases} \dot{y}_e = v_r \cdot \sin\phi_e + Lh \cdot \omega_r \cdot \cos\phi_e \\ \dot{\phi}_e = \dot{\phi}_r - \dot{\phi}_d = \omega_r - \omega_d \end{cases} \quad (5.73)$$

In this thesis it is assumed that $|\phi_e| < \pi/2$, which means that the robot orientation must not be perpendicular to the desired trajectory.

By definition of the orthogonal projection x_e and \dot{x}_e , remain equal to zero as the robot moves. Therefore, from the first equation of (5.54) we have:

$$v_d = v_r \cdot \cos\phi_e + \omega_d \cdot y_e \quad (5.74)$$

under the hypothesis that the desired path curvature $k = \frac{\omega_d}{v_d}$ is continuous and bounded, equation (5.74) can be rewritten as:

$$v_d = \left(\frac{\cos\phi_e}{1 - k \cdot y_e} \right) \cdot v_r \quad (5.75)$$

under the constraint: $(1 - k \cdot y_e) > 0$. A velocity profile for v_r is supposed to be given between the initial and final position where $v_r = 0$ (when $v_r = 0$, $\omega_r = 0$ as well).

Let us define the sliding surface

$$s = \dot{y}_e + k_2 \cdot y_e + k_0 \cdot \text{sgn}(y_e) \cdot \phi_e \quad (5.76)$$

whose time derivative is:

$$\dot{s} = v_r \cdot \dot{\phi}_e \cdot \cos\phi_e + k_2 \cdot v_r \cdot \sin\phi_e + k_0 \cdot \text{sgn}(y_e) \cdot \dot{\phi}_e \quad (5.77)$$

From (5.34), (5.77) and knowing that

$$\dot{\phi}_e = \dot{\phi}_r - \dot{\phi}_d = \omega_r - \omega_d$$

one gets the steering command

$$\omega_c = \frac{-q_2 \cdot s - p_2 \cdot \text{sgn}(s) - k_2 \cdot v_r \cdot \sin\phi_e}{v_r \cdot \cos\phi_e + k_0 \cdot \text{sgn}(y_e)} + \omega_d \quad (5.78)$$

where

$$\omega_d = k \cdot \left(\frac{\cos\phi_e}{1 - k \cdot y_e} \right) \cdot v_r \quad (5.79)$$

For the case of using look-ahead Lh :

$$\begin{aligned} \dot{\omega}_c = & \frac{1}{Lh \cdot \cos\phi_e} \cdot (-q_2 \cdot s - p_2 \cdot \text{sgn}(s) - k_2 \cdot \dot{y}_e - \\ & - v_r \cdot \dot{\phi}_e \cdot \cos\phi_e + Lh \cdot \dot{\phi}_e^2 \cdot \sin\phi_e - k_0 \text{sgn}(y_e) \cdot \dot{\phi}_e) + \dot{\omega}_d \end{aligned} \quad (5.80)$$

Let us define $V = \frac{1}{2} \cdot s^2$ as a Lyapunov function candidate, therefore its time derivative is

$$\begin{aligned} \dot{V} &= s \cdot \dot{s} \\ &= s \cdot (\ddot{y}_e + k_2 \cdot \dot{y}_e + k_0 \cdot \text{sgn}(y_e) \cdot \dot{\phi}_e) \\ &= s \cdot (-q_2 \cdot s - p_2 \cdot \text{sgn}(s)) \\ &= -q_2 \cdot s^2 - p_2 \cdot \frac{s^2}{|s|} \end{aligned}$$

For \dot{V} to be negative semi-definite, it is sufficient to choose q_2 and p_2 such that $q_2, p_2 > 0$.

For the longitudinal velocity we may have different situations namely: 1) $v_c = \text{constant}$; 2) $v_c = v_d$; 3) v_c given by a longitudinal controller, which has as input the velocity error ($v_d - v_r$), and possibly robot acceleration data. In practical applications, the desired velocity v_d needs to be calculated online such that its values are in accordance to the associated path. This requires that the feedback information of the pose and velocity of the robot be inputs of the path planner.

5.7.1 Simulation Results

In this subsection, simulation results of the SM-PF proposed controller are presented. The simulation model block diagram is shown in Fig. 5.23.

Figures 5.24 and 5.27 show the simulation results using SM-PF control in case of Path presented in Fig. 5.6b. In the first figure is presented the situation when $v_c = v_d$, where v_d is equal to linear velocity from Fig. 5.7a and the second show the case when $v_c = \text{constant} = 0.5 \text{ m/s}$.

In case of SM-PF control only the lateral error, y_e , and the orientation error, ϕ_e , must be minimized. From Figs. 5.26 and 5.29 we can observe that the errors (y_e and ϕ_e) are maintained around zero.

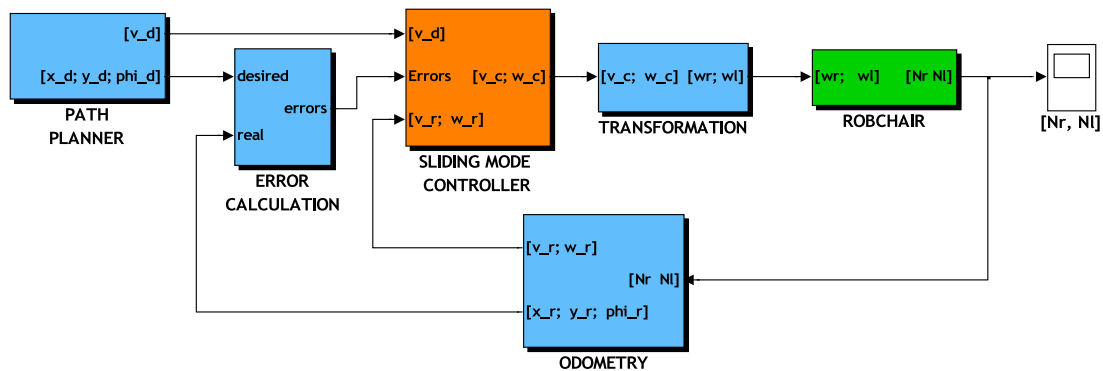


Figure 5.23: Simulation model block diagram for TT-PF control - Simulink scheme.

For $v_c = \text{constant}$ there is a tendency of increasing for the lateral and orientation errors. When we used $v_c = v_d$ the robot velocity is a lower inside of a curve (according with the algorithm presented in Chapter 4). In the other way, when we used $v_c = \text{constat}$ the robot velocity is equal along of all the path meaning that in curve the robot goes outside the desired path (the lateral and orientation errors increase). For this reason it is very important to chose the velocity profiles along the path.

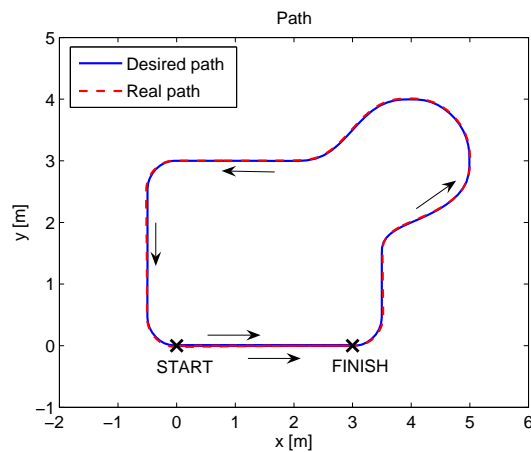


Figure 5.24: Simulation of TT-PF controller with a given longitudinal velocity profile.

From Fig. 5.21 we can observe that position errors (x_e and y_e) and orientation error (ϕ_e) are maintained around zero.

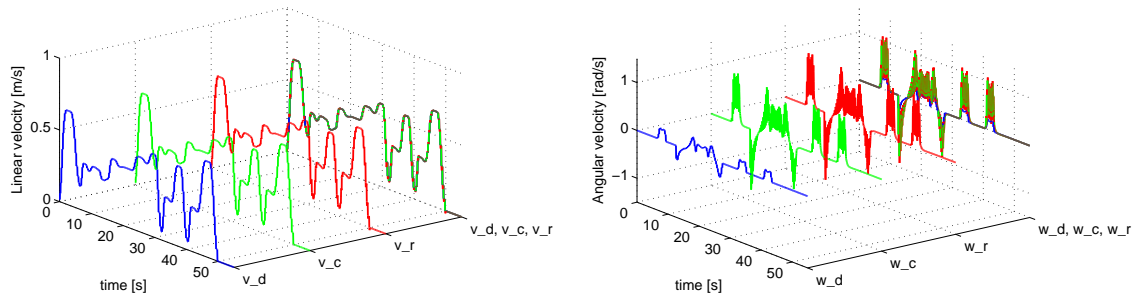


Figure 5.25: Desired ω_d , command ω_c and real ω_r longitudinal and angular velocity for SM-PF control.

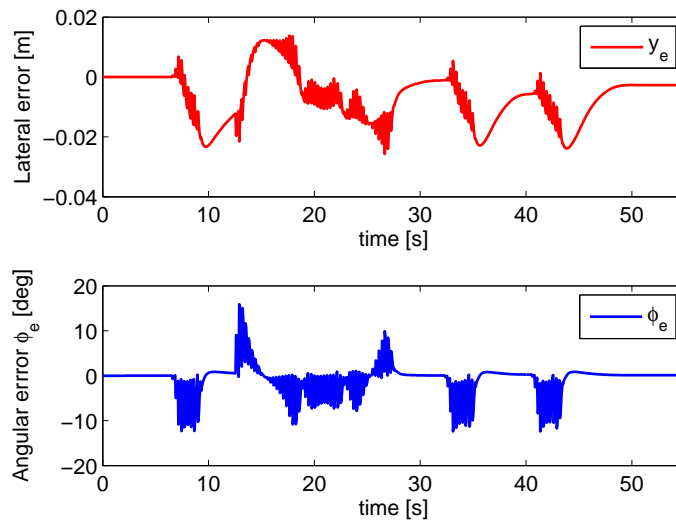


Figure 5.26: Lateral and angular errors of SM-PF control.

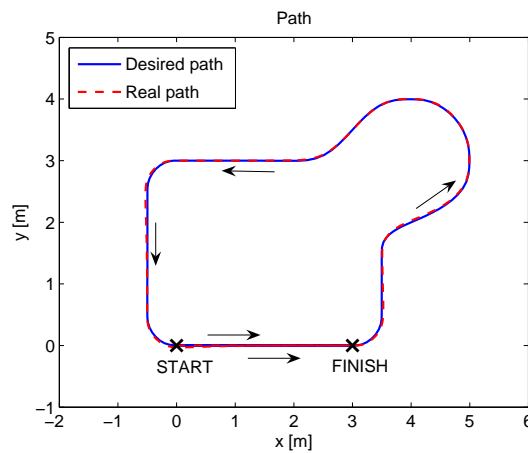


Figure 5.27: Simulation of TT-PF controller with a constant longitudinal velocity ($v_d = 0.5\text{m/s}$).

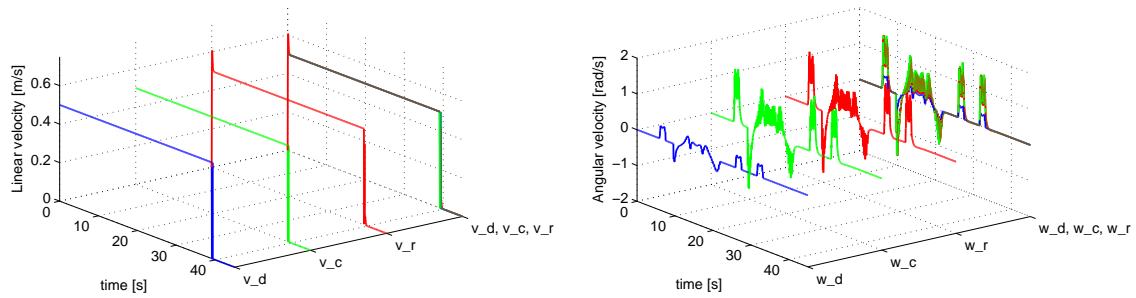


Figure 5.28: Desired $a\omega_d$, command $a\omega_c$ and real $a\omega_r$ longitudinal and angular velocity for SM-PF control.

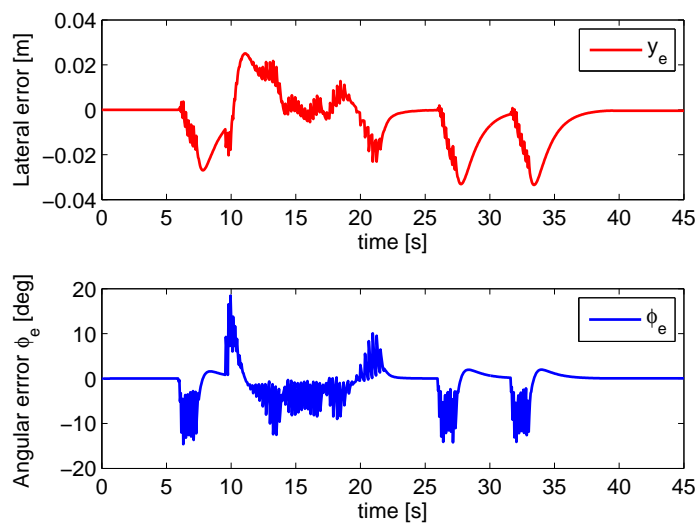


Figure 5.29: Lateral and angular errors of SM-PF control.

Chapter 6

Human Body Comfort

6.1 Introduction

Many people nowadays spend a significant proportion of their time travelling and there is an increasing demand for comfort, in private and public transportation. Three classes of factors are considered in the analysis of travelling comfort: organizational, local and riding. The riding comfort can be analysed in three different respects: dynamic factors - related to vibration, shocks and acceleration; ambient factors - thermal comfort, air quality, noise, pressure gradients, etc; spatial factors - dealing with the ergonomics of the passenger's position.

In today's aged society, a wheelchair is the most common vehicle to assist elderly and disabled people. Wheelchairs can provide many profits to users, such as extending mobility, enlarging community and social activities, and enhancing quality of life of the users. Therefore, the number of users of electric powered wheelchairs is increasing, and the development of wheelchairs which are able to drive comfortably is highly required.

Various factors are largely related to the riding comfort of electric powered wheelchairs, such as seat comfort, ambient noise, and stability. The passenger's posture swing of body and the driving acceleration and deceleration are generally the main factors which influence comfort.

In the international standard of ISO-2631-1 [133], the riding comfort of a transportation vehicle is evaluated by the magnitude of the acceleration weighted by oscillation frequency.

Passenger's comfort while riding wheelchairs is also improved by suppressing the vibration with discomfort frequencies. Maeda [113] described that a wheelchair with

user has three resonant frequencies; the first resonant frequency is $5\div 7$ [Hz], the second is 8[Hz], and third is $13\div 15$ [Hz]. And he addressed that the main point for improving a wheelchair passenger's comfort was to reduce the seat vibration of the wheelchair at around 8[Hz].

On the other hand, a wheelchair is not the only steady-state operation, but also the transient state such as starting and stopping. Additionally, the high drive acceleration or deceleration causes passenger's discomfort. However, up to the present, passenger's posture behavior of body which causes discomfort during riding has not been studied to our knowledge.

Static ride comfort deals with the user's response to prolonged sitting with minimal movement. For example, in an office setting, the user is primarily stationary for most of the work day. Static loads affect the user continually in each position she or he acquires. Posture and postural support are therefore extremely important factors when considering rider comfort. The spinal column supports the upper extremities and compresses under these loads. In addition, these compressive loads induce moments, and these moments increase as postural deviation increases. These moments can cause spinal deformities. Seat supports can reduce and redistribute pressure as well as minimize postural deviation.

Dynamic wheelchair applications incorporate accelerations and cyclic loading compounding the existing static loads, for example, the wheelchair motion as the result of user's propulsion. During an acceleration, the spinal column acts as a shock absorber, an energy absorber.

A user of a power wheelchair must learn to maneuver the chair using the control interface selected for his or her individual needs. This may be a joystick, sip-and-puff, tongue touch pad, eye gaze, or chin or head control, depending upon the level of disability. Research has found that in individuals with severe disabilities resulting from high-level spinal cord injury, nervous system diseases, cognitive impairment or blindness, 10% find it extremely difficult to perform activities of daily living with power wheelchairs, and up to 40% find many steering and maneuvering situations difficult or impossible. New technology using microprocessors and sensors to assist navigation help to alleviate this problem.

The ISO 2631 defines methods for quantification, evaluation and analysis on human response to whole-body vibrations concerning different aspects:

- Health risk;

- Comfort and perception;
- Motion sickness.

Comfort is a complex definition that contains both physiological and psychological components; this includes the subjective feeling of well being with the absence of discomfort, stress and pain. Comfort not only consists of the absence of negative effects; it is also the experience of positive aspects of comfort. Therefore, comfort includes a form of evaluation, i.e. *it feels well* and has as its opposite, negative sensations. From interviews of vehicle passengers it is obvious that ride comfort is dependent not only on the magnitude but also on the occurrence of occasional shocks or transients.

Ride quality is a person's reaction to a set of physical conditions in a vehicle environment, such as dynamic, ambient and spatial variables. Dynamic variables consist of motions, measured as accelerations and changes (jerk) in accelerations in all three axes (lateral, longitudinal and vertical), angular motions about these axes (roll, pitch and yaw) and sudden motions, such as shocks and jolts. Normally, the axes are fixed to the vehicle body. The ambient variables may include temperature, pressure, air quality and ventilation, as well as noise and high frequency vibrations, while the spatial variables may include workspace, leg room and other seating variables. However, many use the term passenger comfort, ride comfort or average ride comfort for ratings on a ride quality scale regarding the influence of dynamic variables. Normally, higher rating on a ride quality scale means better comfort, whereas higher rating on a ride (dis-)comfort scale means less comfort.

The human evaluation of comfort, ride quality, involves not only motion quantities but also human interaction variables (see Figure 6.1).

In the time domain an analysis points out parameters like: peak value, standard deviation, root mean square value (rms), running rms, crest factor, energy equivalent rms, estimated Vibration Dose Value (eVDV), root-mean-quad (rmq) or Vibration Dose Value (VDV). The evaluations and weightings in the frequency domain can be realized via a Fast Fourier Transformation (FFT) or in the power spectrum. The most important parameters are summarized in Table 6.1

The evaluation of vibration is defined by the specification of the rms value of the acceleration a in $[m/s^2]$ for translational and for rotational vibrations in $[rad/s^2]$:

$$a_q = \left[\frac{1}{T} \cdot \int_0^T a_q^2(t) dt \right]^{\frac{1}{2}} \quad (6.1)$$

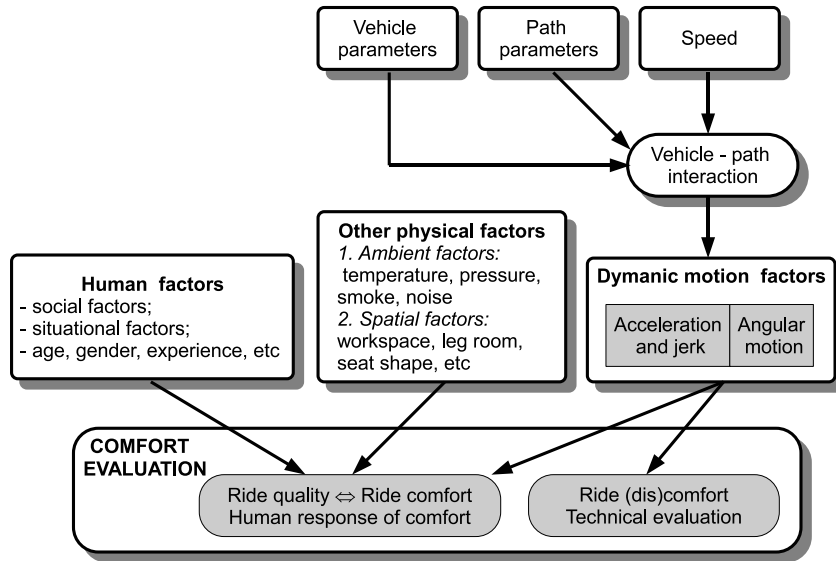


Figure 6.1: The human response (ride quality) involves human variables as well as dynamic motion and other physical variables, but the ride comfort response and technical evaluation of ride (dis-)comfort involves dynamic motion variables only. Modified from Forstberg [114].

Table 6.1: Most relevant parameters

Parameter	Definition
mean	$\bar{x} = \frac{1}{N} \sum (x(i))$
standard deviation	$\tau = \left[\frac{1}{N} \sum [x(i) - \bar{x}]^2 \right]^{\frac{1}{2}}$
root-mean-square	$rms = \left[\frac{1}{N} \sum x^2(i) \right]^{\frac{1}{2}}$
crest factor	$\frac{peakvalue}{rms}$
root-mean-quad value	$r.m.q = \left[\frac{1}{N} \sum x^4(i) \right]^{\frac{1}{4}}$
Vibration Dose Value	$V DV = \left[\frac{T_s}{N} \sum x^4(i) \right]^{\frac{1}{4}}$
estimated Vibration Dose Value	$eV DV = \left[(1.4 \cdot (rms))^4 \cdot T_s \right]^{\frac{1}{4}}$

with

q – weighting factor for different conditions

$a_q^2(t)$ – instantaneous frequency-weighted acceleration as a function of time, t

T – integration time for running averaging

The overall weighted acceleration a_w shall be determined in accordance with the

following equation (6.2) or its digital equivalent in the time or frequency domain:

$$a_q = \left[\sum_i (W_i \cdot a_i)^2 \right]^{\frac{1}{2}} \quad (6.2)$$

with W_i is frequency weighting factor and a_i is rms acceleration.

If the signal includes components in more than one direction, the total value a_w of the weighted rms accelerations is calculated as follows:

$$a_w = \sqrt{k_x^2 \cdot a_{wx}^2 + k_y^2 \cdot a_{wy}^2 + k_z^2 \cdot a_{wz}^2} \quad (6.3)$$

with

a_{wx}, a_{wy}, a_{wz} = weighted rms accelerations with respect to the orthogonal axes x, y or z respectively

k_x^2, k_y^2, k_z^2 = multiplying factors for special axes

For a seated person $k_x = 1.4, k_y = 1.4$ and $k_z = 1$.

The Vibration Dose Value (VDV), sometimes called fourth-power vibration dose, which is more sensitive for peak values, is used if high peak values occur in the vibration signal (like shock conditions):

$$VDV = \left[\int_0^T a_w^4(t) dt \right]^{\frac{1}{4}} \quad (6.4)$$

The VDV is a method of assessing the cumulative effects (i.e. dose) of vibrations. If the crest factor is low, the estimated Vibration Dose Value (eVDV) is sometimes used to calculate the approximate vibration dose value from the rms of the weighted accelerations (a_{rms}) and the exposure time t in seconds:

$$eVDV = 1.4 \cdot a_{rms} \cdot t^{\frac{1}{4}} \quad (6.5)$$

Approximate magnitudes of overall (rms) vibration total values (a_w in $[m/s^2]$) in public transport are given in Table 6.2. Vibration total value is calculated as the square root of the sum of the squares of each axis measurement (see eq. 6.3).

According to the EU Directive on mechanical vibration [115] the average limit value of VDV is $9.1ms^{-1.75}$ and the upper limit is $21ms^{-1.75}$.

Table 6.2: ISO 2631-1 STANDARD.

Overall Acceleration	Consequence
$a_w < 0.315m/s^2$	not uncomfortable
$0.315 < a_w < 0.63m/s^2$	a little uncomfortable
$0.5 < a_w < 1m/s^2$	fairly uncomfortable
$0.8 < a_w < 1.6m/s^2$	uncomfortable
$1.25 < a_w < 2.5m/s^2$	very uncomfortable
$a_w > 2.0m/s^2$	extremely uncomfortable

The transmissibility (T_r) is defined as the output VDV divided by the input VDV ,

$$T_r = \frac{VDV_{output}}{VDV_{input}} \quad (6.6)$$

The transmissibility defines the performance of the wheelchair in terms of the amplification or attenuation of the vibration that is transmitted to the occupant. A value less than unity indicates that the accelerations were attenuated by the combination of wheelchair and human, whereas a value great than unity indicates an amplification of accelerations by the wheelchair-human system.

In Frequency-domain, power spectral density function (PSD) shows the strength of the variations(energy) as a function of frequency. In other words, it shows at which frequencies variations are strong and at which frequencies variations are weak. The unit of PSD is energy per frequency(width) and you can obtain energy within a specific frequency range by integrating PSD within that frequency range. Computation of PSD is done directly by the method called FFT or computing autocorrelation function and then transforming it.

Given the input, acceleration from inertial sensor, and the output, acceleration obtained from the HNC model, the transfer function is usually calculated using the cross-spectral density (CSD) method defined as:

$$H_{CSD}(f) = \frac{CSD_{input-output}(f)}{PSD_{input}(f)} \quad (6.7)$$

where $CSD_{input-output}(f)$ is the CSD of the input and output, and $PSD_{input}(f)$ is the power spectral density of the input. The advantage of using the CSD method is that the function generates the phase of the response and only includes data at the input and output that are correlated, thus reducing the effects of noise in the measurement system.

6.2 Model of Human Head-Neck Complex

The human body is a complex dynamic system, the properties of which vary from moment to moment and from one individual to another. From the results of large amount of experimental data, various biomechanical models have been developed to describe the human motion. These models can be grouped as lumped or distributed parameter models. The lumped parameter models consider the human body as several rigid bodies, springs and dampers [116], [117], [118]. Some distributed models consider the spine as a layered structure of rigid elements, representing the vertebral bodies and deformable elements representing the intervertebral disc by the finite elements [119].

The dynamic response of seated subjects exposed to vibration has been widely assessed in terms of the driving point impedance, apparent mass and transmissibility (transmission of motion through the human body). The transmission of the acceleration to the head-neck complex (HNC) in the seated human body may be the cause of discomfort and motion sickness in wheelchairs. The seating back, by limiting the horizontal and rotational motion of the trunk, increases the transmission of the trunk horizontal acceleration to the HNC. This may have considerable influence on discomfort.

The present study focuses specifically on the influence of sliding-mode trajectory-tracking (SM-TT) controller action on user comfort. The user comfort is examined not only in the time domain (using the transmissibility parameter), but also in the frequency domain. For measuring accelerations of the wheelchair, a three-dimensional inertial sensor was used. The analysis of user comfort is made in three different situations: i) SM-TT control under odometry navigation; ii) when the odometric data is fused with absolute position data from magnetic markers (using an EKF-based fusion in the on-line pose estimation); iii) SM-TT control with purposely-incorrectly-tuned parameters.

A double-inverted pendulum model with two degrees-of-freedom is considered for the HNC model (Fig. 6.2). One of the centers of rotation of the model was assumed to be at C7-T1 (O_1 in Fig. 6.2), and the other at C0-C1 (O_2 in Fig. 6.2) of the cervical spine. Two lumped masses, indicating the mass of the neck and the mass of the head, were considered in the model. The center of mass of the neck was assumed to be exactly at the mid-point of the two centers of rotation. Moreover, the center of mass of the head was assumed to be exactly over the center of mass of the neck and the

center of rotation (Fig. 6.2). The equation of motion using generalized coordinates can be expressed as:

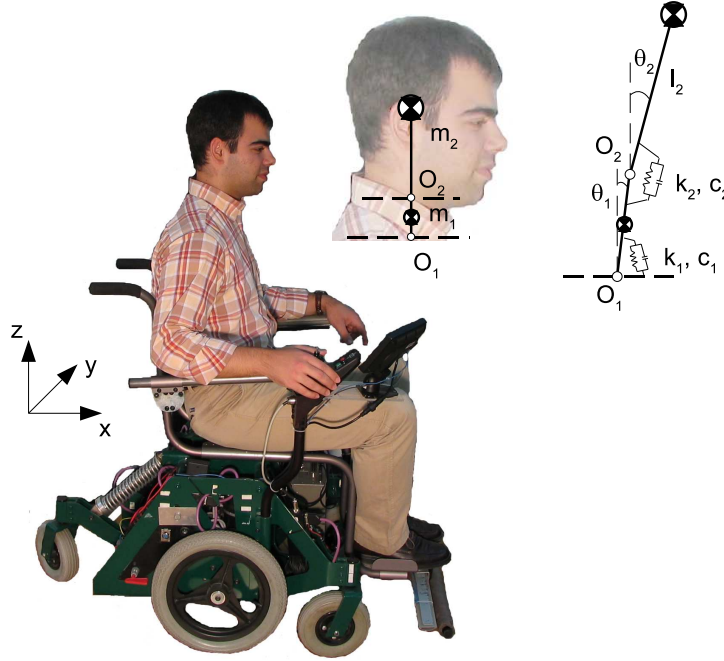


Figure 6.2: Human head-neck model

$$M(q)\ddot{q} + C(q, \dot{q})\dot{q} + Kq + G(q) = Q_q \quad (6.8)$$

where: $q = \begin{bmatrix} \theta_1 \\ \theta_2 \end{bmatrix}$, $Q_q = 0$,

$$M(q) = \begin{bmatrix} M_{11} & M_{12} \\ M_{21} & M_{22} \end{bmatrix}$$

$$M_{11} = m_1 l_1^2 + m_2 L_1^2 + J_1$$

$$M_{12} = m_2 L_1 l_2 \cos(\theta_1 - \theta_2)$$

$$M_{21} = m_2 L_1 l_2 \cos(\theta_1 - \theta_2)$$

$$M_{22} = m_2 l_2^2 + J_2$$

$$C(q, \dot{q}) = \begin{bmatrix} c_1 + c_2 & C_{12} \\ C_{21} & c_2 \end{bmatrix}$$

$$C_{12} = m_2 L_1 l_2 \sin(\theta_1 - \theta_2) \dot{\theta}_2 - c_2,$$

$$C_{21} = -m_2 L_1 l_2 \sin(\theta_1 - \theta_2) \dot{\theta}_1 - c_2,$$

$$K = \begin{bmatrix} k_1 + k_2 & -k_2 \\ -k_2 & k_2 \end{bmatrix}$$

Table 6.3: Characteristics of user's elements

Element	Neck	Head
Length of segment $L_i[m]$	0.080	0.138
Center of gravity $l_i[m]$	0.040	0.069
Mass $m_i[kg]$	1.01	4.22
Moment of Inertia $J_i[kgm^2]$	0.0011	0.210
Spring constant $k_i[Nm/rad]$	14.04	10.29
Damping constant $c_i[Nms/rad]$	0.347	0.230

$$G(q) = \begin{bmatrix} -(m_2L_1 + m_1l_1)\ddot{x}\cos(\theta_1) \\ -m_2l_2\ddot{x}\cos(\theta_2) \end{bmatrix}$$

In my thesis, the user characteristic elements, shown in Table 6.3 (from [116]), were used to model the dynamic behavior of the human HNC.

6.3 Experimental Date From Inertial Sensor

The analysis of user comfort is made in three different situations:

- case A: SM-TT control under odometry navigation;
- case B: SM-TT control under magnetic-markers navigation (odometric data is fused, using an EKF-based fusion, with absolute position data from magnetic markers detection);
- case C: SM-TT control with purposely-incorrectly-tuned parameters.

The experimental data of all three cases are summarized in Table 6.4. Three experimental trials were executed in cases *A* and *B*. The table shows the vibration dose value (*VDV*), transmissibility (T_r), root mean square accelerations (*rms*) and maximum values (*Max*). The results of columns "rms accel. Robchair" and "Max. accel. RobChair" concern the acceleration results obtained by the inertial sensor; and the "rms accel. Head" and "Max. accel. Head" were obtained from the model of head-neck complex (6.8). The overall rms acceleration of head (along the *x* axes) in cases *A* and *B* are in range of "not uncomfortable", but in case *C* is in range of "uncomfortable" (see Table 6.2 and equation (6.3)).

Each experiment was made for the same trajectory (see Fig. 6.3). The time domain *VDV* values obtained in cases *A* and *B* are below the limit value of $9.1ms^{-1.75}$, only in case *C*, *VDV* values are above that limit. As can be observed from Table

Table 6.4: Experimental results.

Case	No	VDV_x	VDV_x	T_r	rms accel.	Max. accel	rms accel.	Max. accel
		RobChair	Head		RobChair	RobChair	Head	Head
A	I	2.9219	1.3826	0.4732	0.3287	1.5686	0.1656	0.7286
	II	2.7634	1.3429	0.4859	0.3191	1.4988	0.1589	0.7307
	III	2.7177	1.2802	0.4710	0.3187	1.5590	0.1510	0.8210
aver.		2.8010	1.3352	0.4767	0.3222	1.5421	0.1585	0.7601
B	I	2.9481	1.4408	0.4887	0.3538	1.2853	0.1797	0.7100
	II	3.2946	1.5707	0.4767	0.3663	1.7635	0.1856	0.7988
	III	3.0318	1.4860	0.4901	0.3629	1.4136	0.1828	0.7755
aver.		3.0915	1.4992	0.4852	0.3610	1.4875	0.1827	0.7614
C	-	11.4623	5.4607	0.4764	1.5185	4.1708	0.7039	2.2210

6.4, the transmissibility tends to be under unity, suggesting that the vibrations are attenuated.

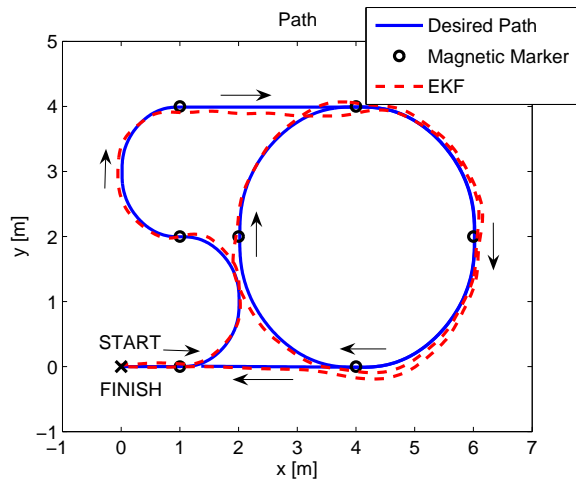


Figure 6.3: Experimental sliding-mode trajectory-tracking control using an EKF-based fusion in the on-line pose estimation.

Figure 6.4 shows cross-spectral density values for all experiments. The maximum of H_{CSD} magnitude occurs in case *C*, and the corresponding frequencies are between $0.8 - 1.8Hz$. When the magnitude of H_{CSD} increases, the user comfort decreases.

Figure 6.5 shows experimental acceleration data from IMU and from encoders (first derivative of velocity) for SM-TT control under magnetic-markers navigation.

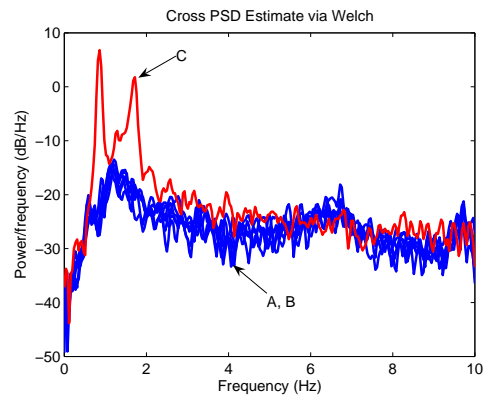


Figure 6.4: Cross-spectral density functions for all experiments.

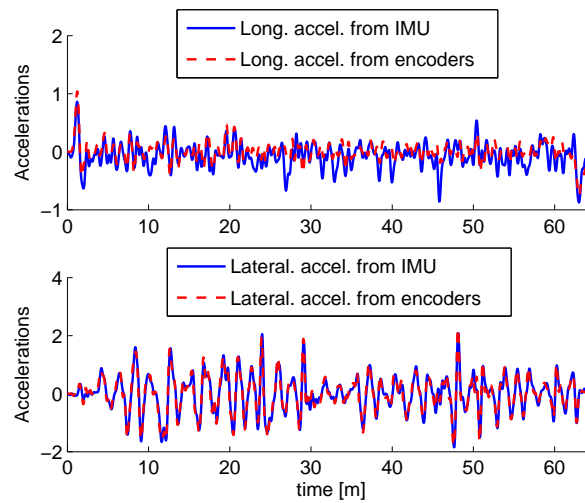


Figure 6.5: Longitudinal and lateral accelerations from IMU and from encoders.

Chapter 7

Implementation in Real Wheelchair - RobChair

7.1 Introduction

In last two decades an accelerated progress in modern wheelchairs has occurred. They are lighter and perform better than ever before. There are now many possibilities available to improve the ride, from suspension systems which help to remove vibrations and jolts, to ultra-light weight frames which enable better performance, to special designs for every individualized need.

There has been an increasing need for wheelchairs over time. In [120] they state: *Mobility is fundamental to health, social integration and individual well-being of the human being. Henceforth, mobility must be viewed as being essential to the outcome of the rehabilitation process of wheelchair dependent persons and to the successful (re-)integration into society and to a productive and active life. Many lower limb disabled subjects depend upon a wheelchair for their mobility. Estimated numbers for the Netherlands, Europe and USA are respectively 80.000, 2,5 million and 1,25 million wheelchair dependent individuals. Groups large enough to allow a special research focus and conference activity. Both the quality of the wheelchair, the individual work capacity, the functionality of the wheelchair/user combination, and the effectiveness of the rehabilitation programme do indeed determine the freedom of mobility. Their optimization is highly dependent upon a continuous and high quality research effort, in combination with regular discussion and dissemination with practitioners...*

Various research projects on intelligent wheelchairs have been reported in the last decade, such as RobChair [121]-[122], Wheelesley [123], NavChair [124], the TAO

projects [125], SIAMO [126], Rolland [127]-[128], MAid [129]. However, all of these projects only represent the outgrowths of mobile robot research and few have made the transition to a commercial product.

The majority of research projects developing intelligent wheelchair sensors, control and technology have concentrated upon improving the autonomous function of the mobility aid.

A key task is to provide controls and control modes so that disabled users can make the most efficient use of their skills and abilities. Techniques developed in the field of robotics have the potential to offer independent mobility to people who cannot operate existing controls, and also to reduce the need to tailor these relatively complex controls and control modes precisely to maximise the user's skills.

Intelligent wheelchair systems have to be developed under a different set of goals from other mobile robots. Safety is a key factor for a wheelchair whose task is to carry a human user. In addition, the wheelchair's motion must be smooth, so that the user would feel safe, and comfortable. As the wheelchair operates in a dynamic environment, the path guidance should also be able to deal with unexpected events such as dangers or unexpected obstacles on the path.

The intelligent wheelchair, RobChair system, is being developed to overcome above mentioned problems, allowing the end-user to just perform safe movements and accomplish some daily life important tasks. The RobChair is a highly interactive system which is jointly controlled by the human operator and the software of the robot.

A robotic wheelchair must interact with its user, and for a human-machine symbiosis shared control capabilities is required.

The wheelchair must be able to accept inputs from its user not only at the start of the trip, but throughout the journey. Our wheelchair system will be able to navigate in indoor and outdoor environments respecting human comfort.

Little is known about how dynamic acceleration affects wheelchair-ride comfort. Most current literature focuses on the vibration exposure of a seated occupant [130, 131, 132]. Some standards have been developed by the International Organization for Standardization (ISO) to quantify how much exposure is allowable for various frequencies of exposure [133]. Although the exposure to whole-body vibration has been shown to be injurious to seated humans, the effects of wheelchairs and seating systems on the transmission of vibration to an individual have not been thoroughly examined.

This thesis studies the driving control of powered wheelchairs with smooth trajectory and good ride quality, and proposes a trajectory control scheme based on sliding mode.

7.2 Architecture of RobChair

In this section, a navigation architecture capable of providing intelligent motion control of autonomous vehicles is briefly described, which is under research at Institute of Systems and Robotics (ISR) Coimbra and tested in RobChair platform (Fig. 7.1). This architecture is structured in three levels: Motion Planning Level (MPL), Motion Tracking Level (MTL) and Motion Control Level (MCL) (see Fig. 7.2).

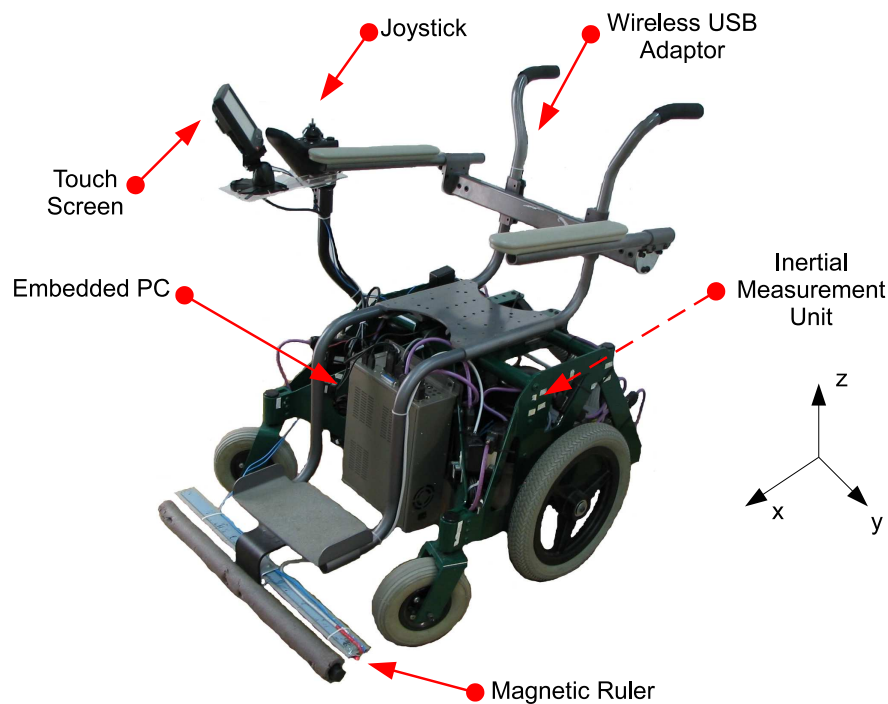


Figure 7.1: RobChair platform.

Motion Planning Level (MPL) - is responsible for feeding the local motion planning level with a path of predefined goal, which may be provided by Human-Machine Interface (HMI) or centralized task controller through local network.

Motion Tracking Level (MTL) - determines the linear and angular velocity commands to be sent to the Motion Controller, based on the error between the reference trajectory provided by the upper levels and the real trajectory.

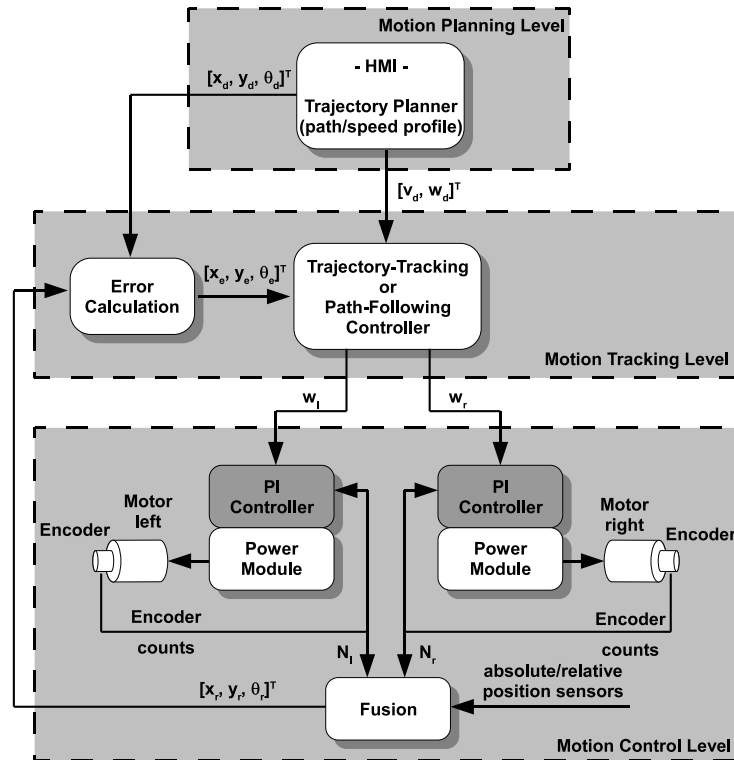


Figure 7.2: Levels and modules of the motion control system.

Motion Control Level (MCL) - is responsible for the robust velocity servo-control. This block uses the encoders' data in two separated feedback control loops that drives the wheels to their reference velocities. A traction control module receives the desired velocity vector from the MTL module and gives the command to the power modules of each motors.

7.2.1 Hardware and Software Architecture

The RobChair (Fig. 7.1) is powered by two 12V batteries which feed two permanent magnet DC motors with 24V input voltage and 1000 RPMS. These motors are coupled to two gearboxes with a factor 1:10. With the aid of this gearboxes, each wheel may have a nominal torque of 29,3 Nm. The RobChair has been equipped with several devices such as two power driver modules, optical encoders, lasers, inertial sensor and magnetic ruler.

The control architecture is depicted in Fig. 7.3. The following devices are connected, through CAN-bus (controller-area network), to the embedded PC: two motor nodes; two encoder nodes; one joystick node; one CAN Trigger node; one magnetic

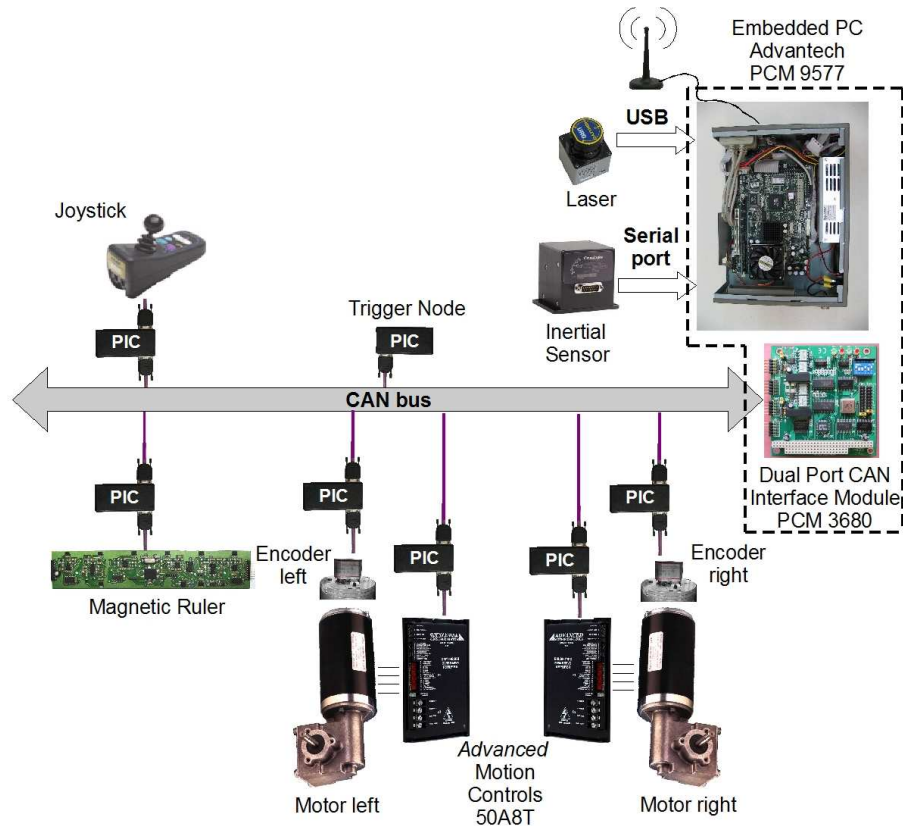


Figure 7.3: RobChair CAN-based hardware architecture.

ruler.

The onboard embedded PC, is a Linux-based system connected to external computational systems via wireless Ethernet.

The real-time software framework is composed of a real-time operating system, a robotic hardware abstraction layer and a component-based software system. The current implementation of the framework is based on RTAI Linux as its underlying real-time operating system. RTAI Linux is a real-time extension to the regular Linux kernel, and has been selected because it provides the usual advantages of the Linux operating system, along with hard-real time capabilities. This choice limits the programming language to C, to allow for component execution in kernel space when hard real-time is required, but extensions to other programming languages are possible for non real-time components.

The component-based software selected for the proposed software framework is GenoM (**generator of modules**) [134], [135], which is an environment for description and implementation of software components that provides the following:

- defines specific interaction between components and composition standards;

- provides the dedicated set of executable software elements required to support the execution of software components that conform to the model;
- defines the internal architecture of software components, and their structure and functioning;
- provides a set of tools for describing software components and for generating templates.

As depicted in Fig. 7.3, the CAN fieldbus is used to link the central unit with several implemented nodes. The communication is done by a home defined protocol with which the communication events are synchronized by a trigger (called CAN-trigger). At every 5 ms, the CAN-trigger sends a command message allowing the other controllers to perform synchronized data acquisition and actuation. The control loop time of the high-level algorithms that are running in the embedded PC is different from the low-level control loop. Currently it is settled at 50 ms. Each motor has its own dedicated controller that performs encoder data acquisition, odometry computation, and wheel velocity control.

The RobChair is equipped with a magnetic sensing ruler (MSR) developed at ISR-UC that is able to perform a robust detection of magnetic markers [136]. The experimental results with RobChair primarily show that the detection system is robust, since it is able to detect true magnetic markers, and to eliminate noisy magnetic distortions and false markers.

The odometric data calculated based on the wheel encoders is fused with the data from magnetic markers. The extended Kalman filter (EKF) was chosen for the fusion process, as summarized in Table 7.1. The robot pose defined by the Cartesian coordinates (x_r, y_r) and heading (ϕ_r) are the state variables of the EKF. The magnetic ruler measures are treated as measurements in the fusion process. For a detailed description of the fusion algorithm see [136]. This navigation technology, based on sensing magnetic markers, is well suited when high precision navigation and robustness is required, and it can be used to complement other navigation systems, such as GPS.

The inertial sensor RGA300CA-100 (Crossbow) was used for measuring the wheelchair accelerations in three orthogonal directions.

Table 7.1: Fusion algorithm.

Models

A. System model:

$$\begin{bmatrix} x_r(k+1) \\ y_r(k+1) \\ \phi_r(k+1) \end{bmatrix} = \begin{bmatrix} x_r(k) + v_r(k) \cdot \cos(\phi_r(k) + \omega_r(k)/2) \\ y_r(k) + v_r(k) \cdot \sin(\phi_r(k) + \omega_r(k)/2) \\ \phi_r(k) + \omega_r(k) \end{bmatrix}$$

with compact form: $\mathbf{x}(k+1) = f(\mathbf{x}(k), \mathbf{u}(k)) + noise$

B. Measurement model:

$\mathbf{z} = [x_f \ y_f]^T$, where x_f, y_f represents the Cartesian position of the magnetic markers.

$$h(\mathbf{x}(k)) = \begin{bmatrix} x_r(k) + d \cdot \cos(\phi_r(k) + \alpha) \\ y_r(k) + d \cdot \sin(\phi_r(k) + \alpha) \end{bmatrix}$$

where: $d = \sqrt{d_m^2 + b^2}$ and $\alpha = \arctan(d_m/b)$, d_m is the measure (see Fig. 7.4), and b is a parameter of measurement system

The compact form: $\mathbf{z}(k) = h(\mathbf{x}(k)) + noise$

1. EKF fusion algorithm:

1.1 prediction stage:

$$\hat{\mathbf{x}}(k|k-1) = f(\hat{\mathbf{x}}(k-1|k-1), \mathbf{u}(k))$$

$$P(k|k-1) = A(k)P(k-1|k-1)A^T(k) + Q(k)$$

$$\text{where } A(k) = \begin{bmatrix} 1 & 0 & -v_r(k) \cdot \sin(\phi_r(k) + \omega_r(k)/2) \\ 0 & 1 & -v_r(k) \cdot \cos(\phi_r(k) + \omega_r(k)/2) \\ 0 & 0 & 1 \end{bmatrix}$$

1.2 correction stage

$$S(k) = H(k)P(k|k-1)H^T(k) + R(k)$$

$$K(k) = P(k|k-1)H^T(k)S^{-1}(k)$$

$$\hat{\mathbf{x}}(k|k) = \hat{\mathbf{x}}(k|k-1) + K(k)(\mathbf{z}(k) - h(\hat{\mathbf{x}}(k|k-1)))$$

$$P(k|k) = P(k|k-1) - K(k)H(k)P(k|k-1)$$

$$\text{where } H(k) = \begin{bmatrix} 1 & 0 & -d \cdot \sin(\phi_r(k) + \alpha) \\ 0 & 1 & d \cdot \cos(\phi_r(k) + \alpha) \end{bmatrix}$$

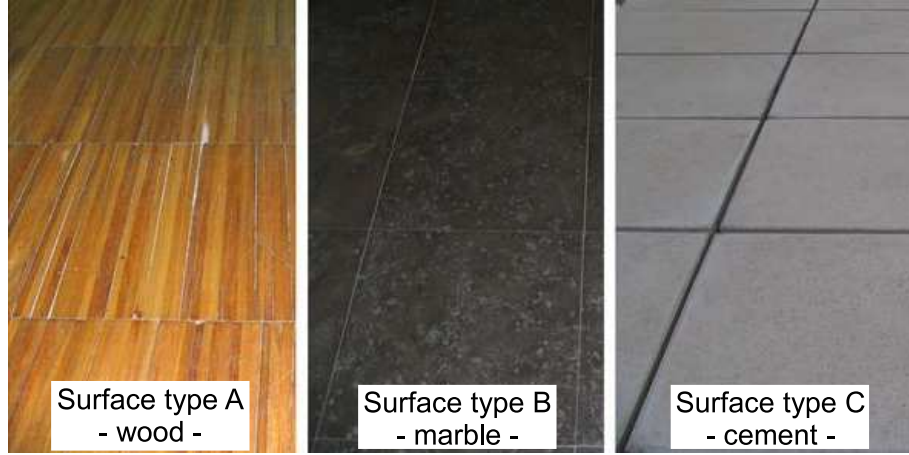


Figure 7.5: Surfaces used in the determination of acceleration limits.

The obtained maximum acceleration, a_r , and maximum deceleration, d_r , were

$$a_r = \min(a_{rA}, a_{rB}, a_{rC}) = \min(2.16, 2.64, 2.53) = 2.16m/s^2 \quad (7.2)$$

and

$$d_r = \min(d_{rA}, d_{rB}, d_{rC}) = \min(-18.80, -20.53, -16.42) = -16.42m/s^2 \quad (7.3)$$

7.3.3 Maximum Velocity to Avoid Sliding Out

The maximum velocity when travelling along a curve depends on the curvature of the path and the wheel ground adherence. Figure 7.7 shows the free body diagram for the robot. N_c and F_c represent the resultant of the normal and frictional forces for all wheels respectively. W is the weight of the robot and a_n is the normal acceleration. The forces in the y - $axis$ direction can be expressed as:

$$\leftarrow \sum F_n = m \cdot a_n; \quad F_c = m \cdot a_n \quad (7.4)$$

F_c can be expressed in terms of the normal force N_c as

$$F_c = \mu_s \cdot N_c \quad (7.5)$$

where μ_s is the static coefficient of friction between the ground and the wheels. This value was experimentally determined to be 0.556 (see Subsection 7.3.5 for more details).

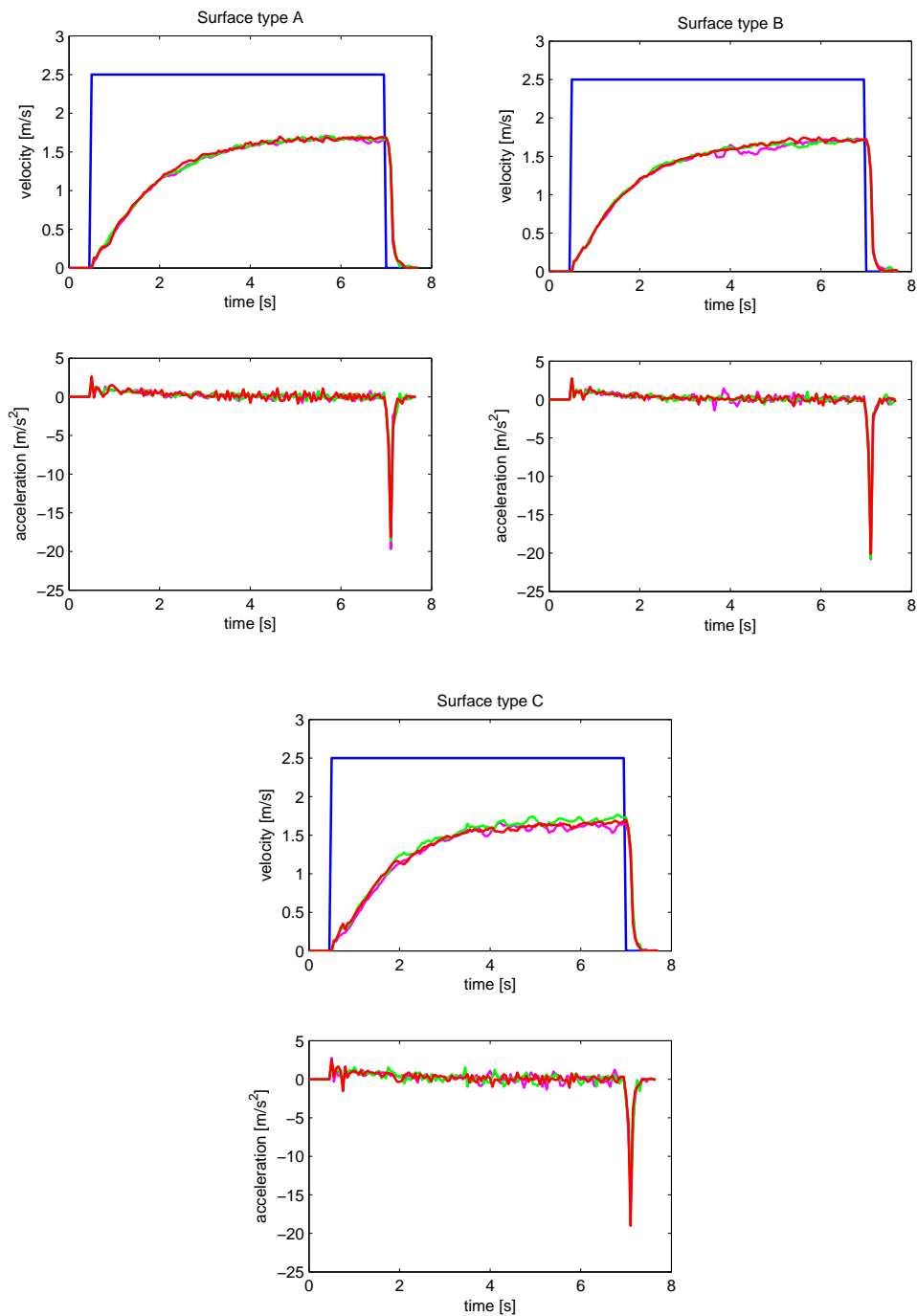


Figure 7.6: Experimental (green and red) and desired (blue) wheels speed values used to determine the maximum acceleration and deceleration of the RobChair.

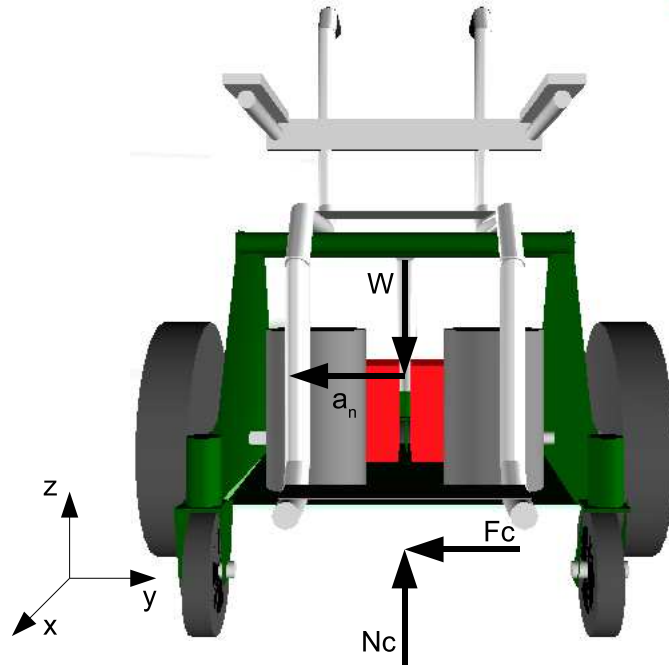


Figure 7.7: Free body diagram showing the RobChair mobile robot (in plane yz).

The forces in the z direction can be expressed as follows:

$$\uparrow \sum F_z = 0; \quad W = m \cdot g = N_c \quad (7.6)$$

The normal acceleration, a_n , can be expressed in terms of velocity v_r , and curvature, k :

$$a_n = v_r^2 \cdot k \quad (7.7)$$

Combining (7.5), (7.6) and (7.7) results in:

$$\mu_s \cdot N_c = m \cdot v_r^2 \cdot k \quad (7.8)$$

Solving for v_r and substituting (7.6) into (7.8) provides the maximum velocity to avoid sliding out as

$$v_{slide} = \sqrt{\frac{\mu_s \cdot g}{k_{max}}} \quad (7.9)$$

where k_{max} is the highest curvature of the entire path.

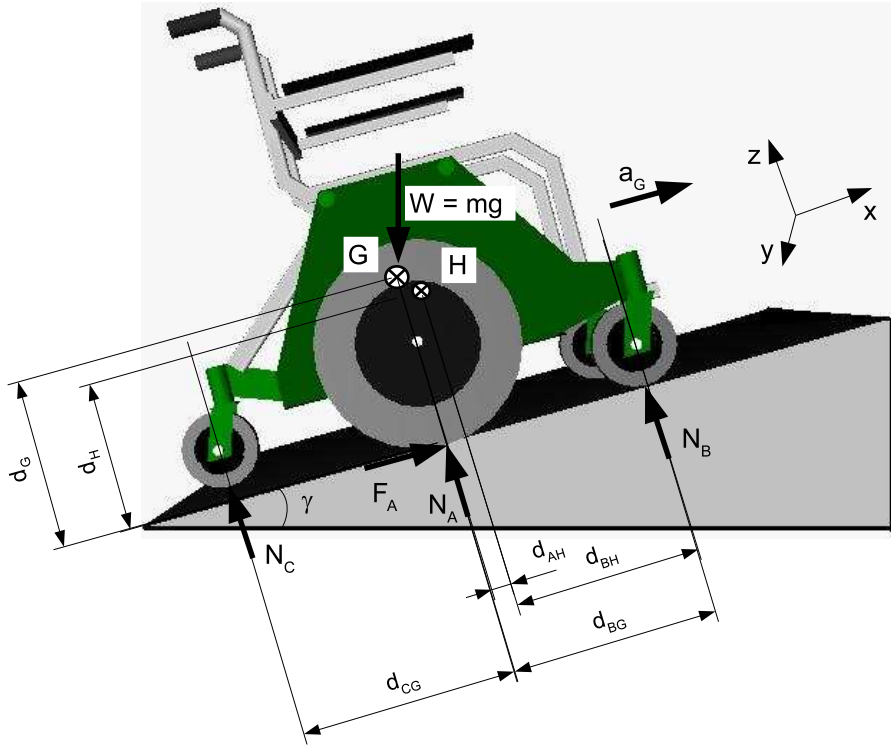


Figure 7.8: Free body diagram to find the maximum acceleration before wheel slippage.

7.3.4 Wheel-Ground Interaction to Avoid Slippage

The maximum acceleration to avoid wheel slippage is bounded by the wheel-ground adherence. For assuring that wheel slippage does not occur, the frictional force must not overcome the normal force multiplied by the coefficient of friction. The maximum acceleration can be calculated by setting

$$F_A = \mu_s \cdot N_A \quad (7.10)$$

where F_A is the frictional force, N_A is the normal force and μ_s is the static coefficient of friction between the wheels and the ground (see Subsection 7.3.5 for more details). The free body diagram for the problem is shown in Fig 7.8. In order to find the maximum acceleration, the equations of motion must be derived and solved. The mass of the robot (including batteries) is $m = 75.5$ kg.

The equations of motion can be expressed as follows:

$$\nearrow \sum F_x = m \cdot a_G; \implies F_A - m \cdot g \cdot \sin(\gamma) = m \cdot a_G \quad (7.11)$$

$$\nwarrow \sum F_z = 0; \implies N_C + N_A + N_B - m \cdot g \cdot \cos(\gamma) = 0 \quad (7.12)$$

$$\odot \sum M_G = 0; \implies -d_{CG} \cdot N_C + d_{AG} \cdot N_A + d_{BG} \cdot N_B + d_G \cdot F_A = 0 \quad (7.13)$$

$$\odot \sum M_{G,H} = 0; \implies d_{AH} \cdot N_A - d_{BH} \cdot N_B + d_H \cdot F_A = 0 \quad (7.14)$$

N_A is the normal force acting on the driving wheels, F_A is the frictional force of the driving wheels, N_B is the normal force acting on the caster wheels, a_G is the acceleration of the center of gravity of the wheelchair, and γ is the angle of the ground with respect to a horizontal surface. The angle is bound to $-8.53^\circ \leq \gamma \leq 8.53^\circ$, which is about a 15% grade. The frictional force of the caster wheels is neglected since they are assumed to be free-rolling. The equations of motion along with equation (7.10) give a total of 5 equations for 5 unknowns; therefore, the maximum acceleration, before slippage occurs, can be calculated to be:

$$a_{slip} = a_G = \frac{\mu_s \cdot d_{BH} \cdot d_{CG} \cdot g \cdot \cos(\gamma)}{(d_{CG} + d_{BG})(d_{AH} + d_H \cdot \mu_s) - d_{BH}(d_{CG} + d_{AG} + d_G \cdot \mu_s)} - g \cdot \sin(\gamma) \quad (7.15)$$

The maximum deceleration, before slippage occurs, can be calculated to be:

$$d_{slip} = -a_{slip} \quad (7.16)$$

7.3.5 Calculation of the Coefficient of Friction

Calculating the static coefficient of friction (μ_s) between the RobChair drive wheels and the ground was accomplished by running a series of tests. The wheelchair was placed on a flat clean surface and a cable was attached to the robot. Engaging the robot brakes ensured that the drive wheels would not rotate during the tests. A spring scale was attached to the cable to record the amount of force required to cause RobChair to begin sliding. The observed required force was 26.3 kg. Figure 7.9 displays the forces acting on the robot.

The frictional and normal forces can be obtained by solving the following set of equations of motion:

$$\leftarrow \sum F_x = 0 \implies F - F_A = 0 \quad (7.17)$$

$$\uparrow \sum F_z = 0 \implies N_C + N_A + N_B - W = 0 \quad (7.18)$$

$$\odot \sum M_G = 0 \implies -d_{CG} \cdot N_C + d_{AG} \cdot N_A + d_{BG} \cdot N_B + d_G \cdot F_A + d_F \cdot F = 0 \quad (7.19)$$

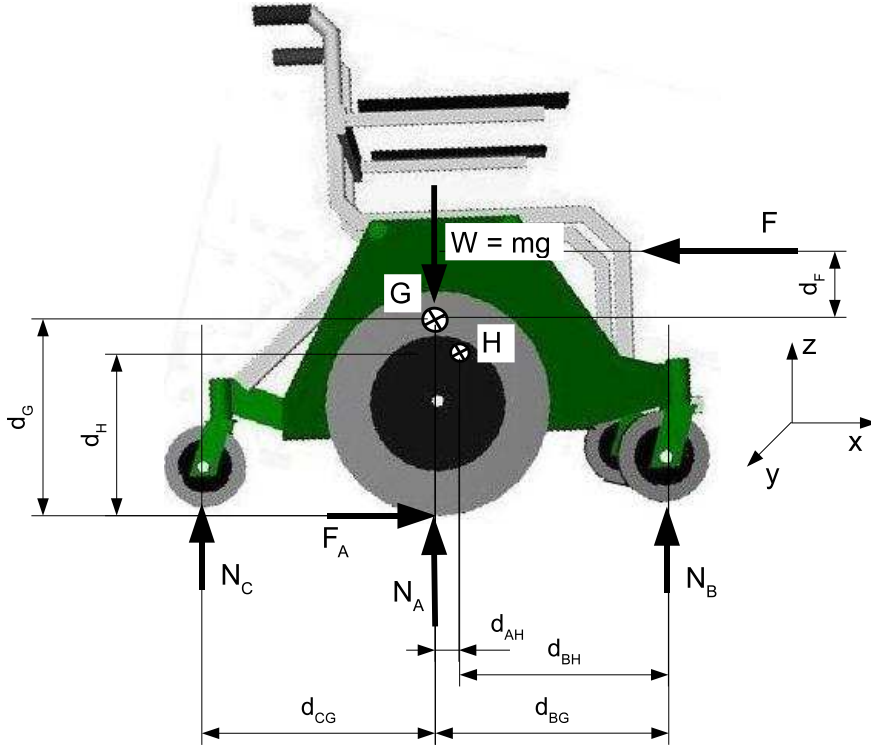


Figure 7.9: Schematic showing the forces acting on RobChair to cause it to move.

$$\odot \sum M_{G,H} = 0 \Rightarrow d_{AH} \cdot N_A - d_{BH} \cdot N_B + d_H \cdot F_A + d_F \cdot F = 0 \quad (7.20)$$

The equations can be solved to give:

$$\begin{aligned} F_A &= 258N \\ N_A &= 464.15N \\ N_B &= 248.15N \\ N_C &= 28.3N \end{aligned} \quad (7.21)$$

Referring to (7.10), results for the coefficient of friction,

$$\begin{aligned} F_A &= \mu_s \cdot N_A \\ \mu_s &= 0.556 \end{aligned} \quad (7.22)$$

7.3.6 Bounded Wheel Speed Commands

The kinematic model linking the scalars v_r , ω_r , v_R and v_L is:

$$v_r = \frac{v_R + v_L}{2} \quad (7.23)$$

$$\omega_r = \frac{v_R - v_L}{2 \cdot b} \quad (7.24)$$

where $|v_R|$ and $|v_L|$ will be bounded by some given value V_{max} .

Assuming that forward and backward velocities of the right and left wheels of a differential-drive WMR are equally bounded by a maximum velocity V_{max} , the set of feasible wheel velocities (v_R, v_L) can be transformed into the set of feasible WMR velocities (v, ω) , as illustrated by the rhombic shape in Fig. 7.10.

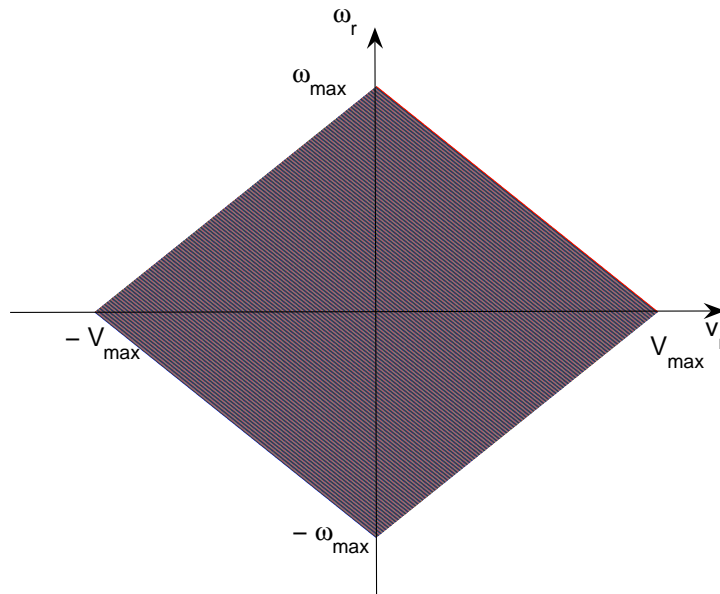


Figure 7.10: Feasible WMR velocities.

As known, a differential-drive WMR modeled by equations (7.23) and (7.24) can move on paths of arbitrary curvature k , as:

$$k = \frac{v_R - v_L}{b \cdot (v_R + v_L)} \quad (7.25)$$

Indeed for any $v_L = -v_R$ the corresponding path curvature would be infinite, i.e. the vehicle would turn on the spot. If the wheel speeds v_L and v_R are constrained to positive values only, than the curvature k given by equation (7.25) would be bounded:

$$-\frac{1}{b} \leq k \leq \frac{1}{b}, \quad v_R, v_L \in [0, V_{max}] \quad (7.26)$$

Figure 7.11 shows that in order to exploit the full range $[-1/b, 1/b]$ of possible

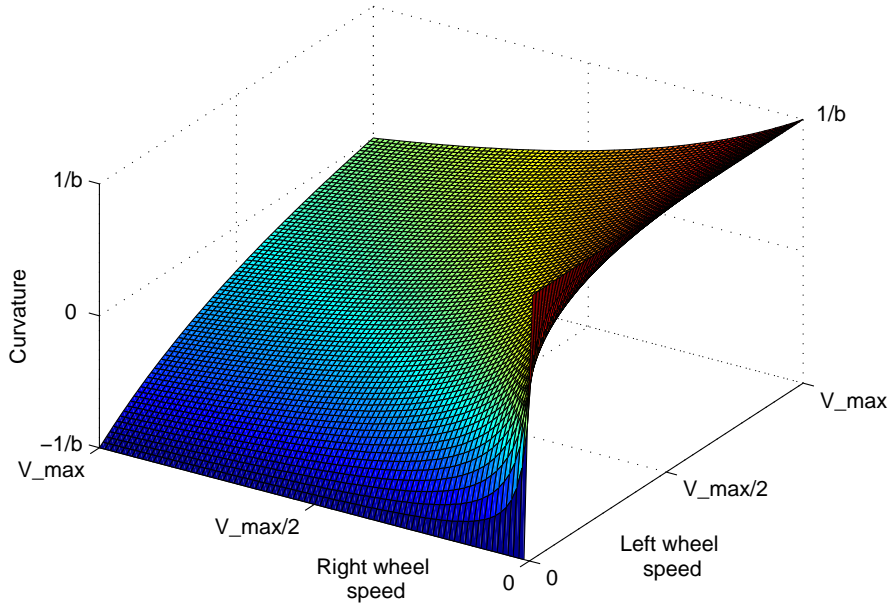


Figure 7.11: Differential drive curvature as function of the wheels speeds.

curvatures at all times with the constraints, $0 \leq v_L, v_R \leq V_{max}$. The linear speed $v_r(t)$ of a differential drive vehicle should always be smaller or equal to $V_{max}/2$. The maximum feasible linear velocity would be of course V_{max} corresponding to $v_L = v_R = V_{max}$. Notice that the wheels of differential drive robot turn in one direction only (i.e. $v_L, v_R \geq 0$), given that the resulting admissible curvature is bounded ($|k| \leq 1/b$), in any path-following application the desired path curvature k_d will need to be bounded too. In the sequel, the upper bound of the absolute value of the reference path curvature will be denoted by k_{dmax} ($k_{dmax} > 0$) and it will be assumed that:

$$|k_d| \leq k_{dmax} \leq \frac{1}{b} \quad (7.27)$$

In Fig. 7.12, point C corresponds to $v = 0$, point D to $u = V_{max}$ and the line AB corresponds to $v = V_{max}/2$. All points belonging to lines parallel to AB refer to constant values of v , in particular all points in the region ABC refer to linear robot velocities $\in [0, V_{max}/2]$ and all points in ABD refer to linear velocities $\in [V_{max}/2, V_{max}]$. Points on the (non depicted) line CD from C to D refer to increasing linear speeds with zero curvature (i.e. angular velocity) due to the fact that the two wheels have the same speed.

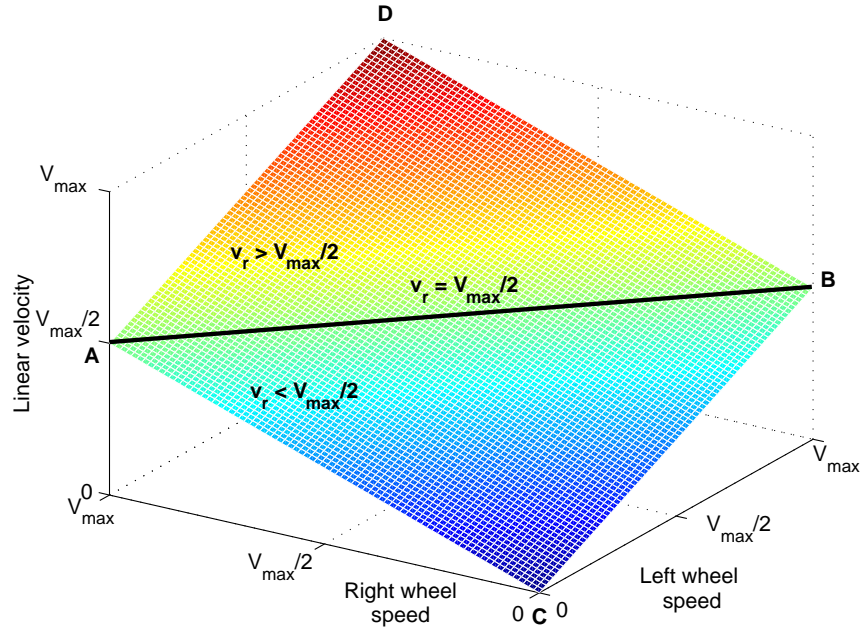


Figure 7.12: Linear velocity as function of wheels' speed.

7.3.7 Dynamic Constraints

To avoid wheel slippage, the dynamic constraints such as the wheel acceleration bound should be considered in the design of the path-following or path-tracking controller. Any abrupt change in the robot motion may cause slippage or mechanical damage to the mobile robot. If the angular acceleration of each wheel is limited by $\dot{\omega}_{max}$

$$|\dot{\omega}_{R,L}| \leq \dot{\omega}_{max} \quad (7.28)$$

then, from (7.23) and (7.24), the tangential and angular accelerations of the robot are bounded by:

$$|a_v| + b \cdot |a_\omega| \leq r \cdot \dot{\omega}_{max} \quad (7.29)$$

The ranges of each value to be independently considered are obtained by taking half the value of each maximum as:

$$|a_v| \leq \frac{r \cdot \dot{\omega}_{max}}{2} \quad (7.30)$$

$$|a_\omega| \leq \frac{r \cdot \dot{\omega}_{max}}{2 \cdot b} \quad (7.31)$$

7.3.8 Feasible Constraints

Using the constraints in the previous section, the values for the maximum velocity, acceleration, and deceleration can be obtained as follows:

$$\begin{aligned} v_d(t) &\leq V_{lim} \\ a_d(t) &\leq A_{lim} \\ d_d(t) &\geq D_{lim} \end{aligned} \tag{7.32}$$

where

$$\begin{aligned} V_{lim} &= \min(v_r, v_{slide}) \\ A_{lim} &= \min(a_r, a_{slip}, a_w) \\ D_{lim} &= \min(d_r, d_{slip}) \end{aligned} \tag{7.33}$$

where v_r , v_{slide} , a_r , a_{slip} , d_r , d_{slip} , are obtained from equations (7.1), (7.9), (7.2), (7.15), (7.3), (7.16) respectively.

7.4 Experimental Results

A set of experimental tests, using RobChair [136], [137], has been performed to evaluate the performance of the sliding mode controllers (SM-TT and SM-PF), and the trajectory planning algorithm with comfort constraint.

According to the notation shown in Fig. 7.4, the RobChair parameter values are $L = 0.614m$ and $R = 0.175m$. For all the experiments, the following values of the SM-TT and SM-PF controllers (see (5.60), (5.61) for SM-TT and (5.60), (5.78), (5.79) for SM-PF)were used: $k_0 = 4$, $k_1 = 0.75$, $k_2 = 5$, $p_1 = 0.05$, $p_2 = 0.05$, $q_1 = 0.75$, $q_2 = 1.75$. The signum functions in the command signals were replaced by saturation functions with ± 0.15 thresholds, to reduce the chattering phenomenon.

7.4.1 Experimental Results Under Odometry Navigation

As shown in Fig. 7.13, the first experiment reported here concerns the implementation of the SM-TT in the following conditions: 1) only odometry feedback is used; 2) initial pose error ($x_e = -1$, $y_e = -1$ and $\phi_e = 0$). The same figure shows that the RobChair retrieved quickly ($\Delta t \approx 10s$) and smoothly from its initial state error, and the tracking errors converge on average to zero with acceptable reduced values along the path.

Experimental results for SM-TT controller under odometry navigation (without

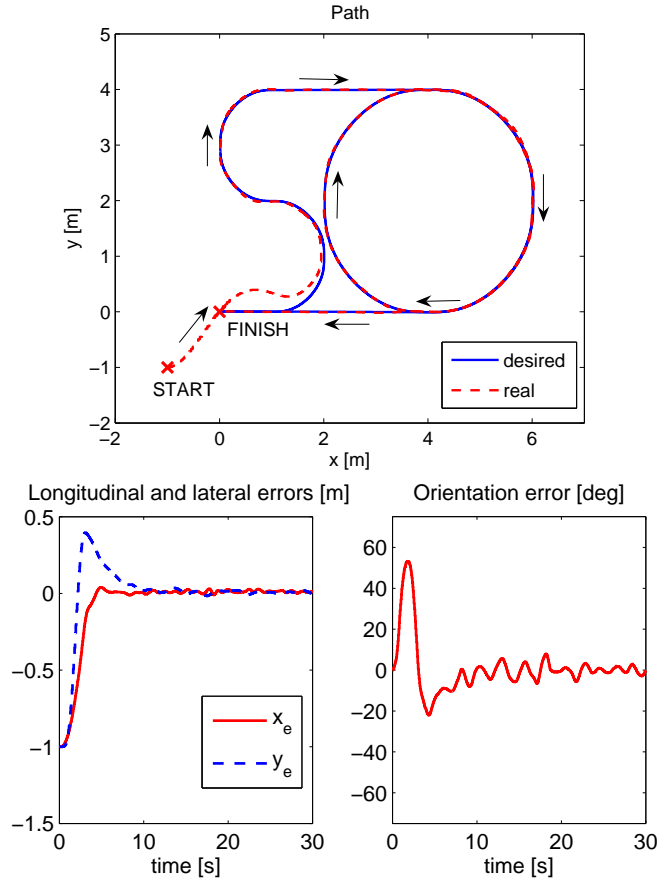


Figure 7.13: Experimental SM-TT control starting from an initial error state ($x_e(0) = -1$, $y_e(0) = -1$, $\phi_e(0) = 0$), under odometry navigation.

initial pose errors) for two different trajectories (illustrated in Fig. 7.14) are shown in Tables 7.2 and 7.3. Three experimental trials were executed for each path. The table shows the maximum (Max), root mean square (rms), rms accelerations a_{wx} , a_{wy} and a_{wz} (on x , y and z axes), and the overall rms acceleration a_w values (see (6.3)).

The maximum absolute values of lateral and longitudinal errors are under 0.065 m and the overall r.m.s. acceleration values (a_w) are below 0.5 m/s^2 . This value is in the range of “a little uncomfortable” (see Table 6.2).

7.4.2 Experimental Results Under Magnetic-markers Navigation

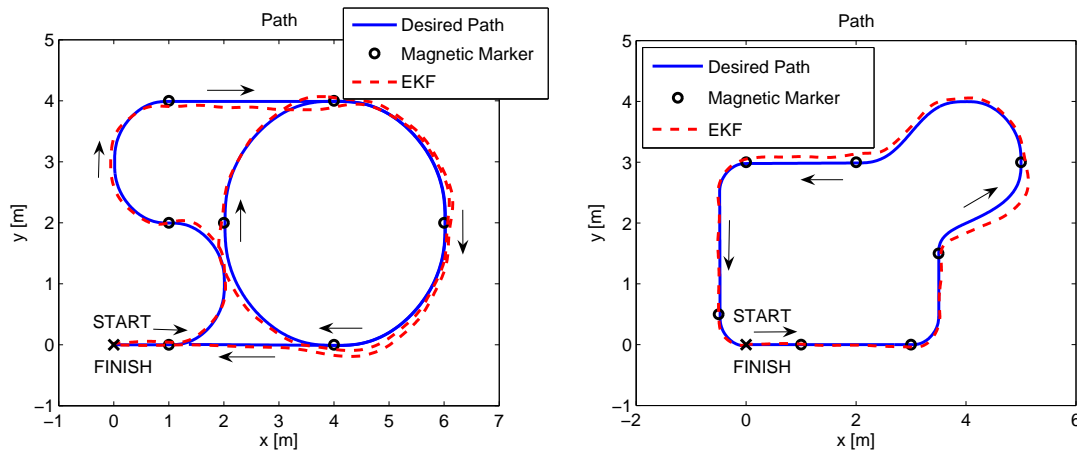
Another set of experiments using SM-TT controller (Fig. 7.14), and SM-PF controller (Fig. 7.15), was made for two type of trajectories without initial pose errors when the odometric data is fused with absolute position data from magnetic markers. The

Table 7.2: Experimental results for SM-TT controller under odometry navigation.

Case	No	Max x_e [m]	rms x_e [m]	Max y_e [m]	rms y_e [m]	Max. θ_e [rad]	rms θ_e [rad]
<i>Path – 1</i>	I	0.0419	0.0152	0.0612	0.0140	0.2263	0.0461
	II	0.0450	0.0159	0.0448	0.0113	0.1689	0.0426
	III	0.0493	0.0182	0.0864	0.0195	0.2787	0.0514
average		0.0454	0.0164	0.0641	0.0149	0.2246	0.0467
<i>Path – 2</i>	I	0.0581	0.0245	0.0614	0.0190	0.2935	0.0769
	II	0.0498	0.0232	0.0560	0.0181	0.3775	0.0783
	III	0.0492	0.0211	0.0406	0.0137	0.2171	0.0649
average		0.0524	0.0229	0.0527	0.0169	0.2960	0.0734

Table 7.3: Experimental results for SM-TT controller under odometry navigation.

Case	No	a_{wx} [m/s^2]	a_{wy} [m/s^2]	a_{wz} [m/s^2]	a_w [m/s^2]
<i>Path – 1</i>	I	0.2407	0.2029	0.0618	0.4452
	II	0.2417	0.2052	0.0600	0.4480
	III	0.2354	0.1891	0.0570	0.4266
average		0.2393	0.1991	0.0596	0.4399
<i>Path – 2</i>	I	0.2696	0.2356	0.0564	0.5045
	II	0.2710	0.2149	0.0531	0.4872
	III	0.2777	0.2246	0.0572	0.5034
average		0.2728	0.2250	0.0556	0.4984

Figure 7.14: Experimental SM-TT control under magnetic-markers navigation: Left) *Path – 1*; Right) *Path – 2*. In both paths, the circles represent the positions of the seven magnetic markers used in the experiment.

extended Kalman filter was used for the fusion process, as summarized in Table 7.1.

The pictures of the real experiments are shown in Fig. 7.16.

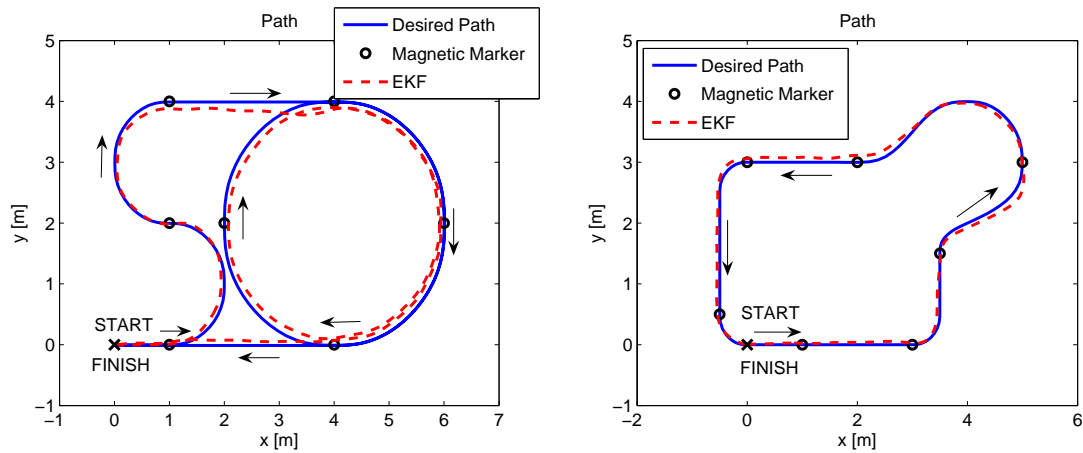


Figure 7.15: Experimental SM-PF control under magnetic-markers navigation: Left) *Path – 1*; Right) *Path – 2*. In both paths, the circles represent the positions of the seven magnetic markers used in the experiment.

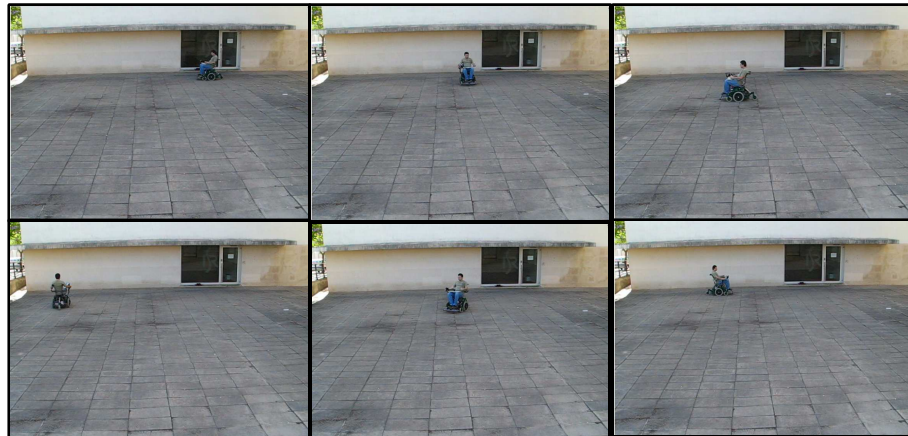


Figure 7.16: RobChair pictures at different positions in a real experiment.

Figures 7.17 and 7.18 show desired, command and real linear and angular velocities for SM-TT control. Corrections in the pose after each magnetic marker detection provokes an error signal that is efficiently dealt by the SM-TT controller, and rapidly the tracking errors converge to zero (see Fig. 7.19). All the experimental results for SM-TT controllers under magnetic-markers navigation are summarized in Tables 7.4 and 7.5.

The maximum absolute values of lateral and longitudinal errors are under 0.28 m and the overall r.m.s. acceleration values (a_w) are below 0.55 m/s^2 .

Experimental results for SM-PF controller (using 5.78 and 5.79) under magnetic-markers navigation (without initial pose errors) for two different trajectories (Fig. 7.15) are shown in Table 7.6. In this case, a constant longitudinal velocity command

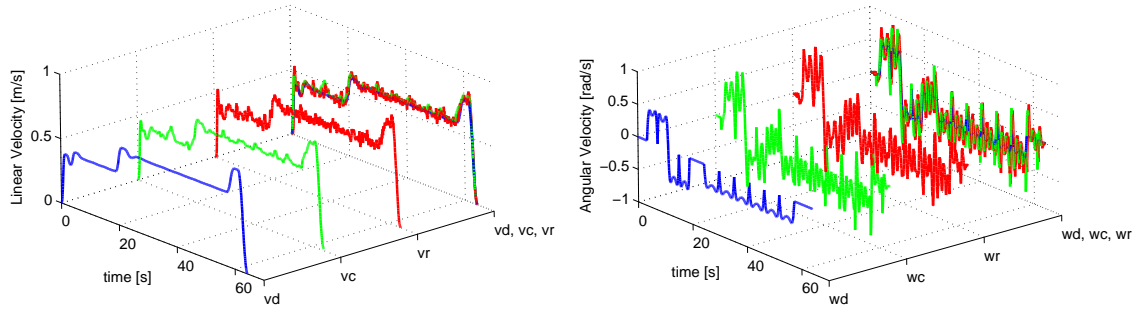


Figure 7.17: Desired (v_d, ω_d), command (v_c, ω_c) and real (v_r, ω_r) linear and angular velocities for SM-TT control using an EKF-based fusion in the on-line pose estimation - *Path - 1*.

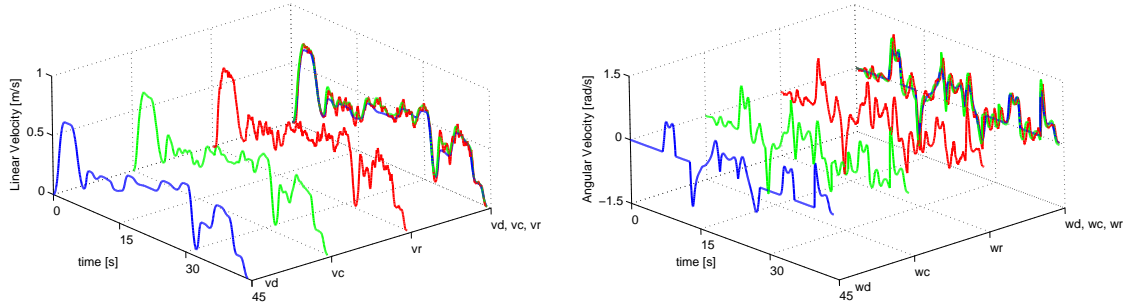


Figure 7.18: Desired (v_d, ω_d), command (v_c, ω_c) and real (v_r, ω_r) linear and angular velocities for SM-TT control using an EKF-based fusion in the on-line pose estimation - *Path - 2*.

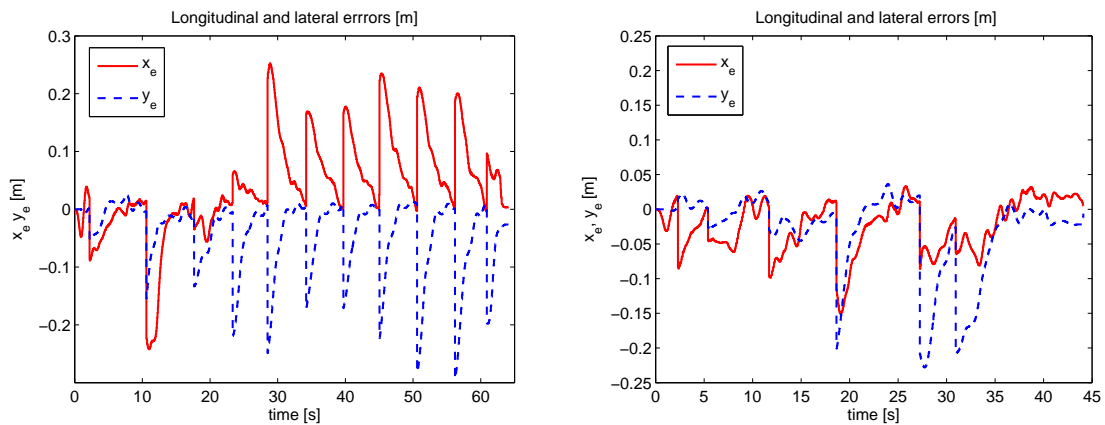


Figure 7.19: Longitudinal and lateral errors of SM-TT control under magnetic-markers navigation: Left) *Path - 1*; Right) *Path - 2*.

of $v_c = 0.5m/s$ was used. Three experimental trials were executed for each path. The table shows the maximum (Max), root mean square (rms), rms accelerations a_{wx}, a_{wy}

Table 7.4: Experimental results for SM-TT controller under magnetic-markers navigation.

Case	No	Max x_e [m]	rms x_e [m]	Max y_e [m]	rms y_e [m]	Max. θ_e [rad]	rms θ_e [rad]
<i>Path – 1</i>	I	0.2528	0.0923	0.2932	0.0768	0.3779	0.0950
	II	0.2210	0.0517	0.1982	0.0424	0.2572	0.0721
	III	0.2039	0.0748	0.1945	0.0452	0.2527	0.0642
average		0.2259	0.0729	0.2286	0.0548	0.2959	0.0771
<i>Path – 2</i>	I	0.1626	0.0586	0.2222	0.0626	0.2299	0.0698
	II	0.1647	0.0511	0.2390	0.0687	0.2585	0.0758
	III	0.1849	0.0515	0.2739	0.0685	0.2982	0.0814
average		0.1707	0.0537	0.2450	0.0666	0.2622	0.0757

Table 7.5: Experimental results for SM-TT controller under magnetic-markers navigation.

Case	No	a_{wx} [m/s ²]	a_{wy} [m/s ²]	a_{wz} [m/s ²]	a_w [m/s ²]
<i>Path – 1</i>	I	0.2275	0.2138	0.0584	0.4410
	II	0.2502	0.2247	0.0709	0.4761
	III	0.2222	0.1977	0.0652	0.4215
average		0.2333	0.2121	0.0648	0.4462
<i>Path – 2</i>	I	0.3071	0.2234	0.0518	0.5342
	II	0.2892	0.2447	0.0565	0.5334
	III	0.3023	0.2416	0.0753	0.5470
average		0.2995	0.2366	0.0612	0.5382

Table 7.6: Experimental results for SM-PF controller under magnetic-markers navigation.

Case	No	Max y_e [m]	rms y_e [m]	Max. θ_e [rad]	rms θ_e [rad]	a_{wx} [m/s ²]	a_{wy} [m/s ²]	a_{wz} [m/s ²]	a_w [m/s ²]
<i>Path – 1</i>	I	0.2189	0.0704	0.3689	0.1348	0.2736	0.1713	0.0304	0.4530
	II	0.1658	0.0690	0.3661	0.1319	0.2687	0.1635	0.0326	0.4416
	III	0.2142	0.0789	0.3581	0.1424	0.2702	0.1674	0.0339	0.4463
average		0.1996	0.0728	0.3644	0.1364	0.2708	0.1674	0.0323	0.4470
<i>Path – 2</i>	I	0.1341	0.0437	0.5350	0.1493	0.2994	0.2468	0.0350	0.5444
	II	0.1642	0.0532	0.6261	0.1679	0.3094	0.2247	0.0390	0.5367
	III	0.2680	0.0725	0.5878	0.1489	0.3047	0.2309	0.0410	0.5368
average		0.1888	0.0565	0.5830	0.1554	0.3045	0.2341	0.0383	0.5393

and a_{wz} (on x , y and z axes), and the overall rms acceleration a_w values (see (6.3)).

The maximum absolute values of lateral error (y_e) are under 0.27 m and the overall

r.m.s. acceleration values (a_w) are below 0.55 m/s^2 . By definition of orthogonal projection, the longitudinal error x_e is zero in the SM-PF case. The maximum and r.m.s values of heading errors are bigger in case of SM-PF. Also, the longitudinal r.m.s. accelerations (a_{wx}) are larger in the SM-PF case, as would be expectable, once longitudinal control was under a constant velocity command ($v_c = 0.5 \text{ m/s}$) rather than under a velocity profile fitted for the course in the SM-TT case.

Figure 7.20 shows experimental acceleration data from IMU and from encoders (first derivative of velocity) for SM-TT control under magnetic-markers navigation.

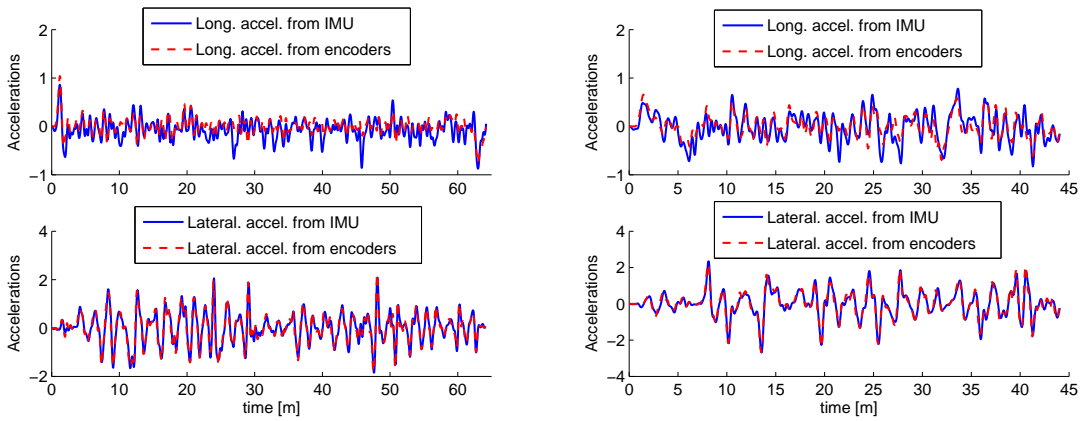


Figure 7.20: Longitudinal and lateral accelerations from IMU and from encoders in case of SM-TT control, Left) *Path – 1*; Right) *Path – 2*.

Chapter 8

Conclusions

This thesis describes trajectory-tracking and path-following controllers based on the sliding-mode theory for WMRs and autonomous vehicles. Moreover, a trajectory planning algorithm is described that deals with comfort constraints providing smooth trajectories with low associated accelerations. The proposed control structure is based on two nonlinear sliding surfaces ensuring the tracking of the three output variables, exploiting the nonholonomic constraint. The control law has been thoroughly evaluated in terms of tracking performance either by simulation and real experiments. Using the trajectory planner, trajectories are generated that comply with user comfort requirements by exposing him/her to acceptable levels of accelerations, being its maximum value a design parameter.

The experimental tests presented in this thesis are representative of the average performance of the controllers. I had summarized my acquired experience in general observations that can be useful guidelines for implementation of the same control strategies in other type of mobile robots.

The following suggestions are recommended for future work:

- It would be interesting to study the sliding-mode control design using the WMR dynamical model, where uncertainties in the robot physical parameters exist.
- The performances of the four reaching laws (Chapter 5) can be compared in order to establish an on-line parameters adjusting procedure and deserves more study.
- The trajectory planners that work directly with a library of skills (perception and motor skills) should be investigated, instead of working with preprogrammed planners.

The topic of nonlinear control systems is large and receives a lot of research interest in both journals and conferences. This thesis has touched aspects with relevance to controller design, robotics and in particular mobile robotics. Questions have been answered, new ones have appeared. With the appearance of smarter sensors, faster computers, and more reliable data processing, the design and implementation of nonlinear control techniques for mobile robotics are of great interest and should attract further investigations.

Appendix A

Appendix

Definition (G^1 -curves): A parametric curve $p(u)$ has first-order geometric continuity, and we say $p(u)$ is a G^1 -curve, if $p(u)$ is regular and its unit tangent vector is a continuous function along the curve, i.e., $\tau(\cdot) \in C^0([u_0, u_1])$.

Definition (G^2 -curves): A parametric curve $p(u)$ has second-order geometric continuity, and we say $p(u)$ is a G^2 -curve, if $p(u)$ is G^1 -curve and its curvature vector is continuous along the curve.

Definition (Comfort): from <http://www.websters-online-dictionary.org/>

1. a state of being relaxed and feeling no pain;
2. a feeling of freedom from worry or disappointment;
3. the act of consoling; giving relief in affliction.

Barbalat's Lemma: from Khalil Lemma 8.2 [138], let $\phi : \mathfrak{R} \rightarrow \mathfrak{R}$ be a uniformly continuous function on $[0, \infty)$. Suppose that

$$\lim_{t \rightarrow \infty} \int_0^t \phi(\tau) d\tau \quad (\text{A.1})$$

exists and is finite. Then, $\phi(t) \rightarrow 0$ as $t \rightarrow \infty$.

Extension of Barbalat's Lemma: Barbalat's lemma is extended to show global asymptotic stability in Khalil Theorem 8.4 [138]. Let $D \subset \mathfrak{R}^n$ be a domain containing $x = 0$ and suppose $f(t, x)$ is piecewise continuous in t and locally Lipschitz in x . Let V be a continuously differentiable function such that

$$W_1(x) \leq V(x) \leq W_2(x) \dot{V}(x) \leq -W(x) \quad (\text{A.2})$$

for all $x \in D$, where $W_1(x)$ and $W_2(x)$ are continuous positive definite functions and $W(x)$ is a continuous positive semidefinite function on D . Choose $r > 0$ such that $B_r \subset D$ and let $\rho < \min_{\|x\|=r} W_1(x)$. Then all solutions of $\dot{x} = f(x)$ with $x(0) \in \{x \in B_r | W_2(x) \leq \rho\}$ are bounded and satisfy

$$W(x) \rightarrow 0 \text{ as } t \rightarrow \infty \quad (\text{A.3})$$

If all of the above assumptions hold globally and $W_1(x)$ is radially unbounded, the statement is true for all $x(0) \in \mathfrak{R}^n$.

Global Asymptotic Lyapunov Stability From Khalil Theorem 4.2 [138], let a general nonlinear, time invariant system $\dot{x} = f(x)$, have an equilibrium point at $x = 0$. System equilibrium points not located at $x = 0$ may be moved to the origin through a suitable coordinate transformation. Define a continuously differentiable Lyapunov function $V : \mathfrak{R}^n \rightarrow \mathfrak{R}$ such that

$$V(0) = 0 \text{ and } V(x) > 0, \forall x \neq 0 \|x\| \rightarrow \infty \Rightarrow V(x) \rightarrow \infty \dot{V}(x) < 0, \forall x \neq 0 \quad (\text{A.4})$$

then the origin $x = 0$ is globally asymptotically stable. This implies the system has only one equilibrium point.

LaSalle's Theorem From Khalil Theorem 4.4 [138], let $\Omega \subset D$ be a compact set that is positively invariant with respect to $\dot{x} = f(x)$. Let $V : \mathfrak{R}^n \rightarrow \mathfrak{R}$ be a continuously differentiable function such that $\dot{V}(x) \leq 0$ in Ω . Let E be the set of all points in Ω where $\dot{V}(x) = 0$. Let M be the largest invariant set in E . Then every solution starting in Ω approaches M as $t \rightarrow \infty$.

This may be extended to asymptotic stability by Khalil Corollary 4.2 [138], let $x = 0$ be an equilibrium point for $\dot{x} = f(x)$. Let $V : \mathfrak{R}^n \rightarrow \mathfrak{R}$ be a continuously differentiable, radially unbounded, positive definite function such that $\dot{V}(x) \leq 0$ for all $x \in \mathfrak{R}^n$. Let $S = \{x \in \mathfrak{R}^n | \dot{V}(x) = 0\}$ and suppose that no solution can stay identically in S , other than the trivial solution $x(t) \equiv 0$. Then, the origin is globally asymptotically stable.

The benefit of LaSalle's theorem is that it does not require \dot{V} to be negative definite for global asymptotic stability.

Bibliography

- [1] Masehian E. and Katebi Y. (2007). Robot Motion Planning in Dynamic Environments with Moving Obstacles and Target, *International Journal of Mechanical Systems Science and Engineering*, 1(1), 20–25.
- [2] Shiller Z., Large F., Sekhavat S. and Laugier C. (2007). Motion Planning in Dynamic Environments, *Autonomous Navigation in Dynamic Environments*, Vol. 35, Springer-Verlag, 107–119.
- [3] Wang M. and Liu J.N.K. (2008). Fuzzy Logic-based Real-time Robot Navigation in Unknown Environment with Dead Ends, *Robotics and Autonomous Systems*, Elsevier, 56(7), 625–643.
- [4] Fatmi A., Yahmadi A., Khriji L. and Masmoudi N. (2005). A Fuzzy Logic Based Navigation of a Mobile Robot, *International Journal of Applied Mathematics and Computer Sciences*, 1(2), 87–92.
- [5] Zavlangas P.G., Tzafestas S.G. and Althoefer K. (2000). Fuzzy Obstacle Avoidance and Navigation for Omnidirectional Mobile Robots, *European Symposium on Intelligent Techniques - ESIT 2000*, 375–382.
- [6] Lebedev D.V., Steil J.J. and Ritter H.J. (2005). The Dynamic Wave Expansion Neural Network Model for Robot Motion Planning in Time-varying Environments, *Neural Networks*, Elsevier, 18(3), 267–285.
- [7] Yang S.X., Hu T., Yuan X., Liu, P.X., Meng M. (2003). A Neural Network Based Torque Controller for Collision-free Navigation of Mobile Robots, *IEEE International Conference on Robotics and Automation*, 1, 13–18.
- [8] Kulic R., Vukic Z. (2003). Methodology of Concept Control Synthesis to Avoid Unmoving and Moving Obstacles, *Journal of Intelligent and Robotic Systems*, Springer-Verlag, 37(1), 21–41.

- [9] Kulić R., Vukić Z. (2006). Methodology of Concept Control Synthesis to Avoid Unmoving and Moving Obstacles II, *Journal of Intelligent and Robotic Systems*, Springer-Verlag, 45(3), 267–294.
- [10] Ye C. and Wang D. (2001). A Novel Navigation Method for Autonomous Mobile Vehicles, *Journal of Intelligent and Robotic Systems*, Springer-Verlag, 32(4), 361–388.
- [11] Zhuang Hui-Zhong, Du Shu-Xin and Wu Tie-Jun (2006). On-line Real-time Path Planning of Mobile Robots in Dynamic Uncertain Environment, *Journal of Zhejiang University - Science A*, Zhejiang University Press, co-published with Springer-Verlag, 7(4), 516–524.
- [12] Shi Chao-Xia, Hong Bing-Rong, Wang Yan-Qing and Piao Song-Hao. (2006). Autonomous Navigation Based on the Velocity Space Method in Dynamic Environments, *Lecture Notes in Computer Science*, Springer-Verlag, 4222/2006, 958–961.
- [13] Bloch A. M., McClamroch N. H. and Reyhanoglu M. (1990). Controllability and Stabilizability of Properties of a Nonholonomic Control Systems, *Proc. IEEE Conf. Decision and Control*, 1312-1314.
- [14] Divelbiss A. W. and Wen J. T. (1997). Trajectory Tracking Control of a Car-trailer System, *IEEE Transactions Control Systems Technology*, 5(3), 269-278.
- [15] Bloch, A. M. and McClamroch, N. H. (1989). Control of Mechanical Systems With Classical non Holonomic Constraints, *Proceeding of the 28th IEEE Conf. on Decision and Control*, Tampa, 201–205.
- [16] Samson C. and Ait-Abderrahim K. (1991). Feedback Control of a Nonholonomic Wheeled Cart in Cartesian Space, *Proceedings of IEEE International Conference on Robotics and Automation*, 2, 1136-1141.
- [17] Pomet J. B. (1992). Explicit Design of Time-varying Stabilizing Control Laws for a Class of Controllable Systems Without Drift, *Systems and Control Lett.*, 18, 147-158.
- [18] MCloskey R. T. and Murray R. M. (1994), Exponential Stabilization of Driftless Nonlinear Control Systems Using Homogeneous Feedback, *IEEE Transactions on Automatic Control*, 42(5), 614–628.

- [19] Kanayama Y., Kimura Y., Miyazaki F. and Noguchi T. (1990). A Stable Tracking Control Method for an Autonomous Mobile Robot, *Proceedings of IEEE International Conference on Robotics and Automation*, 1, 384-389.
- [20] Jiang Z.-P. and Nijmeijer H. (1997). Tracking Control of Mobile Robots: A Case Study in Backstepping, *Automatica*, 33(7), 1393-1399.
- [21] De Luca A. and Oriolo G. (1995). Modelling and Control of Nonholonomic Mechanical Systems, in: J. Angeles, A. Kecskemethy (Editors), *Kinematics and Dynamics of Multi-Body Systems*, Springer-Verlag, 277-342.
- [22] Oriolo G., De Luca A. and Vendittelli M. (2002). WMR Control Via Dynamic Feedback Linearization: Design, Implementation, and Experimental Validation. *IEEE Transactions on Control System Technology*, 10(6), 835-852.
- [23] Sarkar, N., Yun, X. and Kumar, V. (1992). Control of Mechanical Systems With Rolling Constraints: Application to Dynamic Control of Mobile Robots - Technical Report, *University of Pennsylvania Department of Computer and Information Science*, Technical Report No. MS-CIS-92-44.
- [24] Samson, C. (1993). Time-varying Feedback Stabilization of Car-like Wheeled Mobile Robots. *Int. Journal of Robotics Research*, 12(1), 55-64.
- [25] Zhang M. and Hirschorn R. M. (1997). Discontinuous Feedback Stabilization of Nonholonomic Wheeled Mobile Robots, *Dynamics and Control*, 7(2), 155-169.
- [26] Koh K.C. and Cho H.S. (1999). A Smooth Path Tracking Algorithm for Wheeled Mobile Robots with Dynamic Constraints, *Journal of Intelligent and Robotic Systems*, 24(4), 367-385.
- [27] Zhang Y., Chung J. H. and Velinsky S.A. (2003). Variable Structure Control of a Differentially Steered Wheeled Mobile Robot, *Journal of Intelligent and Robotic Systems*, 36(3), 301-314.
- [28] Yang, J.M. and Kim, J.H. (1999). Sliding Mode Control for Trajectory Tracking of Nonholonomic Wheeled Mobile Robots, *IEEE Transactions on Robotics and Automation*, 15(3), 578-587.
- [29] Kim M.S., Shin J.H. and Lee J.J. (2000). Design of a Robust Adaptive Controller for a Mobile Robot, *Proc. IEEE/RSJ Int. Conf. On Intelligent Robots and Systems*, 3, 1816-1826.

- [30] Fukao T., Nakagawa H., and Adachi N. (2000). Adaptive Tracking Control of a Nonholonomic Mobile Robot, *IEEE Transactions on Robotics and Automation*, 16(5), 609-615.
- [31] Coelho P. and Nunes U. (2005). Path-following Control of Mobile Robots in Presence of Uncertainties, *IEEE Transactions on Robotics*, 21(2), 252-261.
- [32] Li C.K. and Chao H.M. (2002). Output Tracking of Uncertain Robot Systems Via High Order Sliding Mode Technique, *Electronic letters*, 38(10), 487-489.
- [33] Corradini M.L. and Orlando G. (2002). Control of Mobile Robots with Uncertainties in the Dynamical Model: a Discrete Time Sliding Mode Approach with Experimental Results, *Control Engineering Practice*, 10(1), 23-34.
- [34] Wu S.-F., Mei J.-S. and Niu P.-Y. (2001). Path Guidance and Control of a Guided Wheeled Mobile Robot, *Control Engineering Practice*, 9(1), 97-105.
- [35] Jiang Z.-P., Lefeber E. and Nijmeijer H. (2001). Saturated Stabilization and Tracking of a Nonholonomic Mobile Robot, *Systems and Control Letters*, 42(5), 327-332.
- [36] Pourboghrat F. and Karlsson M. P. (2002). Adaptive Control of Dynamic Mobile Robots with Nonholonomic Constraints, *Computers and Electrical Engineering*, 28(4), 241-253.
- [37] Dong W. and Kuhnert K.-D. (2005). Robust Adaptive Control of Nonholonomic Mobile Robot with Parameter and Nonparameter Uncertainties, *IEEE Transactions on Robotics*, 21(2), 261-266.
- [38] Fierro R. and Lewis F. L. (1997). Control of a Nonholonomic Mobile Robot: Backstepping Kinematics into Dynamics. *Journal of Robotic Systems*, 14(3), 149-163.
- [39] Kolmanovsky I. and McClamroch N. H. (1995). Development in Nonholonomic Control Problems, *IEEE Control Systems*, 20-36.
- [40] Kim Min-Soeng, Shin Jin-Ho, Hong Sun-Gi, and Lee Ju-Jang. (2002). Designing a Robust Adaptive Dynamic Controller for Nonholonomic Mobile Robots under Modeling Uncertainty and Disturbances, *Mechatronics*, 13(5), 507-519.

- [41] Dong, W., Huo, W., Tso, S. K. and Xu, W. L. (2000). Tracking Control of Uncertain Dynamic Nonholonomic System and its Application to Wheeled Mobile Robots, *IEEE Transactions on Robotics and Automation*, 16(6), 870-874.
- [42] Campion, G., dAndrea-Novel, B. and Bastin, G. (1991). Modeling and State Feedback Control of Nonholonomic Mechanical Systems, *Proceedings of the 30th IEEE Conf. on Decision and Control*, 1184–1189.
- [43] Brockett R.W. (1983). Asymptotic Stability and Feedback Stabilization, *Differential Geometric Control Theory*, Birkhauser, Boston, 181–191.
- [44] Canudas de Wit C., Khennouf H., Samson C. and Sordalen O. (1993). Nonlinear Control Design for Mobile Robots. *Recent Trends in Mobile Robotics*, Vol. 11, World Scientific Series in Robotics and Automated Systems, 121-156.
- [45] Godhavn J. and Egeland O. (1997). A Lyapunov Approach to Exponential Stabilization of Nonholonomic Systems in Power Form, *IEEE Transactions on Automatic Control*, 42(7), 1028-1032.
- [46] Aguiar A., Atassi A. and Pascoal A. (2000). Regulation of a Nonholonomic Dynamic Wheeled Mobile Robot with Parametric Modeling Uncertainty Using Lyapunov Function, *Proc. 39th IEEE Conference on Decision and Control*, Sidney, Australia, 2995–3000.
- [47] Canudas de Wit C. and Sordalen O. (1992). Exponential Stabilization of Mobile Robots with Nonholonomic Constraints, *IEEE Transactions on Automatic Control*, 37(11), 1791-1797.
- [48] Hespanha J., Morse A. S. (1999). Stabilization of Nonholonomic Integrators via Logic-Based Switching. *Automatica, Special Issue on Hybrid Systems*, 35(3), 385-393.
- [49] Freund E. and Mayr R. (1997). Nonlinear Path Control in Automated Vehicle Guidance, *IEEE Transactions on Robotics and Automation*, 13(1), 49-60.
- [50] Walsh G., Tilbury D., Sastry S., Murray R. and Laumond J.P. (1994). Stabilization of Trajectories for Systems with Nonholonomic Constraints, *IEEE Transactions on Automatic Control*, 39(1), 216-222.

- [51] Fierro R. and Lewis F. (1995). Control of a Nonholonomic Mobile Robot: Backstepping Kinematics into Dynamics, *Proc. 34th IEEE Conference on Decision and Control*, New Orleans, LA, USA, 3805-3810.
- [52] Micaelli A. and Samson C. (1993). Trajectory Tracking for Unicycle-Type and Two-Steering-Wheels Mobile Robots, *Technical Report No. 2097*, INRIA, France.
- [53] Samson C. and Ait-Abderrahim K. (1990). Mobile Robot Control Part 1: Feedback Control of A Nonholonomic Wheeled Cart in Cartesian Space, Technical Report No. 1288, INRIA, France.
- [54] Jiang Z. and Nijmeijer H. (1999). A Recursive Technique for Tracking Control of Nonholonomic Systems in Chained Form, *IEEE Transactions on Robotics and Automation*, 44(2), 265279.
- [55] Colbaugh R., Barany E., and Glass K. (1998). Adaptive Control of Nonholonomic Robotic Systems, *Journal of Robotic Systems*, 15(7), pp. 365-393
- [56] Tayebi A., Tadjine M., and Rachid A., (2001). Invariant Manifold Approach for the Stabilization of Nonholonomic Chained Systems: Application to a Mobile Robot, *Nonlinear Dynamics*, 24, 167-181.
- [57] Fierro R. and Lewis F. L. (1998). Control of a Nonholonomic Mobile Robot Using Neural Networks, *IEEE Transactions on Neural Networks*, 9(4), 589-600.
- [58] Indiveri G. (1999). Kinematic Time-invariant Control of a 2D Nonholonomic Vehicle, *Proceedings of the 38th Conference on Decision and Control*, Phoenix, USA, 2112-2117.
- [59] Astolfi A. (1994). On the Stabilization of Nonholonomic Systems, *Proceedings of the 33rd Conference on Decision and Control*, Lake Buena Vista, USA, 3481-3486.
- [60] Aicardi M., Casalino G., Bicchi A. and Balestrino A. (1995). Closed Loop Steering of Unicycle Like Vehicles Via Lyapunov Techniques, *IEEE Robotics and Automation Magazine*, 2, pp. 27-35.
- [61] A. Tayebi A. and Rachid A. (1997). A Unified Discontinuous State Feedback Controller for the Path-following and the Point-stabilization Problems of a

- Unicycle-like Mobile Robot, *Proceedings of the 1997 IEEE International Conference on Control Applications*, Hartford, USA, 31-35.
- [62] Altafini C. (2003). Path Following With Reduced Off-Tracking for Multibody Wheeled Vehicles, *IEEE Transaction on Control Systems Technology*, 11(4), 598-605.
- [63] Samson C. (1995). Control of Chained Systems: Application to Path Following and Time-varying Point-stabilization of Mobile Robots, *IEEE Transaction on Automatic Control*, 40(1), 64-77.
- [64] Sampei M., Tamura T., Itoh T. and Nakamichi M. (1991). Path Tracking Control of Trailer-like Mobile Robot, *IEEE/RSJ International Workshop on Intelligent Robots and Systems, IROS91*, Osaka, 193-198.
- [65] Guldner, J. and Utkin, V. I. (1995). Sliding Mode Control for Gradient Tracking and Robot Navigation Using Artificial Potential Fields, *IEEE Transactions on Robotics and Automation*, 11(2), 247-254.
- [66] dAndrea Novel, B., Campion, G. and Bastin, G. (1995). Control of Nonholonomic Wheeled Mobile Robots by State Feedback Linearization. *Int. J. Robot. Res.*, 14(6), 543-559.
- [67] Kozłowski, K. and Majchrzak, J. (2002). A Backstepping Approach to Control a Nonholonomic Mobile Robot. *In Proc. IEEE Conf. Robot. Autom.*, 39723977.
- [68] Yang, S.X., Yang, H. and Meng, M. Q.-H. (2004). Neural Dynamics Based Full-state Tracking Control of a Mobile Robot. *In Proc. IEEE Conf. on Robotics and Automation*, 5, 46144619.
- [69] De Luca, A., Oriolo, G. and Samson C. (1998). Feedback Control of a Nonholonomic Car-like Robot, *Robot Motion Planning and Control*, Springer-Verlag, 170-253.
- [70] Pacejka, H. B. (2002). Tire and Vehicle Dynamics, *Society of Automotive Engineers and Butterworth-Heinemann*, Oxford.
- [71] Malan, S., Milanese, M., Borodani, P. and Gallione, A. (2005). Lateral Control of Autonomous Vehicle for Public Urban Mobility Systems, *Proceedings of IEEE Conference on Intelligent Transportation Systems*, 372-377.

- [72] Tondel, P. and Johansen, T. A. (2003). Lateral Vehicle Stabilization Using Constrained Nonlinear Control, *Lateral vehicle stabilization using constrained nonlinear control*, Cambridge.
- [73] Meier, G., Roppenecker, G. and Wurmthaler, C. (2004). Automatic Lateral Vehicle Guidance Using Tracking Control - A Modular Approach to Separate Driver- and Vehicle-Dependent Dynamics, *Proceedings of the IEEE Intelligent Vehicles Symposium*, 145-149.
- [74] Choi, S.B. (2000). The design of the Look-Down Feedback Adaptive Controller for the Lateral Control of Front-Wheel-Steering Autonomous Highway Vehicles, *IEEE Transactions on Vehicular Technology*, 49(6), 2257-2269.
- [75] Tan, H.S., Guldner J., Patwardhan, S., Chen, C. and Bougler B. (1999). Development of an Automated Steering Vehicle Based on Roadway Magnets - A Case Study of Mechatronic System Design, *IEEE/ASME Transactions on Mechatronics*, 4(3), 258-272.
- [76] Hernandez, J.I. and Kuo, C.Y. (2003). Steering Control of Automated Vehicles Using Absolute Positioning GPS and Magnetic Markers, *IEEE Transactions on Vehicular Technology*, 52(1), 150-161.
- [77] Chen, C. and Tan H.S. (1999). Experimental Study of Dynamic Look-Ahead Scheme for Vehicle Steering Control, *Proceeding of the American Control Conference*, San Diego, 3163-3167.
- [78] Rossetter, E.J. and Gerdes J.C. (2002). A study of Lateral Vehicle Control Under a 'Virtual' Force Framework. *International Symposium on Advanced Vehicle Control*, Japan.
- [79] Mammar, S. and Netto, M. (2004). Integrated Longitudinal and Lateral Control for Vehicle Low Speed Automation, *Proceeding of the IEEE International Conference on Control Applications*, 350-355.
- [80] Chaibet, A., Nouveliere, L., Mammar, S., Netto, M. and Labayrade, R. (2005). Backstepping Control Synthesis for Both Longitudinal and Lateral Automated Vehicle, *IEEE Intelligent Vehicles Symposium*, 42-47.
- [81] Hung, J. Y., Gao, W. and Hung, J. C. (1993). Variable Structure Control: A Survey. *IEEE Transaction on Industrial Electronics*, 40(1), 2-22.

- [82] Utkin, V. I. (1977). Variable Structure Systems with Sliding Mode. *IEEE Transactions on Automatic Control*, 22(2), 212-222.
- [83] Utkin, V. I. and Young, K. D. (1978). Method for Constructing Discontinuity Planes in Multidimensional Variable Structure Systems. *Automation and Remote Control*, 39(10), 1466-1470.
- [84] Slotine, J. J. and Sastry, S. S. (1982). Tracking Control of Non-linear Systems Using Sliding Surfaces, with Application to Robot Manipulators. *Massachusetts Institute of Technology*, Cambridge MA 02139, Technical Report LIDS-P-1264, 1-54.
- [85] Slotine, J. J. and Li, W. (1991). Applied Nonlinear Control. *Prentice-Hall*, Inc, Inglewood Cliffs, New Jersey
- [86] Utkin, V. I. (1992). Sliding Modes in Control Optimization. New York, *Springer-Verlag*.
- [87] Young, D. K. and Ozguner, U.(1993). Frequency Shaping Compensator Design for Sliding Mode. *Int. J. Control*, 57(5), 1005-1019
- [88] DeClarlo, R.A., Zak, S. H. and Mathews, G. R. (1988). Variable Structure Control of Nonlinear Multivariable Systems: A Tutorial. *Proceedings of the IEEE*, 76(3), 212-232.
- [89] Gao, W. and Hung, J. C. (1993). Variable Structure Control of Nonlinear Systems: a New Approach. *IEEE Transaction on Industrial Electronics*, 40(1), 45-55.
- [90] Loh, A.M. and Yeung L.F. (2004). Chattering Reduction in Sliding Mode Control: An Improvement for Nonlinear Systems, *WSEAS Transaction on Systems*, 9(3), 2878-2885.
- [91] Young, D. K., Utkin,V. I. and Ozguner, U.(1999), A Control Engineer's Guide to Sliding Mode Control. *IEEE Transaction on Control System Technology*, 7(3), 328-342.
- [92] Haskara, I. and Ozguner, U. (1999). An Estimation Based Robust Tracking Controller Design for Uncertain Nonlinear System. *Proceedings of the 38th Conference on Decision and Control*, Arizona USA, 4816-4821.

- [93] Elmali, H. and Olgac, N. (1996). Implementation of Sliding Mode Control with Perturbation Estimation (SMCPE). *IEEE Transaction on Control System Technology*, 4(1), 79-85.
- [94] Moura, J. T., Roy, R. G. and Olgac, N. (1997). Sliding Mode Control with Perturbation Estimation (SMCPE) and Frequency Shaped Sliding Surfaces. *Journal of Dynamic Systems, Measurement, and Control*, 119(3), 584-588.
- [95] Bartolini, G. and Pydynowski, P. (1996). An Improved, Chattering Free, VSC: Scheme for Uncertain Dynamical Systems. *IEEE Transaction on Automatic Control*, 41(8), 1220-1226.
- [96] Bartolini, G., Ferrara, A. and Usai, E. (1998). Chattering Avoidance by Second-order Sliding Mode Control. *IEEE Transactions on Automatic Control*, 43(2), 241-246.
- [97] Pan, Y. and Furuta, K. (2006). Variable Structure Control with Sliding Sector for Hybrid Systems. *Proceedings of the 2006 International Workshop on Variable Structure Systems*, Alghero, Italy, 286-291.
- [98] Jiang, K., Seneviratne, L.D. and Earles, S.W.E (1997). Time-optimal Smooth-path Motion Planning for a Mobile Robot with Kinematic Constraints. *Robotica*, 15, 547-553.
- [99] Aydin, S. and Temeltas, H. (2004). Fuzzy-Differential Evolution Algorithm for Planning Time-Optimal Trajectories of a Unicycle Mobile Robot on a Predefined Path. *Advanced Robotics*, 18(7), 725-748.
- [100] Stentz, A. (1993). Optimal and Efficient Path Planning for Unknown and Dynamic Environments. *Carnegie Mellon University Robotics Institute*, Technical Report CMU-RI-TR-93-20, 1-38.
- [101] Louste, C. and Liegeois, A. (2002). Path Planning for Non-holonomic Vehicles: a Potential Viscous Fluid Field Method. *Robotica*, 20, 291-298.
- [102] Parkin, R.E. (1991). Applied Robotic Analysis. *Prentice Hall*, New Jersey.
- [103] Gallina, P. and Gasparetto, A. (2000). A Technique to Analytically Formulate and to Solve the 2-Dimensional Constrained Trajectory Planning Problem for a Mobile Robot. *Journal of Intelligent and Robotic Systems*, 27, 237-262.

- [104] Munoz, V., Ollero, A., Prado, M. and Simon, A. (1994). Mobile Robot Trajectory Planning with Dynamic and Kinematic Constraints. *Proceedings 1994 IEEE International Conference on Robotics and Automation*, 4, 2802-2807.
- [105] Lamiriaux, F., Sekhavat, S., Laumond, J.P. (1999). Motion Planning and Control for Hilare Pulling a Trailer. *IEEE Transactions on Robotics and Automation*, 15(4), 640-652.
- [106] Cherif, M. (1999). Motion Planning for All-Terrain Vehicles: A Physical Modeling Approach for Coping with Dynamic and Contact Interaction Constraints. *IEEE Transactions on Robotics and Automation*, 15(2), 202-218.
- [107] Fotouhi, R., Szyszkowski, W. and Nikiforuk, P. (2002). Trajectory Planning and Speed Control for a Two-link Rigid Manipulator. *Journal of Mechanical Design*, 124(3), 585-589.
- [108] Munoz, V., Cruz, A. and Garcia-Cerezo, A. (1998). Speed Planning and Generation Approach Based on the Path-time Space for Mobile Robots. *Proceedings in the IEEE International Conference on Robotics and Automation*, 3, 2199-2204.
- [109] Prado, M., Simon, A. and Ezquerro, F. (2002). Velocity, Acceleration and Deceleration Bounds for a Time-Optimal Planner of a Wheeled Mobile Robot. *Robotica*, 20, 181-193.
- [110] Prado, M., Simon, A., Carabias, E., Perez, A. and Ezquerro, F. (2003). Optimal Velocity Planning of Wheeled Mobile Robots on Specific Paths in Static and Dynamic Environments. *Journal of Robotic Systems*, 20(12), 737-754.
- [111] Piazzzi, A. and Guarino Lo Bianco, C. (2000). Quintic G^2 -Spline for Trajectory Planning of Autonomous Vehicles. *Proceedings in the IEEE Intelligent Vehicles Symposium*, Dearborn, USA, 198-203.
- [112] Guarino Lo Bianco, C. and Piazzzi, A. (2000). Optimal Trajectory Planning with Quintic G^2 -Spline. *Proceedings in the IEEE Intelligent Vehicles Symposium*, Dearborn, USA, 620-625.
- [113] Maeda, S., Futatsuka, M., Yonesaki, J. and Ikeda, M. (2003). Relationship Between Questionnaire Survey Results of Vibration Complaints of Wheelchair Users and Vibration Transmissibility of Manual Wheelchair. *In Health and Preventive Medicine*, 8, 82-89.

- [114] Forstberg, J. (2000). Ride Comfort and Motion Sickness in Tilting Trains - Human Responses to Motion Environments in Train and Simulator Experiments. *Doctoral Thesis*, Stockholm.
- [115] European-Parliament and the Council of the European Union. (2002). On the Minimum Health and Safety Requirements Regarding the Exposure of Workers to the Risks Arising from Physical Agents. *Official Journal of the European Communities*, Directive 2002/44/EC.
- [116] Atapourfard M., Ishihara T. and Inooka. H. (2002). The Influences of Trunk Horizontal Vibration to the Head-neck Complex. *SICE02*, Osaka, 1053–1058.
- [117] Atapourfard M., Ishihara T. and Inooka H. (2004). Identification of the Head-neck Complex in Response to Trunk Horizontal Vibration. *Biological Cybernetics*, 90(6), 418–426.
- [118] Gurses S., Dhaher Y., Hain T.C. and Keshner E.A. (2005). Perturbation Parameters Associated with Nonlinear Responses of the Head at Small Amplitudes. *CHAOS*, 15(2), 023905.1–023905.10.
- [119] Kitazaki S. and Griffin M.J. (1997). A Modal Analysis of Whole-body Vertical Vibration Using a Finite Element Model of the Human Body. *Journal of Sound and Vibration*, 200(1), 83–103.
- [120] Van Der Woude, L.H.V., Hopman M.T.E and Kemenade, C.H. (1999) Biomedical Aspects of Manual Wheelchair Propulsion: The State of the Art II. *Assistive Technology Research Series*, 5, 392 pp.
- [121] Pires, G. and Nunes, U. (2002). A Wheelchair Steered Through Voice Commands and Assisted by a Reactive Fuzzy-logic Controller, *Int. Journal of Intelligent and Robotic Systems*, 34(3), 301-314.
- [122] Maia, R., Cortesao, R., Nunes, U., Silva, V. and Fonseca, J. (2003). Robust Low-Level Motion Control of WMR with Stochastic Active Observers, *The 11th International Conference on Advanced Robotics, Coimbra*, 2, 876-882.
- [123] Yanco, H.A. (1998). Wheellesley, a Robotic Wheelchair System: Indoor Navigation and User Interface. In *Lecture Notes in Artificial Intelligence: Assistive Technology and Artificial Intelligence*. Springer-Verlag, 256268.

- [124] Levine, S.P., Bell, D.A., Jaros, L.A., Simpson, R.C., Koren, Y., and Borenstein, J. (1999). The NavChair Assistive Wheelchair Navigation System, *IEEE Transactions on Rehabilitation Engineering*, 7(4), 443-451.
- [125] Gomi, T. and Ide, K. (1996). The Development of an Intelligent Wheelchair, *IVS'96*, Tokyo, 70-75.
- [126] Mazo, M., Garcia, J.C., Rodriguez, F.J., Urena, J., Lazaro, J.l, Espinosa, F. (2002). Experiences in Assisted Mobility: the SIAMO Project, *The 2002 IEEE International Conferences on Control Applications*, 2, 766-771.
- [127] Rofer, T. and Lankenau, A. (1999). Ensuring Safe Obstacle Avoidance in a Shared-Control System. *7th IEEE International Conference on Emerging Technologies and Factory Automation*, 2, 1405-1414.
- [128] Lankenau, A., Meyer, O. and Krieg-Bruckner, B. (1998). Safety in Robotics: the Bremen Autonomous Wheelchair, *The 5th Int. Workshop on Advanced Motion Control, AMC '98-Coimbra.*, 524-529.
- [129] Prassler, E., Scholz, J., Strobel, M. (1998). Maid: Mobility Assistance for Elderly and Disabled People, *The 24th Annual Conference of the IEEE on Industrial Electronics Society*, 4, 2493-2498.
- [130] Atapourfard, M., Ishihara, T. and Inooka, H. (2002). The Influences of Trunk Horizontal Vibration to the Head-Neck Complex, *SICE02*, Osaka, 2, 1053-1058.
- [131] Nakashima, Y. and Maeda, S. (2004). Effects of Seat-Back Angle and Accelerometer Height at the Seat-Back on Seat-Back X Axis r.m.s. Acceleration in Field Experiments according to the ISO2631-1 Standard, *Industrial Health*, 42(1), 65-74.
- [132] Urbano, J., Terashima, K., Miyoshi, T. and Kitagawa, H. (2005). Velocity Control of an Omni-directional Wheelchair Considering User's Comfort by Suppressing Vibration, *IEEE/RSS Intelligent Robots and Systems (IROS 05)*, 3169-3174.
- [133] ISO. (1997). Mechanical vibration and shock - Evaluation of Human Exposure to Whole Body Vibration - Part 1: General Requirements, *ISO 2631-1*.

- [134] Fleury, S., Herrb, M. and Chatila, R. (1997). GenoM: A Tool for the Specification and the Implementation of Operating Modules in a Distributed Robot Architecture, *Proceedings of the International Conference on Intelligent Robots and Systems*, Grenoble, France, 842-848.
- [135] Fleury, S. Herrb, H. and Mallet, A. (2001). GenoM User's Manual. Technical report 01577, *LAAS-CNRS*. <https://softs.laas.fr/openrobots/wiki>.
- [136] Lopes A. C., Moita F., Nunes U., and Solea R., An Outdoor Guidepath Navigation System for AMRs Based on Robust Detection of Magnetic Markers, *12th IEEE International Conference on Emerging Technologies and Factory Automation*, Patras, 989–996, 2007.
- [137] Solea R. and Nunes U. (2008), Robotic Wheelchair Control Considering User Comfort. Modeling and Experimental Evaluation, *ICINCO 2008 - International Conference on Informatics in Control, Automation and Robotics*, Funchal, Madeira - Portugal, 37–44.
- [138] Khalil H. K. (2002). *Nonlinear Systems*, 3rd. ed. Upper Saddle River, Prentice Hall.